UNIVERSITY OF CALIFORNIA SAN DIEGO

Bernstein and Finite-Length Diocotron Modes in a Non-Neutral Plasma Column

A dissertation submitted in partial satisfaction of the
requirements for the degree
Doctor of Philosophy

in

Physics

by

Daniel Walsh

Committee in charge:

Professor Daniel H. E. Dubin, Chair
Professor C. Fred Driscoll
Professor Sergei Krasheninnikov
Professor John McGreevy
Professor Thomas O'Neil
Professor Kraig Winters

2018

The dissertation of Daniel Walsh is approved, and it is acceptable in quality and form for publication on microfilm and electronically:

_____

_____

_____

_____

_____

_____

Chair

University of California San Diego

2018

DEDICATION

This dissertation is not dedicated to a person, but to a frame of mind: physics is conducted in the pursuit of understanding nature, wherein one discovers that unearthing truth is more than sufficient to warrant this mission. To dedicate this scientific work to anything else would detract from this goal, and be a misrepresentation of the countless hours and deep thought required to reach this point. My dedication cannot be expressed by a mere block of text in a dissertation, but rather is embodied by my devotion to the discipline through continual curiosity in the mechanics of the Universe.

EPIGRAPH

Everything should be as simple as it can be, but not simpler.

—Albert Einstein

The first principle is that you must not fool yourself and you are the easiest person to fool.

—Richard P. Feynman

TABLE OF CONTENTS

LIST OF FIGURES

LIST OF TABLES

ACKNOWLEDGEMENTS

I would like to thank my colleagues in the Nonneutral Plasma group for their support, input, and insights that have contributed to my successes. First, I thank my advisor, Daniel Dubin, for his guidance along the way. His passive demeanor allowed me to be my own harshest critic, and forced me to take responsibility for my own research decisions, as any researcher must learn to do. I would also like to thank Tom O'Neil for his willingness to engage in discussions with me, and for always offering keen, fundamental insight. He also provided a constant reminder to me that even a book filled with all physics formulae is useless without the guidance of strong physical intuition.

On the experimental side, Fred Driscoll served as an anchor that kept me grounded. Frequently, I would find myself painstakingly analyzing a mathematical detail of my research, and Fred was very helpful in keeping me focused on the "big picture" aspects of the problem, which helped me immensely, for which I am very grateful. Next, I wish to thank researchers Francois Anderegg and Andrey Kabantsev, as well as my fellow research students Matt Affolter and Kurt Thomson, for their willingness and patience in providing the experimental results I needed to compare my work to experiment, as well as for enlightening conversations and insights exchanged.

Finally, I would like to especially acknowledge my mother and father, as well as the rest of my family, without whom none of this would have been possible. My mother and father, in particular, supplied me with unwavering support and love, which I will never be able to repay.

Thank you, and all others with whom I have crossed paths, for playing a role–however small–in shaping me into the person I am today.

Chapter 2, in full, is a reprint of the material as it appears in Physics of Plasmas: Daniel Walsh and Daniel H. E. Dubin, "Bernstein modes in a non-neutral plasma column", *Physics of Plasmas*, **25**, 052119 (2018). Daniel Walsh was the primary investigator and author of this paper.

VITA

2011	B.A., University of California Santa Barbara
2016	M.S., University of California San Diego
2011-2015	Graduate Teaching Assistant, University of California San Diego
2018	Ph. D. in Physics, University of California San Diego

PUBLICATIONS

Daniel Walsh and Daniel H. E. Dubin, "Bernstein modes in a non-neutral plasma column", *Physics of Plasmas*, **25**, 052119 (2018).

Daniel Walsh, Daniel Dubin. 2017. Finite-Length Diocotron Modes in a Non-neutral Plasma Column. Poster session presented at: Milwaukee, Wisconsin.

D. Walsh, D.H.E. Dubin. 2017. Numerical and Analytical Calculation of Bernstein Modes in a Plasma Column. Poster session presented at: Lawrence University; Appleton, Wisconsin.

D.K. Walsh, D.H. E. Dubin. 2016. Numerical and Analytical Calculation of Bernstein Resonances in a Non-Uniform Cylindrical Plasma. Poster session presented at: APS Division of Plasma Physics; San Jos, California.

Daniel K. Walsh, Daniel H. E. Dubin. 2015. Numerical and Analytical Calculation of Bernstein Mode Resonances in a Non-Uniform Cylindrical Plasma. Poster session presented at: APS Division of Plasma Physics; Savannah, Georgia.

D. Walsh, D.H.E. Dubin. 2014. Numerical solution for linear cyclotron and diocotron modes in a nonneutral plasma column. Poster session presented at: APS Division of Plasma Physics; New Orleans, Louisiana.

ABSTRACT OF THE DISSERTATION

Bernstein and Finite-Length Diocotron Modes in a Non-Neutral Plasma Column

by

Daniel Walsh

Doctor of Philosophy in Physics

University of California San Diego, 2018

Professor Daniel H. E. Dubin, Chair

This Dissertation consists of solutions to two major problems. Chapter 2 presents theory and numerical calculations of electrostatic Bernstein modes in an inhomogeneous cylindrical plasma column. These modes rely on finite Larmor radius (FLR) effects to propagate radially across the column until they are reflected when their frequency matches the upper hybrid frequency. This reflection sets up an internal normal mode on the column, and also mode-couples to the electrostatic surface cyclotron wave (which allows the normal mode to be excited and observed using external electrodes). Numerical results predicting the mode spectra, using a novel linear Vlasov code on a cylindrical grid, are presented and compared to an analytic WKB theory. A previous version of the theory[6] expanded the plasma response in powers of 1/B, approximating

the local upper hybrid frequency, and consequently its frequency predictions are spuriously shifted with respect to the numerical results presented here. A new version of the WKB theory avoids this approximation using the exact cold fluid plasma response and does a better job of reproducing the numerical frequency spectrum. The effect of multiple ion species on the mode spectrum is also considered, to make contact with experiments that observe cyclotron modes in a multi-species pure ion plasma.[1]

Chapter 3 presents theory and numerical calculation for the finite-length diocotron mode frequency with arbitrary azimuthal mode number. The numerical calculation solves a bounce-averaged version of the Vlasov equation to determine the perturbed potential in the presence of the mode, along with its frequency. The analytic theory is also obtained from the bounce averaged Vlasov equation, but we derive a theorem that allows us to obtain an effective fluid theory consistent with the full Vlasov theory, which integrates out the surface phase space associated with the bouncing motion, considerably simplifying the analysis. We use this effective fluid theory to derive frequency shifts for finite-length cylindrical plasmas, and find good agreement with experiment and with our numerical bounce-averaged Vlasov theory.

Chapter 1

Introduction

1.1 Brief History and General Overview

This dissertation develops theory for two important wave phenomena in the physics of strongly magnetized plasmas, both of which study how the plasma temperature affects magnetized plasma modes traveling perpendicular to the magnetic field. The two topics study two distinct regimes, first for high frequency modes near the cyclotron frequency; and second, for lower frequency modes driven by $\vec{E} \times \vec{B}$ drift dynamics.

The origin of the first topic of the dissertation was due to Ira B. Bernstein, who first considered the propagation of thermal plasma waves perpendicular to the applied magnetic field in 1958. These waves, called Bernstein modes, are collective excitations of the plasma near the cyclotron frequency $\Omega = \frac{qB}{mc}$ (or integer multiples thereof). In this work, we will focus on the fundamental modes, ignoring modes near multiples of the cyclotron frequency, although the work presented here could also be naturally extended to include the higher harmonics, if desired. Excluding mutual electrostatic particle interactions (and image charges), but including thermal effects, the motion is quite trivial, as particles will simply undergo circular motion in a uniform magnetic field, with constant frequency Ω. This theory has no wave propagation due

to the independence of the dispersion relation on the wave vector k. The theoretical inverse of this situation is when we *include* mutual electrostatic effects, but *exclude* thermal effects. Such a theory, called a "fluid theory" allows particles to communicate via the electrostatic potential Φ, but assumes each spatial point can only possess a single "fluid velocity" to which all particles at that point are attributed. The resulting motion in this case exhibits so-called "upper-hybrid modes", which are still analytically tractable modes, and again do not propagate! A natural question arises, then: "What does the theory that includes both electrostatic interactions *and* thermal effects predict?" Surprisingly, the combination of the restoring forces from the sum of the magnetic Lorentz force and the mutual electric forces of these effects together creates a non-trivial dispersion relation, and gives rise to traveling waves.

This can be understood physically when one realizes that as the temperature increases, the cyclotron radius r_c also increases, meaning that a single particle physically behaves more like its charge is smeared around its finite, roughly-circular orbit. This means that the "effective electric field" felt by a particle is not sampled at the instantaneous position of that particle, but rather sampled over nearby spatial points over a distance roughly r_c. For a wavelike solution, the effective perturbed field, and consequently the effective restoring force, will tend to be somewhat smaller than the field sampled at a point, since the concavity of the field, (and therefore the "effective field" perturbation) always opposes the value of the field at that point, reducing its averaged magnitude. For $kr_c \ll 1$, the correction is minor, whereas for $kr_c \gg 1$, the averaging takes place over many wavelengths, and the effective field is almost entirely annihilated. Consequently, the effective electric restoring force is a function of the wavenumber k, the dispersion relation becomes non-trivial, and wave-propagation emerges. As such, Bernstein modes should be considered related to, yet distinct from cyclotron and upper-hybrid modes in that they appear as a consequence of finite Larmor radius effects, splitting a single cyclotron mode frequency into a number of finer frequency peaks clustered near the bare cyclotron frequency, as determined by the discrete spectrum of the resulting wave equation upon imposing boundary conditions.

This temperature dependence is also of great experimental interest, since it offers a non-destructive and reliable plasma temperature measurement. Aside from temperature diagnostics, however, this theory of Bernstein modes also shows promise in other types of diagnostics, such as plasma density profile and isotope purity.

The second type of plasma mode, called the diocotron mode, was first measured in pure electron plasmas by DeGrassie and Malmberg in 1980. "Diocotron" derives from a Greek word meaning "pursue", as the first experimental studies of these plasmas showed instabilities in which the plasma would break up into smaller pieces that seemed to be in pursuit of each other, drifting around the axis of the plasma trap. The reason for this azimuthal drift is a subtle consequence of the interplay between the cyclotron motion discussed in the previous paragraph with an electric field. While a charged particle at rest remains motionless in a magnetic field, the addition of a perpendicular electric field will push on the stationary particle, starting it in motion. Since the magnetic field does no work, the charge moves with a higher speed at lower electric potential energy than higher potential energy, causing the particle's mean velocity to deviate from that of the case of simple cyclotron motion. The resulting motion resembles circular cyclotron motion, except that the particle's orbit will drift gradually in a direction perpendicular to both the electric and magnetic fields. This behavior is called $\vec{E} \times \vec{B}$ drift dynamics. In strong magnetic fields, the cyclotron radius can become quite small to the point that often it becomes superfluous to follow the minute details of the cyclotron motion, justifying a "course graining" analysis where only the guiding center, and not the tiny cyclotron orbits around that center can be resolved.

In this guiding center drift theory, the perpendicular velocity is immediately dictated by the local electric and magnetic fields as $v_\perp = c\frac{\vec{E}\times\vec{B}}{B^2}$. The velocity is determined at each point in space and time, so the notion of a temperature associated with a 2D $\vec{E} \times \vec{B}$ drift plasma ceases to be relevant. Instead, we turn to the more complex problem of studying 3D diocotron modes, where axial bounce motion and finite-length effects are retained, and for which a temperature (called $T_\parallel$) is defined (the subscript notation will usually be dropped since $T_\perp$ is not relevant in this

chapter). In this body of work, we focus on the 3D diocotron mode frequencies, and the central goal, analogous to chapter 2, is to theoretically understand the dependence of diocotron mode frequencies on $T_{\|}$. Because only the slow drift motion is kept, diocotron frequencies are always smaller than the cyclotron frequency (often by orders of magnitude or greater). Understanding temperature dependence on mode frequency is critical to many areas of plasma physics (even to those not directly studying diocotron modes) because this dependence can be used to measure the plasma temperature in a non-destructive way (i.e. without modifying or destroying the plasma in the process).

To give a sense of how a "diocotron thermometer" could work, consider a single plasma particle, which rapidly travels axially at constant r, like a bead on a wire. Since the plasma is axially contained electrostatically, there comes a point at the end of the plasma where the particle is reflected by the external confinement fields, and is forced to turn around and return to the other side, after which it bounces again. Inside the plasma, the radial electric field E_r (which is responsible for driving the azimuthal drift motion) is practically uniform, so the particle gradually orbits the center of the trap at a constant rate. However, while the particle is in the end region, E_r, and consequently the drift velocity, deviate significantly from their previous values, causing the particle to move azimuthally in a non-uniform manner. This brings about a correction to the diocotron mode frequency due to this unexpected kick (as compared to the infinite-length theory). Furthermore, it is clear that the size of this correction will depend on how much time a particle spends in these ends, and how deeply the particle penetrates into the end. The conclusion is that a hotter plasma, which has more higher-velocity particles, will experience a greater correction than a cold plasma. It is this observation that provides the motivation to theoretically study thermal effects on finite-length diocotron modes, which would provide a new way for experimentalists to non-destructively measure temperature.

The theoretical analysis turns out to be more subtle than it appears at first glance due to two competing thermal effects (which we call μ, for "magnetron"; and λ, for "length") that can

partially cancel each other out. As we will see, the diocotron mode frequency tends to increase as temperature is increased, when holding the central density and radial profile fixed, due to this additional "kick" particles experience at the end. However, the plasma also expands axially as temperature increases, which effectively lowers the central plasma density, and consequently the mode frequency. It is then not at all clear which of these effects will win; as we will see, both frequency increase and decrease with temperature are possible. These two opposite dependencies are readily seen when comparing an $\ell = 1$ with an $\ell = 2$ diocotron mode. A positive temperature dependence is predicted and observed for $\ell = 1$, while a negative dependence is predicted and observed for $\ell = 2$.

To gain some understanding of the reversal of temperature dependence between $\ell = 1$ and $\ell = 2$, it is useful to recognize that the λ effect comes from a change to the central density, which has a multiplicative effect on the mode frequency (central density and mode frequency are proportional), while the μ effect comes from an absolute kick on the ends, which has an additive effect on the mode frequency. As a result, the contribution from μ is roughly the same for either mode, while the effect from λ can be significantly larger for $\ell = 2$ than for $\ell = 1$, since the mode frequencies can be markedly different between these two modes for narrow plasmas compared to the wall radius. After all, the $\ell = 1$ diocotron mode frequency for a plasma with no conducting wall is zero (the wall is required to drive this mode), while all higher ℓ modes have non-zero frequencies.

Finally, in this diocotron section, we also develop a formalism to study non-uniform temperature effects (where temperature is a function of radius), to gain a theoretical understanding to make contact with recent experiments. It is shown that for a well-contained plasma, there is only very small radial dependence, and the relevant quantity to predict frequency shift is the total thermal energy introduced to the plasma, regardless of radial distribution.

In the next sections, we will give a more detailed overview of these two subjects, briefly reviewing the major results of the two following chapters.

1.2 High-Frequency Magnetized Modes

In chapter 2, the first topic is covered, in which the theory of "fast" Bernstein modes is developed and extended from the existing literature, examining both analytical and computational solutions to non-uniform plasma columns, with either a single species, or multiple species, which allow comparison to experiments that are neither uniform, nor comprised of a single species. In the discussion of this first topic, the plasma is always assumed to be axially symmetric (and infinite in length), but not azimuthally symmetric, such that the system is modeled as a two-dimensional plasma. Since Bernstein modes are thermal effects, arising from the finite Larmor Radius of particles in the magnetized plasma, the cold fluid theory is only valid in the $T = 0$ limit, where a single cyclotron resonance is observed in the plasma response to a driver, and no additional structure is seen. As the temperature is increased, a family of new modes, called *Bernstein modes* are predicted to emerge from the single cyclotron resonance. At low temperatures, these modes are very closely spaced in frequency, and are not resolvable due to some physical damping mechanism such as particle collisions. However, when the temperature is increased, the mode spacing increases, and a number of Bernstein modes appear, no longer hidden by the finite collisionality. The origin of these modes is that the non-zero Larmor radius of the plasma particles allows them to explore a finite neighborhood around their guiding center positions as they undergo their small circular orbits. As a result, at any time, the force felt by these particles differs from the force that would be predicted from cold fluid theory, where every point in space has a single unambiguous fluid velocity rather than some non-trivial distribution of particle velocities.

This Bernstein chapter presents many new results on these Bernstein modes. First, the fluid theory of these cyclotron modes are studied, and the resulting differential equation is studied by examining its singular points, which correspond to locations in the plasma where the mode potential diverges. While these modes are unphysical, their physical nature becomes

clear when considered as a continuum basis of modes; some continuous combination of which forms a continuous, physical quasimode. This fluid theory, however, is insufficient to explain Bernstein modes, which only appear when thermal effects are introduced. Two distinct theoretical approaches are employed to understand these modes: first, a powerful numerical Vlasov approach is derived, which studies the details of the plasma evolution in phase-space, allowing details of the thermal distribution to be retained, and thereby giving rise to Bernstein modes. Anti-Hermiticity of the resulting operator describing the mode is established, which aids in numerical solution to the problem. Second, an advanced WKB theory is developed, allowing a much simpler description of Bernstein modes, which generalizes the Bernstein dispersion relation to be applicable to a plasma with gradually changing density as a function of space. After developing a theorem on the form of the perturbed potential with $e^{-i\omega t+i\ell\theta}$ in a uniform plasma, and partitioning the solution region into partially overlapping subsets, the Bernstein mode frequencies are calculated, and compared to the results of the numerics. Good agreement is seen between the Vlasov and WKB approaches for both $\ell = 2$ and $\ell = 4$, although the behavior near wave-particle resonances is still not fully understood. Next, the problem is generalized to account for impure plasmas, consisting of other ion isotopes, or even different ions altogether. With this generalization, necessary conditions are established for Bernstein modes, and presented in the form of plots. Finally, the somewhat special $\ell = 0$ (azimuthally symmetric) mode is studied and compared to existing numerical work done in this regime, again demonstrating good agreement.

1.3 Low-Frequency Magnetized Modes

In chapter 3, a completely different problem of "slow" diocotron modes in the same geometry as chapter 2, is studied. In this section, we also consider 3D effects due to the finite axial extent of the plasma, which were neglected in chapter 2. The axial extent is determined by two end confinement rings whose potential keeps the plasma contained axially. Again, the effect

of plasma temperature on mode frequency is studied on this finite-length column. Much like Bernstein modes, the diocotron mode is critical for experimental manipulation of plasmas, and is used for a variety of nondestructive experimental diagnostics. Similar to the situation in chapter 2, while a cold diocotron mode is well-described with cold fluid theory, a temperature increase produces a frequency shift to the mode. We will see that there are two physical reasons for this. First, the plasma density changes as temperature increases and the particles travel farther axially before returning. Since even the infinite-length diocotron frequency depends on the density, this effect tends to make the mode frequency decrease as temperature increases. Second, these warm particles also feel a stronger radial force from the confinement cylinders which acts to increase the mode frequency. Third, the fact that the plasma itself has a finite length means that the self-consistent plasma fields differ from that of an infinite column, either from the image field (as in $\ell = 1$), and in the non-image field (as in $\ell > 1$). The net frequency shift is a combination of these effects. These findings motivate a new temperature diagnostic using diocotron mode frequency dependence on finite plasma length and thermal corrections, made possible by the theoretical results of chapter 3.

Chapter 2

Bernstein Modes

2.1 Introduction

This chapter presents a linearized theory of electrostatic cyclotron waves in both single and multiple-species nonneutral plasma columns. For simplicity we consider the component of plasma response independent of axial position z, but we include thermal effects on the waves, focussing mainly on Bernstein modes. There have been several experimental[1, 17, 9] and theoretical[6, 8, 10] papers studying electrostatic cyclotron waves in a nonneutral plasma in the cold-fluid regime (neglecting thermal effects). In seminal work that included thermal effects, Gould et. al.[9] treated a parabolic-profile plasma using an approximate wave equation to estimate Bernstein mode frequencies, and also performed experiments that observed the modes on a pure electron plasma column. A partial WKB theory analysis was provided, but it neglected mode-coupling between the Bernstein and surface cyclotron modes. While Bernstein modes were observed in these experiments, the plasma was not well characterized, as parameters of the plasma (radius, temperature, etc.) were time-dependent as the plasma decayed toward the wall.

In 1995, E. Sarid et. al. [17] measured cyclotron modes in a Magnesium ion plasma with multiple species. Multiple modes were observed near the ion cyclotron frequency, some of

which may have been Bernstein modes, but the plasma was not sufficiently well-characterized to determine this. Recently, Hart and Spencer performed particle-in-cell simulations on an infinite-length plasma in global thermal equilibrium.[10], and observed azimuthally-symmetric Bernstein modes. Meanwhile, Dubin carried out a full WKB warm fluid theory describing Bernstein modes, extending the work of Gould by accounting for accurate equilibrium distributions, and retaining the crucial linear mode coupling between the internal Bernstein and surface cyclotron modes.[6] However, a large magnetic field limit was assumed by Dubin, and it is a priori unclear how large the magnetic field must be for this approximation to be valid.

In this chapter we present a novel computational method for solution of the linearized Vlasov equation that makes no assumptions about the magnetic field strength, and makes direct comparison to previous work by Dubin, and Hart and Spencer. Using the numerical Bernstein spectrum obtained from the code, we find that the 1/B expansion used by Dubin introduces a spurious shift of the local upper-hybrid frequency, leading to a significant shift of Dubin's predicted Bernstein mode frequencies away from the values obtained from our code. We resolve this issue by constructing a *new WKB theory*, which avoids taking the large magnetic field limit. The results of the Vlasov code and the new WKB theory are then compared, and better agreement is found between the mode frequencies obtained from the two methods. We also consider the effect of multiple species on the Bernstein mode spectrum, finding that wave-particle resonances will damp the waves if the impurity species concentrations are too large. We predict that for ongoing experiments at UCSD, where the modes are excited using applied oscillatory voltages on external electrodes, Bernstein modes will be easiest to observe in the majority species of a clean, hot plasma for azimuthal mode number $l = 2$. For $l = 1$ there is negligible Bernstein mode response to this type of excitation, and for $l = 0$ the Bernstein mode component to the plasma response is small and heavily damped. However, the $\ell = 0$ Bernstein frequencies predicted by our computations are the same as the results of Hart and Spencer[10].

2.2 Equilibrium

In this chapter, we assume throughout that the equilibrium plasma is a thermal equilibrium nonneutral plasma with uniform temperature T and uniform rotation frequency ω_r. We assume that the plasma consists of charge species all with positive charge q, in a uniform magnetic field in $-z$ direction of strength B. This choice of magnetic field direction implies that the plasma rotates in the positive θ direction (i.e. $\omega_r > 0$), and cyclotron motion is also a rotation in the positive θ direction with cyclotron frequency $\Omega = qB/(mc) > 0$. (If the plasma consists instead of negative charge species, the results in this chapter can be applied by assuming a magnetic field in the $+z$ direction.)

We will use nondimensionalized variables. Times are scaled by the central plasma frequency $\omega_p(r=0) = \sqrt{4\pi q^2 n(0)/m}$ associated with one plasma species of mass m and charge q, and lengths are scaled to the central Debye length $\lambda_D(r=0) = \sqrt{T/(4\pi q^2 n(0))}$ where here (and here alone) $n(r)$ is the unscaled plasma number density of the given species. Everywhere else, densities are scaled by the central equilibrium density $n(0)$. Masses of other species are scaled to the mass m. Electric potentials are also scaled via $\Phi = q\phi/T$, where ϕ is the unscaled electrostatic potential. This definition of Φ, along with the scaling of n gives, for a single-species plasma, the scaled Poisson's Equation $\nabla^2\Phi = -n$. These scalings imply the velocities are scaled by the thermal speed $v_T = \sqrt{T/m}$.

The thermal equilibrium density profile of the plasma satisfies Poisson's equation with the constraint that $n(r)$ is a Boltzmann distribution. For a single species plasma, write

$$n(r) = e^{\Psi(r)}, \tag{2.1}$$

where $\psi = -\Phi - \omega_r(\Omega - \omega_r)r^2/2$ is the negative of the (scaled) equilibrium potential energy as seen in a frame rotating with the plasma.[16] Then Poisson's equation reduces to

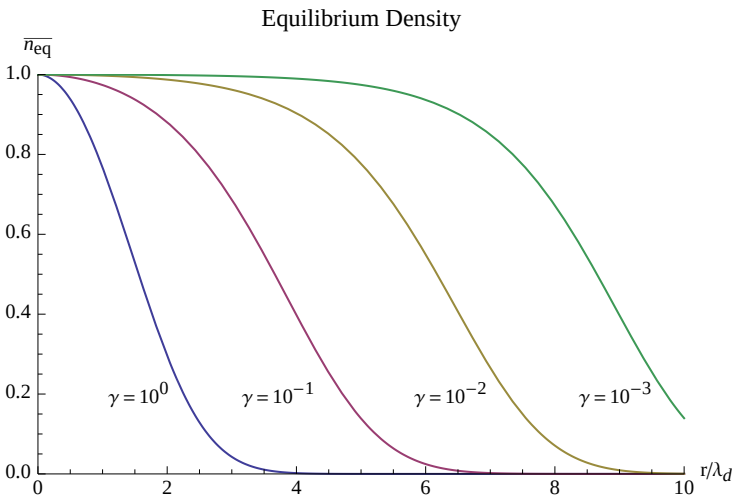

Figure 2.1: Equilibrium densities scaled by central density for various values of γ.

$$\frac{1}{r}\frac{\partial}{\partial r}\left[r\frac{\partial \psi}{\partial r}\right] = e^{\psi} - (1+\gamma), \tag{2.2}$$

where $\gamma \equiv 2\omega_r(\Omega - \omega_r) - 1$. Densities predicted by Eqs. (2.1) and (2.2) are displayed in FIG. 3.6 for a set of different γ values. As γ approaches zero, the plasma radius (measured in Debye lengths) increases.

In later work we will find it useful to define the equilibrium radius of the plasma r_p as

$$r_p = \sqrt{\int_0^{r_W} 2rn(r)\,dr} \tag{2.3}$$

This radius is equal to the radius of an imaginary "top-hat" plasma whose central density and total particle number (per unit axial length) are both equal to our plasma. In scaled units, there is a relationship between γ and r_p, good when $r_p \gg 1$:

$$r_p \sim 0.513 - \log\gamma + \frac{1}{2}\log\log 1/\gamma.$$

Consequently, γ parametrizes the scaled radius of the plasma, i.e. the number of Debye lengths across the column radius.

The equilibrium distribution function is a product of $n(r)$ and a rotating Maxwellian, which in our scaled units becomes

$$f_0(r,\mathbf{v}) = \frac{n(r)}{2\pi} \times \exp\left[-\frac{(\mathbf{v}-\omega_r r\hat{\theta})^2}{2}\right]. \tag{2.4}$$

For nonneutral plasmas containing multiple species, species with different masses can centrifugally-separate in the rotating plasma column, with heavier species pushed to the outside of the column by centrifugal force effects. According to the Boltzmann distribution, the ratio of densities between two species i and j is [15]

$$n_i(r)/n_j(r) = c_{i,j}\exp(-(m_i-m_j)\omega_r^2 r^2/2), \tag{2.5}$$

where $c_{i,j}$ is a constant depending on the overall concentration of the two species. Here, however, we will assume that the density ratio is close enough to a constant over the plasma profile so that centrifugal separation effects can be neglected. This is not a good approximation in some very low temperature experiments ($T < 10^{-4}$ eV) on ion plasmas at UCSD, but is a reasonably good approximation at higher temperatures where, as we will see, it is easier to see Bernstein modes. Thus, we will assume that each species has the same radial density profile, multiplied by a factor proportional to the overall concentration of that species.

2.3 Cold Fluid Theory of Cyclotron Waves

In this section we briefly review the general theory of cold fluid electrostatic waves in a plasma column. Readers interested in more detail should refer to the original work of Trivelpiece and Gould[20], as well as a more recent cold fluid theory of z-independent cyclotron waves developed by Gould[9, 8]. Temperature is assumed to be zero in this theory and the plasma equlibrium density is assumed to have an arbitrary radial dependence $n(r)$. The theory considers

cyclotron waves that are excited by oscillating an external electrode voltage at frequency ω. The electrode radius is $r = r_W$, and its voltage is oscillated to produce a potential on the electrode of the form $\delta\Phi_W e^{-i\omega t + i\ell\theta}$ where ℓ is an integer. For a single-species plasma, Gould derived a linear fluid theory for small amplitude waves, where the perturbed potential $\delta\Phi(r,\theta,t)$ is also proportional to $e^{-i\omega t + i\ell\theta}$, and satisfies the following boundary-value problem:

$$\nabla \cdot \varepsilon \nabla \delta\Phi = 0, \tag{2.6}$$

with a 2-dimensional dielectric tensor ε given by

$$\varepsilon = \mathbb{1} - \begin{bmatrix} 1 & \frac{-i\Omega_v}{\hat{\omega}} \\ \frac{i\Omega_v}{\hat{\omega}} & 1 + \frac{r\omega_f'\Omega_v}{\hat{\omega}^2} \end{bmatrix} X(\omega, r). \tag{2.7}$$

Here

$$X(\omega, r) = \frac{\omega_p^2}{\hat{\omega}^2 - \Omega_v(\Omega_v - r\omega_f')}, \tag{2.8}$$

where we have momentarily relaxed our scaled units, so that the dependence of X on the plasma frequency ω_p is apparent (in our scaled units $\omega_p^2 = n(r)$). The primes denote derivatives with respect to r, $\hat{\omega} = \omega - \ell\omega_f$ is the Doppler-shifted wave frequency as seen in a frame rotating with the plasma, $\Omega_v = \Omega - 2\omega_f$ is the "vortex frequency" (the cyclotron frequency shifted by the Coriolis force from rotation), and $\omega_f(r)$ is the cold-fluid rotation rate of the plasma (neglecting the thermal diamagnetic drift correction that affects ω_r), which is given by the solution of the quadratic equation

$$2\omega_f(\Omega - \omega_f) = \langle n \rangle_r. \tag{2.9}$$

Here $\langle n \rangle_r$ is the average equilibrium density within radius r given by

$$\langle n \rangle_r = \frac{2}{r^2} \int_0^r \bar{r} d\bar{r} n(\bar{r}). \tag{2.10}$$

Equation (2.6) is merely a restatement of the Maxwell's equation $\nabla \cdot \mathbf{D} = 0$, where the electric displacement vector is $\mathbf{D} = -\varepsilon \cdot \nabla \delta\Phi$.

Writing out Eq. (2.6) one obtains the following second order differential equation that must be solved for the wave potential $\delta\Phi$:

$$0 = \varepsilon_{11}\delta\Phi'' + \left(\frac{\varepsilon_{11}}{r} + \varepsilon'_{11}\right)\delta\Phi' + \left(\frac{i\ell}{r}\varepsilon'_{12} - \frac{\ell^2}{r^2}\varepsilon_{22}\right)\delta\Phi, \tag{2.11}$$

where again primes denote derivatives with respect to r. Here ε_{ij} refers to the i,jth component of the dielectric tensor. This equation is to be solved using the boundary conditions that at $r = 0$ the potential must remain finite, and at the surrounding electrode with radius $r = r_W$ the potential is $\delta\Phi(r_W) = \delta\Phi_W$.

Gould made further progress in obtaining the solution of Eq. (2.11) by taking a large magnetic field limit in order to simplify several terms. We will not use this approximation here because it introduces small but important errors in the solution. Instead, we solve Eq. (2.11) numerically. However, we will later find it useful to compare to the large field solution, so for completeness we provide the solution below. The general solution to the large-field ODE can be written analytically as a linear combination of two independent solutions:

$$\delta\Phi = Ar^{-\ell}\int^r d\bar{r}\frac{\bar{r}^{(2\ell-1)}}{D(\bar{r})} + Br^{-\ell}, \tag{2.12}$$

where $D(r)$ is the large-field form for ε_{11},

$$D = 1 - \frac{\omega_p^2/(2\Omega)}{\hat{\omega} - \Omega_v + r\omega'_f/2}, \tag{2.13}$$

and where the coefficients A and B are determined by the boundary conditions on the solution.[6]

For the simplest possible case of a uniform plasma completely filling the electrode volume out to $r = r_W$, Eq. (2.11) simply becomes $\varepsilon_{11}\nabla^2\delta\Phi = 0$. This implies that either the potential

satisfies Laplace's equation, so that there is no density perturbation (and no cyclotron wave) or else $\varepsilon_{11} = 0$, which is the dispersion relation for upper hybrid waves in the uniform plasma column. The frequency of these waves (as seen in the rotating frame) is the upper hybrid frequency, given by

$$\hat{\omega}^2 = \omega_p^2 + \Omega_v^2. \tag{2.14}$$

In a uniform plasma these upper hybrid oscillations can have any functional form, i.e. $\nabla^2\delta\Phi$ is not determined in cold fluid theory.

Another case that can be handled analytically is a uniform plasma column with radius r_p less than r_W. In this case there are surface waves in addition to the upper hybrid waves. The surface waves can be excited by the external electrode potential oscillation, i.e. they are driven to large amplitude if the external electrode potential oscillates at the surface wave frequency. The surface waves themselves have a potential of the form $\delta\Phi \propto r^\ell$ inside the plasma, and a frequency given by the solution of the equation

$$\ell(\varepsilon_{11} + i\varepsilon_{12}) = -\ell\frac{1 + (r_p/r_W)^{2\ell}}{1 - (r_p/r_W)^{2\ell}}. \tag{2.15}$$

This equation yields a quadratic equation for the wave frequency whose solution is

$$\hat{\omega} = \frac{\Omega_v}{2} \pm \sqrt{\frac{\Omega^2}{4} - \frac{\omega_p^2}{2}\left(\frac{r_p}{r_W}\right)^{2\ell}}. \tag{2.16}$$

The upper sign yields the frequency of the surface cyclotron wave, while the lower sign yields the frequency of the diocotron wave. When the magnetic field is large, the surface cyclotron frequency can can be approximated as

$$\hat{\omega} = \Omega_v + \frac{\omega_p^2}{2\Omega_v}\left[1 - \left(\frac{r_p}{r_W}\right)^{2\ell}\right]. \tag{2.17}$$

This surface mode frequency is greater than the vortex frequency but less than the upper hybrid frequency.

Both cyclotron and diocotron waves are incompressible distortions of the shape of the plasma column that rotate in θ with angular phase velocity given by $\hat{\omega}/\ell$, as seen in the frame of the plasma's rotation. These surface waves have finite multipole moments, which is why they can create a potential outside of the plasma that can be detected on the wall. For instance, for $\ell = 1$ the plasma center is shifted off-axis and rotates about the center of the trap at the wave phase velocity, while for $\ell = 2$ the plasma distorts into a uniform-density ellipse whose shape rotates about its center.

On the other hand, upper hybrid oscillations in the uniform plasma column cannot be detected, or excited, using wall potentials. For instance, an $\ell = 0$ upper hybrid oscillation corresponds to *any* cylindrically-symmetric radial velocity perturbation; such a perturbation will oscillate at the upper hybrid frequency of the column. This perturbation obviously conserves total charge, and therefore, by Gauss' law, creates no field outside the plasma that can be used to detect or excite the mode.

Similarly, upper hybrid oscillations internal to the plasma column can be found with any azimuthal mode number ℓ and (almost) arbitrary radial dependence (again assuming that the plasma column has uniform density). For instance, any initial $\ell = 1$ density perturbation of the form $\delta n(r)e^{i\theta}$, chosen so as not to change the center of mass location of the plasma (i.e. $\int_0^{r_p} d\bar{r}\bar{r}^2\delta n(\bar{r}) = 0$), will not create an $\ell = 1$ (dipole) moment and will therefore be unobservable from outside the plasma. This initial perturbation can then evolve in two ways, depending on the self-consistent initial velocity field. That part of the field which is curl-free evolves as an upper hybrid oscillation; that part which is divergence-free has zero frequency (as seen in the plasma's rotating frame). Although not the subject of this chapter, the zero-frequency modes are "convective cell" vortical motions that do not change the perturbed plasma density, by construction. There are an uncountable infinity of such degenerate upper hybrid oscillations and zero-frequency

convective cells, but only two surface modes (the diocotron and upper-hybrid branches). Only the surface modes are detectable, or excitable, from the wall.

For a nonuniform plasma column with density that smoothly approaches zero at some radius less than r_W, the surface mode and the continuum of upper hybrid oscillations now couple in an interesting (and nontrivial) way. (Something similar can happen with the diocotron surface mode and the zero-frequency modes.[18]). As the plasma density varies, the upper hybrid frequency varies and the spectrum of upper hybrid oscillations becomes a continuum that spans the range from the vortex frequency (where the density approaches zero) to the central upper hybrid frequency. This continuum includes the surface plasma frequency, and consequently the formerly discrete surface plasma eigenmode becomes a "quasimode";[18] i.e. it is no longer an undamped eigenmode of the system. However, there remains a damped plasma response to an external driver that consists of a phase-mixed potential response from the upper hybrid continuum, peaked around the former surface plasma frequency. This is a well-known form of spatial Landau-damping that has been discussed previously for other types of plasma waves, such as Langmuir waves [2] and Trivelpiece-Gould modes. [4] (Sidenote: $\ell = 0$ and $\ell = 1$ are exceptional cases. For $\ell = 0$ there is no surface plasma mode, and there is still no coupling between an external wall potential and the upper hybrid continuum (see Sec. VIII D); while for $\ell = 1$ the surface mode remains a discrete "center of mass" eigenmode, even for a nonuniform column.)

To describe the driven response of a nonuniform plasma column at frequencies near the cyclotron frequency, one must now solve Eq. (2.11) numerically in general (except for the $\ell = 0$ case, which can be calculated analytically, as we discuss later). However, notice that Eq. (2.11) has regular singular points for radii where ε_{11} vanishes, causing $\delta\Phi$ to diverge. This occurs when

$$X(\omega, r) = 1. \tag{2.18}$$

Note that this is the same condition we had when considering modes in a uniform plasma, resulting in upper-hybrid oscillations in Eq. (2.14). Accordingly, we define $r_{\mathrm{UH}}(\omega)$ to be a root of Eq. (2.18), which we refer to as an *upper-hybrid radius*.

For a single species plasma with a thermal equilibrium density profile, one can show that there is at most one solution to Eq. (2.18), $r = r_{\mathrm{UH}}(\omega)$. However, for multispecies plasmas, there can be more than one solution.

To understand the nature of the fluid theory divergences near an upper-hybrid radius, we perform asymptotic analysis on Eq. (2.11) near $r_{\mathrm{UH}}(\omega)$ in the case where terms of any order in $\frac{1}{r}$ are neglected. Dropping all such terms in Eq. (2.11), we obtain

$$\delta\Phi'' + \frac{\varepsilon_{11}'}{\varepsilon_{11}}\delta\Phi' = 0. \tag{2.19}$$

Under typical conditions, the root in Eq. (2.18) is first-order, that is, $X'(\omega, r_{\mathrm{UH}}) \neq 0$, so it is viable to expand $\varepsilon_{11}(r)$ around r_{UH}. We write

$$\varepsilon_{11} \sim \frac{1}{\mathcal{L}}(r - r_{\mathrm{UH}}), \tag{2.20}$$

with $\mathcal{L} \equiv 1/\varepsilon_{11}'(r_{\mathrm{UH}})$, so that Eq. (2.19) becomes

$$\delta\Phi'' + \frac{1}{r - r_{\mathrm{UH}}}\delta\Phi' = 0. \tag{2.21}$$

The order of the equation can be reduced, and the equation can be directly integrated:

$$\delta\Phi'(r) = \frac{A}{r - r_{\mathrm{UH}}}. \tag{2.22}$$

We should emphasize that Eq. (2.22) is only correct for r near r_{UH}, and should be regarded as the first term in a series expansion of $\delta\Phi'$ about the point r_{UH}. The next-order terms in the expansion

are proportional to $\log(r/r_{\rm UH}-1)$, a constant of order unity, and so on.

We would like to integrate this expression to obtain $\delta\Phi(r)$. However, the divergence at $r = r_{\rm UH}$ requires careful consideration of the physics: in any physical plasma there will be a small effect from particle collisions, causing waves to damp. Later in the chapter, we introduce a simple Krooks model of collisions. This model has the effect of replacing the frequency ω by $\omega + i\nu$ in Eqs. (2.6) - (2.18), where ν is the collision rate. This in turn implies that $r_{\rm UH}$, the root of the modified Eq. (2.18), $X(\omega+i\nu,r)=1$, is complex. For small ν a Taylor expansion of this equation implies that the imaginary part of $r_{\rm UH}$ is

$$Im(r_{\rm UH}) = -\nu\frac{\partial X/\partial\omega}{\partial X/\partial r}|_{r_{\rm UH0}} = \nu\frac{\partial r_{\rm UH0}}{\partial\omega} = -\frac{2\hat{\omega}\nu}{\omega_p^2\partial\varepsilon_{11}/\partial r} \equiv \Delta r \tag{2.23}$$

where $r_{\rm UH0}$ and Δr are the real and imaginary parts of the upper hybrid radius respectively:

$$r_{\rm UH} = r_{\rm UH0} + i\Delta r, \tag{2.24}$$

and the last form for Δr in Eq. (2.23) follows by substitution for X from Eqs. (2.7), (2.8) and (2.18). The sign of Δr can be either positive or negative depending on the sign of the radial gradient of ε_{11}. The effect of this in integrating Eq. (2.22) is to move the pole at $r_{\rm UH}$ slightly away from the real r axis, allowing integration around the pole:

$$\delta\Phi(r) = A\log\big(\frac{r_{\rm UH}-r}{r_{\rm UH}-r_0}\big) + \delta\Phi(r_0), \tag{2.25}$$

where r_0 is a radius below the cutoff radius, and both r and r_0 are close enough to the upper hybrid radius to make Eq. (2.20) as good approximation. The coefficient A is given here by matching to the derivative of the potential using Eq. (2.22):

$$A = -\delta\Phi'(r_0)(r_{\rm UH}-r_0) \tag{2.26}$$

The logarithmic divergence of the perturbed potential near the upper hybrid radius can be seen in FIG. 2.2 for several different scaled frequencies λ, [8] where

$$\lambda = \frac{\omega - \Omega}{\omega_E}, \tag{2.27}$$

and where $\omega_E \equiv 1/(2\Omega)$ is the $E \times B$ equilibrium rotation rate at the center of the plasma column (in our dimensionless units). (This frequency scaling is useful because the plasma response to the forcing is largest for frequencies ω for which λ is of order unity. The fluid rotation rate ω_f, given by Eq. (2.9), differs from ω_E at the column center in that it includes the $F \times B$ drift from centrifugal force effects, but this difference is typically small.) As shown in FIG. 2.2, the logarithmic divergence changes radius as λ varies because the upper hybrid radius is a function of frequency through Eq. (2.18).

The potential picks up an imaginary part, as shown in FIG. 2.2, even for small ν because, for $r > r_{\mathrm{UH0}}$, the real part of the argument of the logarithm in Eq. (2.25) changes sign:

$$\delta\Phi(r) = A \log\left(\frac{r - r_{\mathrm{UH}}}{r_{\mathrm{UH}} - r_0}\right) + \delta\Phi(r_0) + i\pi A \mathrm{Sign}(\Delta r). \tag{2.28}$$

Next, using the Plemelj formula, we evaluate the limit as $\delta r \to 0$:

$$\begin{aligned}
\delta\Phi(r) &= -i\pi A h(r - r_{\mathrm{UH0}}) + \mathcal{P}\int_{r_0}^{r} \frac{A\, dr'}{r' - r_{\mathrm{UH0}}} + \delta\Phi(r_0) \\
&= -i\pi A h(r - r_{\mathrm{UH0}}) + A \log\left|\frac{r - r_{\mathrm{UH}}}{r_0 - r_{\mathrm{UH0}}}\right| + \delta\Phi(r_0),
\end{aligned}$$

where $h(x)$ is the Heaviside step function. Due to the step function this integral takes a different form for $r < r_{\mathrm{UH}}$ compared to $r > r_{\mathrm{UH}}$. For $r < r_{\mathrm{UH}}$, we have

$$\delta\Phi^{-}(r) = A \log\left(\frac{r_{\mathrm{UH0}} - r}{r_{\mathrm{UH0}} - r_0}\right) + \delta\Phi(r_0), \tag{2.29}$$

while for $r > r_{\mathrm{UH}0}$, the solution is

$$\delta\Phi^{+}(r) = -i\pi A + A\log\left(\frac{r - r_{\mathrm{UH}0}}{r_{\mathrm{UH}0} - r_0}\right) + \delta\Phi(r_0) \tag{2.30}$$

Note that these two equations can be written at once by carefully specifying the branch cut of the logarithm so that $\log(-y) = i\pi + \log(y)$, for $y > 0$:

$$\delta\Phi(r) = A + B\log(r - r_{\mathrm{UH}}). \tag{2.31}$$

With this interpretation, the additive offset encountered by circumnavigating the pole at $r = r_{\mathrm{UH}}$ is accounted for quite naturally by the behavior of the logarithm when the argument switches sign. A solution for the perturbed potential beyond the upper hybrid radius can now be obtained by integrating Eq. (2.11) from $r = 0$ (with $\delta\Phi(0) = 0$), up to $r = r_{\mathrm{UH}} - \Delta r$ (i.e. just before the upper hybrid radius, with $\Delta r \to 0^{+}$)), and then using Eqs. (2.29) and (2.30) to write $\delta\Phi(r_{\mathrm{UH}} + \Delta r) - \Delta\Phi(r_{\mathrm{UH}} - \Delta r) = -i\pi A$ and $\delta\Phi'(r_{\mathrm{UH}} - \Delta r) = -\delta\Phi'(r_{\mathrm{UH}} + \Delta r) = -A/\Delta r$. This allows us to determine a jump condition relating the perturbed potential and its derivative just before and just after the upper-hybrid radius:

$$\begin{aligned} \delta\Phi^{+} &= \delta\Phi^{-} + i\pi\Delta r\,\frac{\partial\delta\Phi}{\partial r}^{-}, \\ \frac{\partial\delta\Phi}{\partial r}^{+} &= -\frac{\partial\delta\Phi}{\partial r}^{-}, \end{aligned} \tag{2.32}$$

where the notation $\delta\Phi^{-}$ and $\delta\Phi^{+}$ is the perturbed potential evaluated at $r_{\mathrm{UH}} + \Delta r$ and $r_{\mathrm{UH}} - \Delta r$ respectively. These formulae allow numerical integration of Eq. (2.11) through the divergence, by taking Δr small but finite. Note that Eq. (2.22) implies that $\Delta r\partial\Phi^{-}/\partial r$ is finite as Δr approaches zero. Physically, the fact that the perturbed potential has an imaginary part when $\nu \to 0$ is due to a collisionless damping mechanism: at the upper hybrid radius, the driven potential oscillation is resonant with a radially-localized upper hybrid oscillation. Unlike the uniform plasma case

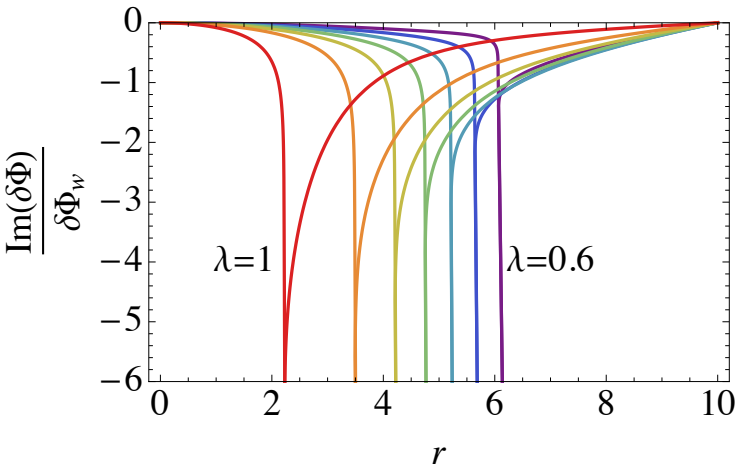

Figure 2.2: Radial dependence of the imaginary part of the perturbed potential $\mathrm{Im}\{\delta\Phi(r)\}$ driven at frequencies from $\lambda = 1$ (red) down to $\lambda = 0.6$ (violet) in equal steps. $r_p = 4.76$, $r_W = 10$, $\ell = 2$, $\Omega = 5$ and $\nu \to 0^+$.

discussed previously, this resonant upper-hybrid oscillation can be excited by the external driving. The excitation requires energy that damps the oscillation, and is responsible for the imaginary (out-of phase) potential response. This type of collisionless damping from linear mode-coupling between a surface wave and an upper hybrid oscillation is a well-known form of spatial Landau-damping that has been discussed previously for other types of plasma waves, such as Langmuir waves [2] and Trivelpiece-Gould modes.[4] Later, when finite temperature effects are added to the theory, the continuous spectrum of upper hybrid oscillations, with variable frequency depending on the local plasma density, will be found to break into a discrete spectrum of finite-temperature Bernstein oscillations. The Bernstein oscillations also couple to the surface wave at the upper hybrid radius, in much the same way as described here.

In FIG. 2.2 we plot $\mathrm{Im}\{\delta\Phi(r)\}/\delta\Phi_W$ for various driving frequencies with mode number $\ell = 2$, assuming a single species plasma with density profile given by the solution of Eq. (2.2), for $r_p = 4.76$ as given by Eq. (2.2),and $r_W = 10$. This can be interpreted as the (imaginary part of the) perturbed potential driven at unit wall amplitude. The imaginary part of the wave potential was taken to eliminate the contribution from the wall potential. To determine a resonant surface mode frequency using these results, we consider a dimensionless measure of the plasma response

Y, the admittance function, defined as

$$Y = \left. \frac{r_W \frac{\partial \delta\Phi}{\partial r}}{\delta\Phi} \right|_{r=r_W} . \tag{2.33}$$

Notice that a cylinder containing no plasma is a simple capacitor, which has purely imaginary

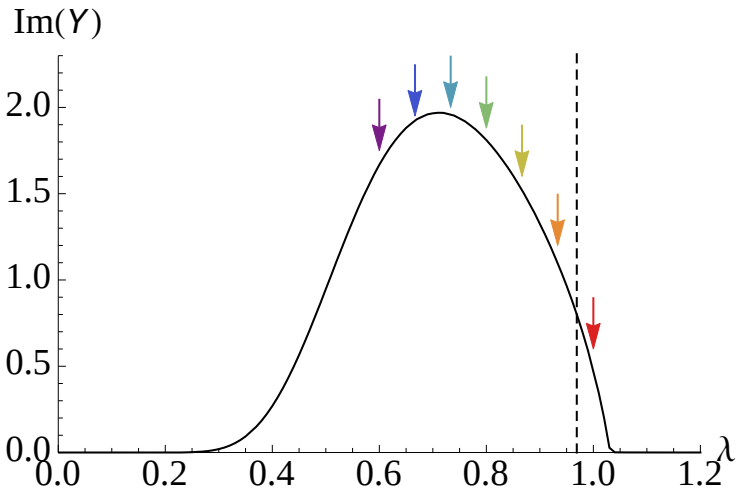

Figure 2.3: A plot of $\mathrm{Im}(Y)$ driven at various frequencies, for the plasma parameters of FIG. 2.2. The colored arrows correspond to the potentials shown in FIG. 2.2. The dashed line is discussed in the text.

experimental admittance (the ratio of current to voltage). Consequently, our theoretical definition of Y for a vacant cylinder will be purely real (the surface charge on the electrode, proportional to $\partial\delta\Phi/\partial r|_{rw}$, is the time integral of the current). We conclude that the imaginary part of Y is due to the presence of plasma, so for the remainder of this chapter we will focus on $\mathrm{Im}(Y)$. For the potential data in FIG. 2.2, the admittance function is plotted in FIG. 2.3. This data shows a broad peak, caused by the mixing of the continuum of upper hybrid oscillations and the surface mode, turning the surface mode into a damped quasimode. The width in this peak decreases as the plasma edge becomes sharper (i.e. as temperature decreases holding the plasma radius r_p fixed), approaching a delta function at the surface cyclotron wave frequency given by Eq. (2.16) (the dashed line), when the plasma density approaches a step function with radius r_p.[6]

At this point, we should reflect on the agreement of FIG. 2.2 with the existing fluid

theory in the literature for a uniform plasma with a sharp edge in the highly magnetized limit. In that case, $\delta\Phi = Ar^{\ell}$ inside the plasma, and $\delta\Phi = Br^{\ell} + Cr^{-\ell}$ outside, with appropriately chosen coefficients to match boundary conditions at the plasma edge where $\delta\Phi$ is continuous, and at the wall, where $\delta\Phi = 0$. The result is a perturbed potential that is maximized at the plasma radius where $\delta\Phi'(r)$ is discontinuous. Figure 2.2 resembles this solution, with a difference: the location of the upper-hybrid radius is variable, where in the top-hat plasma it does not make an appearance as it is buried in the edge. Then for the plasma studied in FIG. 2.2, the simple analytic fluid solution outlined above is only valid away from the plasma edge where the density is changing. In the limit as the plasma edge width goes to zero, the simple analytic form is valid all the way up to the plasma edge, and the region of the logarithmic behavior is pinched out of existence. As the driving frequency increases, the location of the logarithmic divergence (rounded out by finite ν) at the upper-hybrid radius becomes closer to the center of the plasma. Because the divergence moves toward the plasma center where the density profile is nearly uniform, $\varepsilon'_{11}(r)$ is nearly zero, suppressing the divergent term in Eq. (2.19). Similarly, for smaller driving frequencies, the divergence moves toward the plasma edge, where again $\varepsilon'_{11}(r)$ is nearly zero, and a similar phenomenon occurs. Consequently, there is a range of frequencies where the upper-hybrid divergence is most prominent. The width in frequency response of the surface cyclotron mode has been studied in earlier work[6], and was found to become broader as the physical width of the plasma edge widens, as well as the damping ν decreases. However, even at $\nu = 0^{+}$, the surface cyclotron mode response has finite width due to energy absorption in the plasma edge where the driving frequency matches the local upper-hybrid frequency. The plasma response While this fluid theory can be used to predict the cyclotron mode frequency, it predicts no Bernstein modes. These modes only appear in a kinetic theory which will be studied next.

2.3.1 Determination of Mode frequencies

To determine the resonant frequencies, we take a cue from the experimentalists and measure the *admittance* (per unit length along z) of the plasma. This quantity is defined experimentally by

$$Y_{\text{exp}} = \frac{I}{V},$$

where V is the applied electrode voltage, and I is the resulting (line density) current through the electrode. A potential of the appropriate θ dependence is applied to some finite number of wall electrodes. However, for theoretical purposes we instead imagine the wall composed of an infinite number of infinitesimal electrodes, and apply a voltage $V \sim e^{i\ell\theta}$. Consequently, in this limit the current into any electrode vanishes, so we are instead interested in the *angular admittance density*, defined by

$$y = \frac{dY_{\text{exp}}}{d\theta} = \frac{j}{V},$$

where $j = \frac{dI}{d\theta}$ is the angular current density. The potential in the vicinity of the wall electrodes (where there is no plasma) satisfies Laplace's Equation; integrating this equation from $r = r_W - \varepsilon$ to $r = r_W + \varepsilon$ gives

$$2\pi\sigma = \left.\frac{\partial\delta\Phi}{\partial r}\right|_{r=r_W},$$

where σ is the surface charge density on the wall. From the continuity equation there is a relationship between σ and j:

$$-i\omega\ r_W \left.\frac{\partial\delta\Phi}{\partial r}\right|_{r=r_W} = 2\pi j,$$

so we find that the admittance density is given by

$$y = \frac{-i\omega}{2\pi} Y, \tag{2.34}$$

where Y is a dimensionless plasma response that appears in the literature defined by

$$Y = \left. \frac{r_W \frac{\partial \delta\Phi}{\partial r}}{\delta\Phi} \right|_{r=r_W}. \tag{2.35}$$

Notice that a cylinder containing no plasma is a simple capacitor, which has purely imaginary experimental admittance. Consequently, our theoretical definition of Y for a vacant cylinder will be purely real due to the relative factor of i in Eq. (2.34). We conclude that the imaginary part of Y is due to the presence of plasma, so for the remainder of this chapter we will always make comparisons of $\mathrm{Im}(Y)$.

2.4 Vlasov Solution

So far the theory has neglected thermal effects responsible for Bernstein modes. In this section we will develop a numerical approach that keeps these thermal effects. At low temperatures the method predicts admittance functions that approach the cold-fluid theory, but at higher temperatures Bernstein modes appear as separated peaks in the admittance.

We will develop a numerical method for solution of the linearized Vlasov equation in cylindrical coordinates. In cylindrical coordinates the Vlasov equation for the distribution function $f(r,\theta,v_r,v_\theta,t)$ is:

$$\frac{\partial f}{\partial t} + v_r \frac{\partial f}{\partial r} + \frac{v_\theta}{r}\left(\frac{\partial f}{\partial \theta} - v_r \frac{\partial f}{\partial v_\theta} + v_\theta \frac{\partial f}{\partial v_r}\right) + (-\Omega v_\theta + E_r)\frac{\partial f}{\partial v_r} + (\Omega v_r + E_\theta)\frac{\partial f}{\partial v_\theta} = 0, \tag{2.36}$$

with boundary condition at $r = 0$ given by

$$\left. \frac{\partial f}{\partial \theta} - v_r \frac{\partial f}{\partial v_\theta} + v_\theta \frac{\partial f}{\partial v_r} \right|_{r=0} = 0,$$

and $f \to 0$ as $r \to \infty$ and when $|\mathbf{v}| \to \infty$. The condition at $r = 0$ keeps the third term in Eq. (2.36)

from diverging, and physically enforces continuity in f. We will study linear perturbations away from the thermal equilibrium discussed in section 1. First, we will change velocity coordinates via $v = \sqrt{{v_r}^2 + {v_\theta}^2}$, $\tan\psi = \frac{v_\theta}{v_r}$, where v is the magnitude of the velocity, and ψ is the *gyroangle*, or the angle of the velocity relative to the radial direction $\hat{r}$. This gives

$$\begin{aligned} 0 =& \frac{\partial f}{\partial t} + v\cos\psi\frac{\partial f}{\partial r} + \frac{v\sin\psi}{r}\left(\frac{\partial f}{\partial\theta} - \frac{\partial f}{\partial\psi}\right) + \Omega\frac{\partial f}{\partial\psi} \\ &+ (E_r\cos\psi + E_\theta\sin\psi)\frac{\partial f}{\partial v} + \left(\frac{-E_r\sin\psi + E_\theta\cos\psi}{v}\right)\frac{\partial f}{\partial\psi}. \end{aligned} \tag{2.37}$$

In this form, the boundary conditions simplify to

$$\begin{aligned} \frac{\partial f}{\partial\theta} - \frac{\partial f}{\partial\psi} &= 0,\ r = 0; \\ \frac{\partial f}{\partial\psi} &= 0,\ v = 0; \\ f &\to 0,\ r, v \to \infty. \end{aligned} \tag{2.38}$$

Next, we linearize the equation in the usual way: $f = f_0 + \delta f$, where f_0 is a time-independent solution to the non-linear equation. Since the electric potential is determined by both the external wall potential as well as the charge density in the plasma itself, the electric potential is also expanded as $\phi = \Phi_0 + \delta\Phi$ and similarly for the electric field: $\mathbf{E} = \mathbf{E}_0 + \delta\mathbf{E}$. The equilibrium plasma density is azimuthally symmetric, so we also use $E_{\theta_0} = 0$. Self-consistent magnetic effects are neglected in this treatment, so we omit the $\delta\Omega$ term. Here we will take f_0 to

be the thermal equilibrium solution Eq. (2.4) solved in section 1.

$$\begin{aligned}0 =&\frac{\partial \delta f}{\partial t} + v\cos\psi\frac{\partial \delta f}{\partial r} + \frac{v\sin\psi}{r}\left(\frac{\partial \delta f}{\partial \theta} - \frac{\partial \delta f}{\partial \psi}\right) + \Omega\frac{\partial \delta f}{\partial \psi}\\ &+E_{r0}\left(\cos\psi\frac{\partial \delta f}{\partial v} - \frac{\sin\psi}{v}\frac{\partial \delta f}{\partial \psi}\right) + (\delta E_r\cos\psi + \delta E_\theta\sin\psi)\frac{\partial f_0}{\partial v}\\ &+\left(\frac{-\delta E_r\sin\psi + \delta E_\theta\cos\psi}{v}\right)\frac{\partial f_0}{\partial \psi}.\end{aligned} \tag{2.39}$$

The last term involving a ψ derivative is cumbersome. To remove it, we transform into the co-rotating frame with angular frequency ω_r. This effects the transformation $\Omega \to \Omega_v$, $E_{r_0} \to E_{r_0} + \omega_r(\omega_r - \Omega)r \equiv F_{r_0}$. In these coordinates, $\frac{\partial f_0}{\partial \psi} = 0$ (i.e. where $\tan\psi = \bar{v}_\theta/v_r$, with $\bar{v}_\theta$ measured in the rotating frame), eliminating the last term in Eq. (2.39). Future appearances of v_θ will be understood to be measured in the rotating frame.

We next Fourier analyze in ψ, θ, and t, via

$$\begin{aligned}\delta f(r,\theta,v_r,v_\theta;t) &= e^{-i\omega t + i\ell\theta}\sum_{n=-\infty}^{\infty}\delta f_n(r,v)\, e^{in\psi},\\ \delta\Phi(r,\theta;t) &= \delta\Phi(r)e^{-i\omega t + i\ell\theta},\end{aligned} \tag{2.40}$$

where we refer to n as the *gyroharmonic number*. Finally, at this point we introduce a Krooks collision term to introduce damping into the system, by adding a term $\nu\,\delta f_n$, driving the plasma back to equilibrium. This has the effect of broadening the frequency response, allowing comparison to experiment, and making discrete Bernstein modes visible numerically. The resulting equation becomes

$$\begin{aligned}0 =&(-i\omega+\nu)\delta f_n + \hat{L}_{n,m}\delta f_m\\ =&(-i\omega+\nu)\delta f_n + \hat{L}_{0n,m}\delta f_m + v f_0\left(\frac{\partial\delta\Phi}{\partial r}\frac{\delta_n^1+\delta_n^{-1}}{2} + \frac{\ell\delta\Phi}{r}\frac{\delta_n^1-\delta_n^{-1}}{2}\right),\end{aligned} \tag{2.41}$$

where the second equality gives a definition for the operator $\hat{L}_{n,m}$, and the operator $\hat{L}_{0m,n}$ is defined

as

$$\hat{L}_{0n,m}\delta f_m = \frac{v}{2}\left(\frac{\partial \delta f_{n-1}}{\partial r} + \frac{\partial \delta f_{n+1}}{\partial r}\right) + \frac{v}{2r}\left[(\ell+1-n)\,\delta f_{n-1} - (\ell-1-n)\,\delta f_{n+1}\right] + i(\ell\omega_r - n\Omega_v)\delta f_n$$
$$+ \frac{F_{r_0}}{2}\left[\frac{\partial \delta f_{n-1}}{\partial v} + \frac{\partial \delta f_{n+1}}{\partial v} - \frac{(n-1)\delta f_{n-1} - (n+1)\delta f_{n+1}}{v}\right]. \tag{2.42}$$

Recalling the boundary conditions Eq. (2.38), and applying Eq. (2.40), the boundary conditions become

$$\begin{aligned} &\delta f_n(0,v) = 0, n \neq \ell; \\ &\delta f_n(r,0) = 0, n \neq 0; \\ &\delta f_n(r,v) \to 0, \;\; r,v \to \infty. \end{aligned} \tag{2.43}$$

The first and second conditions are unconstrained when $n = \ell$ and $n = 0$, respectively. Notice that Eq. (3.32) does not constitute a closed system for δf, since $\delta\Phi$ also appears. We close the system by introducing Poisson's equation (in our units), linearizing just as we did above:

$$\nabla_\ell{}^2 \delta\Phi = -\delta n, \tag{2.44}$$

$$\delta n \equiv \int d^2v\, \delta f = 2\pi \int dv\, v\, \delta f_{n=0}, \tag{2.45}$$

where the final identity comes from integrating Eq. (2.40), where all but the $n = 0$ term drops out.

To drive the plasma with $\ell \neq 0$ forcing, a forcing potential on the wall $\delta\Phi_W(r_W, \theta; t) = \delta\Phi_W e^{-i\omega t + i\ell\theta}$ is introduced (expressed here with full θ and t dependence), which serves as a boundary condition for Poisson's equation, namely that $\delta\Phi(r_W) = \delta\Phi_W$. (We discuss $\ell = 0$ forcing in Sec. VIII D.) We facilitate the solution by splitting the perturbed potential into a sum: $\delta\Phi = \delta\Phi_{\rm H} + \delta\Phi_p$, where $\delta\Phi_{\rm H}$ satisfies Laplace's (homogeneous) equation $\nabla_\ell^2 \delta\Phi_{\rm H} = 0$ subject

to $\delta\Phi_{\rm H}(r_W) = \delta\Phi_W$, with solution $\delta\Phi_{\rm H} = \delta\Phi_W (r/r_W)^\ell$, and the plasma potential $\delta\Phi_p$ satisfies the (inhomogeneous) Poisson's equation $\nabla^2_\ell \delta\Phi_p = -n$, with Dirichlet boundary conditions. By rewriting our equation in terms of $\delta\Phi_p$, $\delta\Phi_{\rm H}$ appears as a source term, so Eq. (3.32) becomes

$$\left[(-i\omega+\nu)\delta_{n,m} + \hat{L}_{{\rm p}n,m}\right] \delta f_m = -v f_0 \left(\frac{\partial \delta\Phi_{\rm H}}{\partial r} \frac{\delta^1_n + \delta^{-1}_n}{2} + \frac{\ell \delta\Phi_{\rm H}}{r} \frac{\delta^1_n - \delta^{-1}_n}{2} \right), \tag{2.46}$$

where $\hat{L}_{\rm p}$ specifies that the terms proportional to $\delta\Phi$ in $\hat{L}$ of Eq. (3.32) are to be replaced with $\delta\Phi_p$ (that is, they solve Poisson's equation with Dirichlet boundary conditions). The resulting linearized Vlasov equation, along with Poisson's equation and the definition of δn is

$$\begin{aligned} \left[(-i\omega+\nu)\delta_{n,m} + \hat{L}_{{\rm p}n,m}\right] \delta f_m &= -\frac{\ell\, r^{\ell-1} v\, f_0\, \delta\Phi_W\, \delta^1_n}{{r_{\rm w}}^\ell}, \\ 2\pi \int dv\, v\, \delta f_{n=0} - \delta n &= 0, \\ \nabla^2_\ell \delta\Phi_p + \delta n &= 0. \end{aligned} \tag{2.47}$$

We now regard Eq. (2.47) as a system of equations in the coordinates of the functions δf_n, δn, $\delta\Phi_p$, written in some basis. The equations have been expressed so that the terms linear in the variables appear on the left-hand side, while sources appear on the right-hand side. For the numerical work considered here, the basis chosen is obtained simply by discretizing the phase space variables r and v. The explicit discretization used will be discussed in Section 2.4.1.

The reader may wonder why $\delta\Phi_p$ appearing in Eq. (3.32) wasn't simply expressed in terms of Green's functions, which are themselves functions of δn, and therefore δf. We originally approached the problem this way, but when we began calculating on high-resolution grids we found that the non-local nature of the Green's function (in both space and velocity variables) introduced terms connecting every $n = 0$ grid point to every other, making the resulting matrix equation extremely dense. While treating δf, δn, and $\delta\Phi_p$ may appear redundant, the sparsity obtained by introducing a local Poisson's equation rather than non-local Green's function relations

far outweighs the marginally increased size of the matrix equation.

We now show that $\hat{L}_0$ is anti-Hermitian with respect to the inner product

$$\big(a,b\big) \equiv \sum_{n=-\infty}^{\infty} \langle a_n | b_n \rangle, \tag{2.48}$$

where

$$\langle a_n | b_n \rangle \equiv \int_0^\infty r\, dr \int_0^\infty v\, dv\; a_n^*(r,v)\; b_n(r,v). \tag{2.49}$$

The anti-Hermitian property ensures that, in the absence of self-consistent effects, normal mode frequencies are purely real. This is to be expected, since $\hat{L}_0$ describes a plasma of test charges moving in a background field, which should not have modes that grow or decay indefinitely. On the other hand, if a numerical method were employed that does not satisfy this anti-Hermitian property, spurious growth or decay of modes could occur. This possibility will be addressed when we discuss the discretization of the equations.

To prove the anti-Hermitian property, we rewrite $\hat{L}_0$ by rewriting r and v derivatives using

$$\begin{aligned}
\frac{\partial f_n}{\partial r}(r,v) &= \frac{1}{\sqrt{r}}\frac{\partial}{\partial r}\left[\sqrt{r}\, f_n(r,v)\right] - \frac{1}{2r}\, f_n(r,v), \\
\frac{\partial f_n}{\partial v}(r,v) &= \frac{1}{\sqrt{v}}\frac{\partial}{\partial v}\left[\sqrt{v}\, f_n(r,v)\right] - \frac{1}{2v}\, f_n(r,v),
\end{aligned}$$

which gives

$$\begin{aligned}
\hat{L}_{0n,m} f_m =& \frac{v}{2}\left(\frac{1}{\sqrt{r}}\frac{\partial}{\partial r}\left[\sqrt{r}(\delta f_{n-1} + \delta f_{n+1})\right] + \frac{(\ell + 1/2 - n)\,\delta f_{n-1} - (\ell - 1/2 - n)\,\delta f_{n+1}}{r} \right) \\
&+ i(\ell\omega_r - n\Omega_v)\delta f_n \\
&+ \frac{F_{r_0}}{2}\left(\frac{1}{\sqrt{v}}\frac{\partial}{\partial v}\left[\sqrt{r}(\delta f_{n-1} + \delta f_{n+1})\right] - \frac{(n - 1/2)\delta f_{n-1} - (n + 1/2)\delta f_{n+1}}{v} \right).
\end{aligned} \tag{2.50}$$

We now form the inner product $\big(g, \hat{L}_0 f\big)$. We then apply the following identities, proved through

integration by parts:

$$\left\langle g_m \middle| \frac{1}{\sqrt{r}} \frac{\partial}{\partial r} \left[\sqrt{r}\, f_n\right] \right\rangle = -\left\langle \frac{1}{\sqrt{r}} \frac{\partial}{\partial r} \left[\sqrt{r}\, g_m\right] \middle| f_n \right\rangle \tag{2.51}$$

$$\left\langle g_m \middle| \frac{1}{\sqrt{v}} \frac{\partial}{\partial v} \left[\sqrt{v}\, f_n\right] \right\rangle = -\left\langle \frac{1}{\sqrt{v}} \frac{\partial}{\partial v} \left[\sqrt{v}\, g_m\right] \middle| f_n \right\rangle \tag{2.52}$$

$$\left\langle g_n \middle| \left(\ell - n + \frac{1}{2}\right) f_{n-1} - \left(\ell - n - \frac{1}{2}\right) f_{n+1} \right\rangle = -\left\langle \left(\ell - n + \frac{1}{2}\right) g_{n-1} - \left(\ell - n - \frac{1}{2}\right) g_{n+1} \middle| f_n \right\rangle, \tag{2.53}$$

which demonstrate that all terms appearing in $\hat{L}_0$ are anti-Hermitian: $\left(g, \hat{L}_0 f\right) = -\left(\hat{L}_0 g, f\right)$.

2.4.1 Numerical Grid

The next step is to put Eq. (3.32) on a grid to be solved computationally. First, we only keep a finite number of gyroharmonics in the solution, $|n| < M_\psi$ for a given integer M_ψ chosen to be sufficiently large to yield convergent results (more on this later). For n-values beyond this range we set $\delta f_n = 0$. We choose a uniform radial grid with $r_i = i\Delta r$, $i = 0, 1, 2, ..., M_r$, and a uniform grid in speed v with $v_j = j\Delta v$, $j = 0, 1, 2, ..., M_v$, writing $\delta f_n(r_i, v_j) \equiv \delta f^n_{i,j}$. The maximum radius $R_{max} = M_r \Delta r$ is chosen to be just outside the plasma, and the maximum speed $V_{max} = M_v \Delta v$ is chosen to be roughly 4 thermal speeds, i.e. in scaled units $V_{max} \approx 4$. We discretize the operator using second-order-accurate centered-differences for the derivatives in r and v.

However, this introduces small, unphysical errors because the discretized operator $\hat{L}_{0n,m}$ is no longer anti-Hermitian. These errors can have the effect of destabilizing the equations, creating instabilities that result in spurious grid-scale oscillations in the wave potential and unphysical peaks in the admittance. This can be ameliorated by carefully choosing a discretization scheme that preserves the anti-Hermitian property as much as possible. One such method rewrites the radial derivatives in Eq. (2.42) as $\partial f/\partial r = (1/r)\partial(rf)/\partial r - f/r$, and similarly for the v-derivatives , then center-differences these derivatives while averaging some terms over neighboring grid-

points in r and v, as in the Lax method.[5] With this modification the differenced Eq. (3.32) becomes

$$\begin{aligned}
&\frac{v_j}{2r_i}\left(\frac{r_{i+1}(\delta f^{n+1}_{i+1,j}+\delta f^{n-1}_{i+1,j})-r_{i-1}(\delta f^{n+1}_{i-1,j}+\delta f^{n-1}_{i-1,j})}{2\Delta r}-\frac{n}{2}(\delta f^{n-1}_{i+1,j}-\delta f^{n+1}_{i+1,j}+\delta f^{n-1}_{i-1,j}-\delta f^{n+1}_{i-1,j})+\ell(\delta f^{n-1}_{i,j}-\delta f^{n+1}_{i,j})\right)\\
&+\frac{F_{r0}i}{2v_j}\left(\frac{v_{j+1}(\delta f^{n+1}_{i,j+1}+\delta f^{n-1}_{i,j+1})-v_{j-1}(\delta f^{n+1}_{i,j-1}+\delta f^{n-1}_{i,j-1})}{2\Delta v}-\frac{n}{2}(\delta f^{n-1}_{i,j+1}-\delta f^{n+1}_{i,j+1}+\delta f^{n-1}_{i,j-1}-\delta f^{n+1}_{i,j-1})\right)\\
&+\frac{v_j f_{0i,j}}{2}\left(\frac{\delta\Phi_{i+1}-\delta\Phi_{i-1}}{2\Delta r}\left(\delta_{n,1}+\delta_{n,-1}\right)+\frac{\ell\delta\Phi_i}{r_i}\left(\delta_{n,1}-\delta_{n,-1}\right)\right)+i(\ell\omega_r+n\Omega_v-\omega-i\nu)\delta f^n_{i,j}=-\frac{\ell r_i^{\ell-1}v_j f_{0i,j}\delta\Phi_W\delta^1_n}{r_w^\ell}.
\end{aligned} \tag{2.54}$$

In both the first and second lines, the two terms proportional to n are written as the average over their neighboring gridpoints in r and v respectively, which is correct as the grid size approaches zero. Using the discretized version of Eq. (2.48), where the integrals are replaced with a Simpson's rule Riemann sum, this discretized Vlasov equation is also anti-Hermitian in the absence of the self consistent $\delta\Phi_p$ term, respecting the anti-Hermiticity of the continuous equation. This equation forms a closed linear inhomogeneous system of equations when combined with discretized forms of the density relation and Poisson's equation shown below:

$$2\pi\sum_{j=0}^{M_v-1}\frac{1}{2}(v_j\delta f^0_{i,j}+v_{j+1}\delta f^0_{i,j+1})-\delta n_i=0, \tag{2.55}$$

$$\frac{\delta\Phi_{i+1}-2\delta\Phi_i+\delta\Phi_{i-1}}{\Delta r^2}+\frac{\delta\Phi_{i+1}-\delta\Phi_{i-1}}{2r_i\Delta r}-\frac{\ell^2}{r_i^2}\delta\Phi_i+\delta n_i=0, \tag{2.56}$$

along with the boundary conditions from Eq. (2.43),

$$\delta f^n_{0,j}=0, n\neq\ell; \tag{2.57}$$

$$\delta f^\ell_{0,j}=2f^\ell_{1,j}-f^\ell_{2,j}; \tag{2.58}$$

$$\delta f^n_{i,0}=0, n\neq 0; \tag{2.59}$$

$$\delta f^0_{i,0}=2f^\ell_{i,1}-f^\ell_{i,2}; \tag{2.60}$$

$$\delta f^n_{M_r,j}=\delta f^n_{i,M_v}=0, \tag{2.61}$$

where Eq. (2.58) and Eq. (2.60) determine the free gridpoints through linear interpolation for the special cases at the radial origin where $n = \ell$, or at the velocity origin where $n = 0$. Equations (2.54-2.56) are used for internal points $i = 1, ..., M_r - 1$, $j = 1, ..., M_v - 1$. The boundary condition on the discretized perturbed plasma potential $\delta\Phi_i$ is obtained by matching at $i = M_r$ to a solution to the Laplace equation that vanishes at the wall: $\delta\Phi_{M_r} = \delta\Phi_p(R_{max}) = C(R_{max}^{\ell} - (r_W^2/R_{max})^{\ell})$, where the constant C is obtained by matching the derivative, $\delta\Phi_p'(R_{max}) = C\ell(R_{max}^{\ell} + (r_W^2/R_{max})^{\ell})/R_{max}$. (The left-hand side of this equation is discretized in the usual way).

2.4.2 Convergence

It is of critical importance to ensure that numerical results are properly converged; in this problem, numerical accuracy is improved by increasing the number of grid points in r and v (namely M_r and M_v), as well as by increasing the number of gyroharmonics (namely M_ψ) kept in the calculation. Some exploration is required to discover optimal values for each of these three numbers, as the results obviously need to be converged in all three variables simultaneously in order to have reliable results. When checking for convergence, M_r and M_v were independently incremented by 30 at a time, and M_ψ was incremented by two at a time. In this chapter we report on three ℓ values, $\ell = 0, 2$, and 4. Convergence issues varied in each case.

We found that, in general, M_r and M_v must be increased as the damping ν decreases. This is because we are approximating the frequency response of our mathematical plasma with a sufficiently large, discrete matrix equation whose eigenfrequencies (magnetized van Kampen[13] modes) must do a decent job of covering the frequency range of interest. As ν decreases, the resonance width of these discrete (numerical) modes will eventually become smaller than their spacing, at which point the results become unphysical. In order to probe finer frequency resolution, the number of eigenvalues must be increased, which is conveniently done by increasing M_r and M_v. This type of numerical issue typically manifests itself as an admittance function with extremely sharp peaks that do not persist as resolution is increased, or move around unpredictably as the grid

is adjusted slightly. The problem is resolved either by increasing ν (if less frequency resolution is tolerable), or else by increasing M_r and M_v.

For the finite damping rates used in the chapter, convergence in the admittance results was obtained with a relatively small M_ψ value compared to the number of r and v grid points required: $M_\psi \sim 10$ was usually sufficient. For $\ell = 4$, the values of M_r and M_v required for convergence were $M_r \sim M_v \sim 100$. This resolution was sufficient to resolve the first four to eight admittance peaks, counting from the right (see FIG. 2.4); lower frequency peaks beyond this range correspond to potentials that oscillate more rapidly in r, requiring higher resolution. Somewhat higher resolution was also typically required at larger magnetic fields.

For $\ell = 2$, larger values of M_r and M_v had to be used to resolve just the first few admittance peaks, up to $M_r = M_v = 240$ and $M_\psi = 10$, the maximum values we could run on the available computers (limited by memory requirements in the numerical solution of the sparse matrix equation).

We should also mention that there were convergence issues in the distribution function near $r = 0$ for $\ell = 2$; namely, rapid unphysical variation in δf_n versus r and v, for r within a thermal cyclotron radius or so of $r = 0$. The origin of this rapid variation is unknown, but is clearly an artifact of the discretization of the linear operator. For $\ell = 4$ the wave potential is small enough near the origin so that this effect was suppressed, since δf is quite small near the origin. However, in all ℓ values studied this unphysical variation did not seem to affect the density or potential, which was well-converged and varied smoothly with radius near $r = 0$.

In test cases we studied, where the solution for $\delta f(r, \theta, v, \psi)$ near $r = 0$ is known analytically for a given perturbed potential (as a power series expansion in r), the discretized Vlasov equation was able to reproduce the analytic solution for the perturbed density and plasma potential response, even though the numerical distribution function was noisy near the origin. As a second check, for $l = 2$ we added 4th derivative "superdiffision" terms in r and v to the discretized Vlasov equation in order to suppress this grid-scale noise in the distribution function

near $r = 0$, and found that for a scaled superdiffusion coefficient of 10^{-6} the solution reproduced the admittance curves without superdiffusion, with far less noise in δf_n near $r = 0$. These checks gave us some confidence that the admittance, density, and potential results were sensible even when the underlying distribution function was noisy near the origin.

For $\ell = 0$, and for the "hot" $r_p = 4.76$ plasma discussed in relation to FIGs. 2 and 3, it was fairly easy to obtain converged admittance results for moderate values of the grid parameters and moderately strong damping rates, similar to those used in the $\ell = 4$ data. No noise issues near the radial origin were observed. For a colder plasma we studied, with $r_p = 43$, more radial grid points had to be used in order to resolve the plasma edge, as one would expect.

Finally, we encountered a puzzling anomaly that caused numerical instability for $v > v_{\text{thresh}}$, where v_{thresh} depended on the radial grid spacing Δr, M_ψ. When this instability was present, the perturbed distribution function in phase space would look normal for small velocities, but for $v > v_{\text{thresh}}$ would appear random. It was discovered that this instability could be avoided by increasing the quantity $\Delta r M_\psi / V_{\max}$, where $V_{\max}$ is the highest velocity on the grid, thereby forcing v_{thresh} higher than the highest velocity kept on the grid. Therefore, we only increase M_r (i.e. decrease Δr) as much as is needed to resolve the radial variation in the mode, but no more, unless we are willing to increase M_ψ.

2.4.3 Results

In FIG. 2.4 we display a characteristic solution taken from the converged results of the numerical Vlasov code (i.e. the solutions of (2.54-2.56)) for the imaginary part of the admittance function versus scaled frequency λ (see Eq. (2.27)). The plasma is assumed to have the same parameters as in FIGs. 2.2 and 2.3, except that in those figures $\nu = 0$, whereas here we take $\nu = 0.00283$. (As previously mentioned, a finite value of ν is necessary to obtain converged results in the Vlasov solution.) One can see that the admittance has separated into a series of peaks whose magnitudes follow the corresponding cold fluid theory, and whose spacing varies,

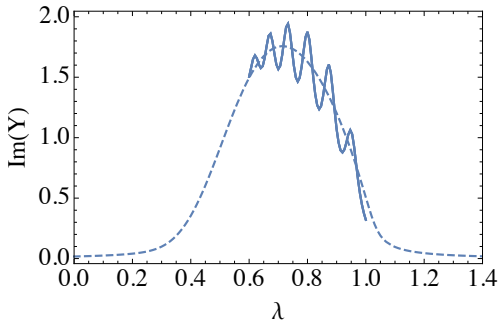

Figure 2.4: Imaginary part of the admittance versus scaled frequency λ for $\ell = 2$ and $\Omega = 5$ in a plasma with $R_p = 4.76$, $r_W = 10$, and collision frequency $\nu = 0.00283$. (i.e. the same parameters as in FIGs. 2.2 and 2.3, but with finite ν rather than $\nu = 0$). Solid line: Vlasov solution. Dashed line: cold fluid theory.

becoming more closely-spaced as frequency λ decreases. Each peak corresponds to a Bernstein mode.

Incidentally, the cold fluid theory admittance plotted in FIG. 2.3 differs slightly from the theory presented in Sec. 2.3 in that we took $\nu \neq 0$ for FIG. 2.4, just as in the Vlasov theory. For finite ν, the radial dependence of cold fluid theory potential differs only slightly from that shown in FIG. 2.2; the sharp singularity at the upper hybrid cutoff radius r_{UH0} becomes slightly rounded.

In FIG. 2.5 the radial dependence of the Vlasov-theory perturbed potential is plotted for λ values at three of the peaks. Inside the cutoff the potential oscillates with radius. These oscillations are the Bernstein normal modes. For radii larger than the upper hybrid cutoff r_{UH0} (shown by the arrow in each figure) the potential decays in a fashion similar to the cold fluid theory shown in FIG. 2.2: here the Bernstein modes are evanescent. As scaled frequency λ decreases, the wavelength of the modes decreases as well.

2.5 New WKB Treatment

In order to understand the results of the Vlasov code we turn to WKB theory descriptions of the electrostatic Bernstein modes. We first review the modes in a uniform plasma, and then discuss a new WKB theory for the modes in a plasma column with nonuniform density versus

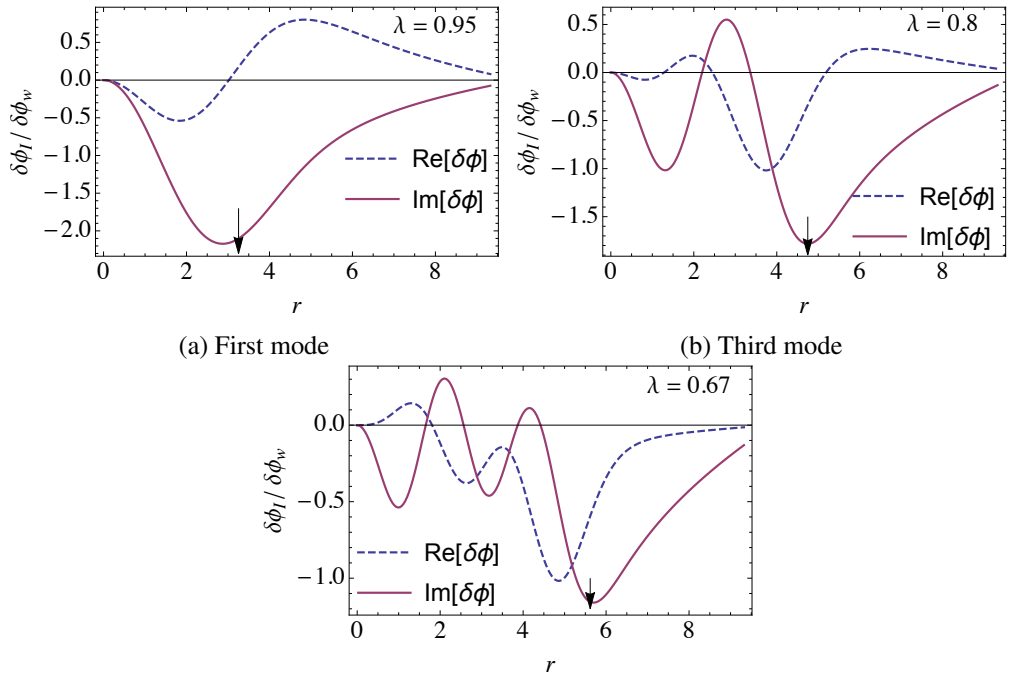

(a) First mode

(b) Third mode

(c) Fifth mode

Figure 2.5: Radial dependence of the Vlasov solution for the real and imaginary part of the plasma wave potential $\delta\Phi_p$, for λ values at three peaks in the previous admittance figure: the first, third and fifth peaks counting from right to left. This potential does not include the driving potential $\delta\Phi_{\rm H}$, and therefore vanishes at the wall radius $r_W = 10$.

radius. This WKB theory further develops a previous theory,[6] providing an improved description of the mode frequencies.

2.5.1 Dispersion Relation

In a uniform plasma, that rotates uniformly with frequency ω_f, the dispersion relation for electrostatic waves traveling perpendicular to the magnetic field is given by[3]

$$0 = 1 - \omega_p^2 \sum_{n=-\infty}^{\infty} \frac{n^2 e^{-\Lambda} I_n(\Lambda)}{\Lambda(\hat{\omega}^2 - n^2\Omega_v^2)}, \text{ with } \Lambda \equiv k^2 r_c^2. \tag{2.62}$$

Here k is the wavenumber, $\hat{\omega}$ is the Doppler-shifted driving frequency (including Krook collisions) seen in the frame rotating with the plasma, defined by $\hat{\omega} = \omega - \ell\omega_f + i\nu$, r_c is the thermal cyclotron radius given by $r_c = 1/\Omega_v$ in scaled units, and $I_n(x)$ is a modified Bessel function. To study these modes near the cyclotron frequency, we ignore all but the dominant terms in which the denominator is small with $n = \pm 1$. With this simplification, the dispersion function becomes

$$\mathcal{D}(\omega, k) = 1 - 2\omega_p^2 \frac{e^{-\Lambda} I_1(\Lambda)}{\Lambda(\hat{\omega}^2 - \Omega_v^2)}. \tag{2.63}$$

This expression can be related to the fluid theory dispersion relation involving the function $X(\omega)$ as follows (noting that X simplifies for a uniform system):

$$\mathcal{D}(\omega, k) = 1 - 2X(\omega) \frac{e^{-\Lambda} I_1(\Lambda)}{\Lambda}. \tag{2.64}$$

Note that the function $2e^{-\Lambda} I_1(\Lambda)/\Lambda$ is monotonically decreasing in Λ with a maximum of unity at $\Lambda = 0$. Thus, a solution to $\mathcal{D} = 0$ requires that $X(\omega) > 1$, or equivalently $\varepsilon_{11} < 0$. Thus, propagating Bernstein waves can exist in the plasma only for frequencies for which $\varepsilon_{11} < 0$. However, if $\varepsilon_{11} > 0$ there are still solutions to $\mathcal{D} = 0$, but these solutions require imaginary values of k (i.e. negative Λ). These are evanescent (non-propagating) solutions.

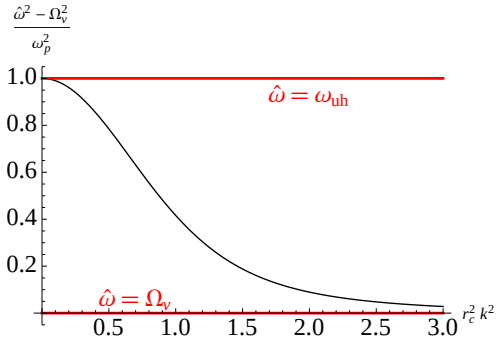

Figure 2.6: Dispersion relation plotted as $\frac{\hat{\omega}^2-{\Omega_v}^2}{{\omega_p}^2}$ versus $r_c^2k^2$. At low kr_c, $\hat{\omega}$ limits to the upper-hybrid frequency, while for high kr_c, it limits to the vortex frequency.

The frequency versus (real) wavenumber following from $\mathcal{D}=0$ is plotted in FIG. 2.6. The dispersion curve demonstrates that zero wavenumber corresponds to waves at the upper-hybrid frequency $\hat{\omega}=\sqrt{\Omega_v^2+\omega_p^2}$, whereas for larger wavenumber, cyclotron orbits tend to "average out" the effect of the perturbed electric field, lowering the mode frequency toward the bare cyclotron frequency in the rotating frame, $\hat{\omega}=\Omega_v$.

In geometrical optics, the $k\to 0$ limit corresponds to a classical turning point for a ray trajectory. Figure 2.6 shows that this limit occurs at the upper hybrid frequency, where $\varepsilon_{11}=0$. Therefore, in an inhomogeneous plasma the locations where the mode frequency matches the upper hybrid frequency are classical turning points. These locations are marked by the arrows in FIG. 2.5, and explain qualitatively why the Bernstein waves change behavior from propagating modes with $\varepsilon_{11}<0$ to evanescent decay with $\varepsilon_{11}>0$. The reflection of the wave at the upper hybrid radius is what sets up a radial normal mode of oscillation within the plasma column. In the next section, a more detailed WKB analysis verifies this picture, and also shows how the Bernstein waves mode-couple to surface cyclotron waves at the upper hybrid radius.

Before we do so, however, it is useful to briefly consider the general form of the Bernstein differential equation in a uniform, isotropic rotating plasma by appealing to symmetry arguments. (For example the dispersion relation in Eq. (2.62) for a uniform plasma could be derived from a differential equation of this form). This will allow us to obtain expressions for the spatial

dependence of the Bernstein wave potential in such a system.

In the plasma center where the system is spatially uniform and rotationally invariant, the differential operator $\mathcal{D}$ must respect these symmetries. Consider expanding $\mathcal{D}$ in a series of increasing differential order, with tensor $T^{(n)}$ as the expansion coefficients:

$$\mathcal{D} = \sum_n \underbrace{T^{(n)}_{\ldots} \, \partial_. \partial_. \cdots \partial_.}_{n \text{ index contractions}} \, . \tag{2.65}$$

If $\mathcal{D}$ is to be isotropic, then each of the $T^{(n)}$ must be invariant under rotations. Necessary and sufficient conditions for tensor isotropy have been determined to be linear combinations of products of Kronecker Delta tensors and possibly a single Levi Cevita tensor ε.[12, 21] Therefore, $\mathcal{D}$ can be expressed schematically as

$$\mathcal{D} = \sum_n \underbrace{\{\delta_{..}\delta_{..} \cdots \delta_{..}\varepsilon_{..}\}\partial_.\partial_. \cdots \partial_.}_{n \text{ index contractions}}, \tag{2.66}$$

where the $\{\}$ denote a linear combination of expressions of the form of its contents. Notice that any case where a given δ involves a self-contraction can be ignored, since this only introduces a factor of the dimension, here 2. Similarly, any self-contraction within ε vanishes due to antisymmetry. Further, any contractions pairing a δ with either another δ or with ε can also be ignored, since either such contraction amounts to renaming a dummy index. Consequently, all indices must contract with a derivative. This immediately implies that every term in $\mathcal{D}$ has an even number of derivatives, that is, twice the number of symbols (δ or ε) appearing in that term (only terms with even n in the sum contribute). Using commutativity of the Kronecker Delta, Levi Cevita and partial derivatives, this allows us to write each term in the standard form, this time giving the indices unique labels:

$$\mathcal{D} = \sum_{\text{even } n} \delta_{i_1 i_2}\delta_{i_3 i_4} \cdots \left(A^{(n)}\delta_{i_{n-1}\, i_n} + B^{(n)}\varepsilon_{i_{n-1}\, i_n}\right) \partial_{i_1}\partial_{i_2}\partial_{i_3}\partial_{i_4} \cdots \partial_{i_{n-1}}\partial_{i_n}, \tag{2.67}$$

where $A^{(n)}$ and $B^{(n)}$ are arbitrary coefficients. Finally, we can write this expression in vector form:

$$\mathcal{D} = \sum_{i=0}^{\infty} \left(\nabla^2\right)^i \nabla \cdot E^{(i)} \nabla, \tag{2.68}$$

where

$$E^{(i)} = \begin{pmatrix} A^{(i)} & B^{(i)} \\ -B^{(i)} & A^{(i)} \end{pmatrix}.$$

To match this general form of $\mathcal{D}$ to the fluid theory of section 2.3, we impose the additional constraint that $E^{(0)} = \varepsilon$ (recall ε is the fluid theory dielectric) so that the theories match to lowest differential order. Since Bessel Functions of the first and second kind are always eigenfunctions of ∇^2 and $\nabla \cdot E^{(i)} \nabla$, we can see that $CJ_\ell(kr) + DY_\ell(kr)$ satisfies this equation, and continuity at $r = 0$ enforces $D = 0$. Further, since $J_\ell(kr)$ is locally asymptotic to a plane wave with wavenumber k far from the origin, k must satisfy $\mathcal{D}(\omega, k) = 0$. While this solution is only valid for a uniform plasma, it also provides an approximate solution to a physical plasma for $r \ll r_p$, where $n(r)$ is very nearly constant. This expression allows us to connect the WKB expression (valid away from the origin) to this Bessel Function solution near the center of the plasma.

2.5.2 WKB regions

To calculate Bernstein Modes in a non-uniform cylindrical plasma, we use a WKB approach. We assume a single-species plasma for which there is a range of frequencies near the cyclotron frequency with a single solution to Eq. (2.18), i.e. a single upper hybrid radius. In other words, ε_{11} increases monotonically with radius from a negative value inside the plasma, through zero at the upper hybrid radius, and increasing toward unity outside the plasma. In this case there will be a propagating Bernstein wave for radii less than r_{UH0}, becoming evanescent for $r > r_{\mathrm{UH0}}$, as in the numerical results shown in FIG. 2.5.

In the WKB analysis of these waves we find that the perturbed potential can be expressed

as a combination of a fluid theory solution and a radially-oscillating Bernstein wave:

$$\delta\Phi = \overline{\delta\Phi} + \widetilde{\delta\Phi}, \tag{2.69}$$

where $\widetilde{\delta\Phi}$ is the radially-oscillating Bernstein wave emerging from finite temperature effects and $\overline{\delta\Phi}$ is the non-oscillatory fluid theory. For radii far from the upper hybrid cutoff, the fluid theory solution is slowly-varying in r and thermal corrections are neglible. We can therefore use cold-fluid theory to describe this solution, numerically integrating Eq. (2.11) to obtain $\overline{\delta\Phi}$ away from the upper hybrid cutoff. For the Bernstein solution, on the other hand, we employ the WKB eikonal approach, matching inner and outer forms for the eikonals across the upper hybrid radius.

A schematic of the full solution is shown in FIG. 2.7. We break the solution into 3 overlapping regions, treated with different methods, and match the solution across the regions. In the central region close to $r = 0$, the plasma is nearly uniform and we use the Bessel function solution for the Bernstein wave, derived in section 2.5.1. For intermediate radii between $r \gtrapprox 0$ and the upper hybrid cutoff at $r \lessapprox r_{\mathrm{UH}}$, WKB theory is used. In this region the Bernstein solution is oscillatory. As we pass through the upper hybrid cutoff, the Bernstein solution transitions from oscillatory to evanescent. Within this transition region near the cutoff, we solve an approximate form of the Bernstein differential operator to match solutions across the cutoff. Here we find that the Bernstein solution mode-couples to the fluid solution, mixing the two in this transition region. A jump condition on the fluid solution across the transition region is obtained, describing the effect of this mode coupling on the fluid solution. A similar jump condition was obtained in Ref. [6], the difference here being that the fluid solution is treated exactly (via numerical solution) rather than using an approximate analytic form valid only for large magnetic field as in Ref. [6].

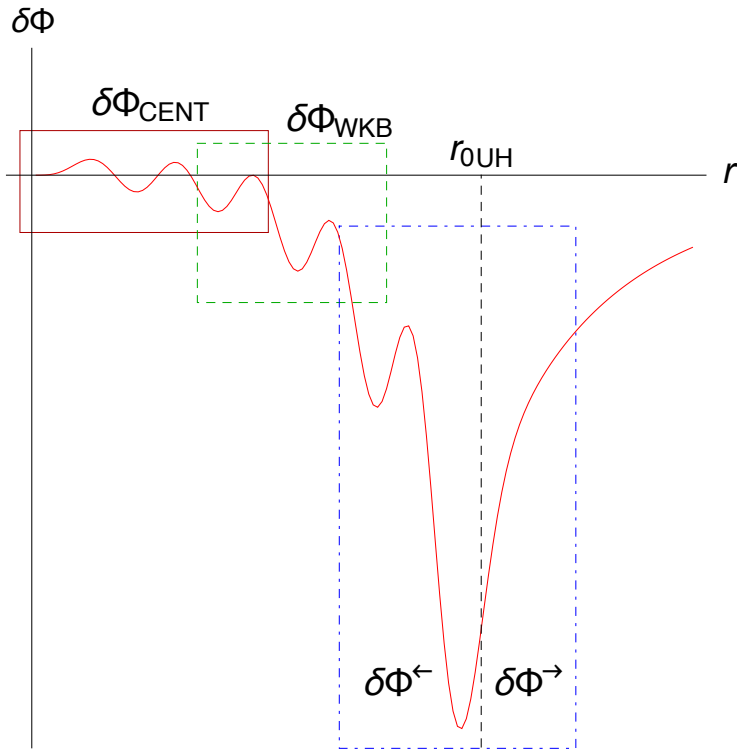

Figure 2.7: A plot of a typical $\delta\Phi$ showing the three main regions of the plasma: $\delta\Phi_{\text{CENT}}$, $\delta\Phi_{\text{WKB}}$, $\delta\Phi^{\leftarrow}$ and $\delta\Phi^{\rightarrow}$ referred to in the WKB theory. The region far outside the plasma is not given a name because it trivially satisfies Laplace's equation and has no Bernstein waves.

2.5.3 Central Solution

We begin with the solution valid near the center of the plasma, where the density $n(r)$ is nearly constant for a thermal equilibrium plasma. As we derived previously, the oscillatory Bernstein solution for a uniform plasma takes the form of a Bessel function:

$$\widetilde{\delta\Phi}(r) = A_{\text{CENT}}\, J_\ell(k_0 r), \tag{2.70}$$

where, for given ω, k_0 is the solution for k of the Bernstein dispersion relation, Eq. (2.64), at the center of the plasma. In order for this solution to match onto the Eikonal solution described in the next section, we use the large argument expansion for $J_\ell(z)$, giving

$$\widetilde{\delta\Phi}_{\text{CENT}} \sim A_{\text{CENT}} \sqrt{\frac{2}{\pi k_0 r}} \cos\left(k_0 r - \frac{\ell\pi}{2} - \frac{\pi}{4}\right). \tag{2.71}$$

2.5.4 Eikonal Form

Since a thermal equilibrium plasma does not have a uniform density profile $n(r)$, the Bessel function solution introduced in the previous section is not satisfactory to describe the entire interior of the plasma. While the asymptotic central result in Eq. (2.71) is a constant wavenumber solution, we now require k to change as a function of r as the dispersion relation changes due to the nonuniform plasma density. This motivates a WKB approach accurate in the limit where $k \gg |k'(r)/k|$. To lowest order in WKB theory, the form of $k(r)$ is found for given ω by solving Eq. (2.64), with X and Ω_v the functions of r appropriate for given $n(r)$. This approximation is only valid away from the cutoff where $k \to 0$. This solution is used in the Eikonal in the region that is both far to the left of the cutoff, and also far from $r = 0$:

$$\widetilde{\delta\Phi}_{\text{WKB}} = A(r) \cos\left(\int_{r_{\text{UH}}}^{r} k(\bar{r})\, d\bar{r} + \chi\right), \tag{2.72}$$

where $A(r)$ is a slowly-varying amplitude, the local wavenumber $k(r)$ is found from the Bernstein dispersion relation Eq. (2.64) (for given frequency ω), and χ is a phase factor to be determined momentarily. The radial form of the amplitude factor is not needed in what follows, but was discussed in Ref. [6].

Matching the central Eq. (2.71) and WKB Eq. (2.72) solutions gives the connection formula that determines the phase factor χ:

$$\chi = \int_0^{r_{\rm UH}} k\, dr - \frac{\ell\pi}{2} - \frac{\pi}{4}. \tag{2.73}$$

2.5.5 Upper-Hybrid Cutoff

Near the cutoff, where $\omega_{\rm UH} - \hat{\omega} \to 0$, the wavenumber of the WKB solutions also approaches zero (see FIG. 2.6), so we can consider adding finite cyclotron radius effects perturbatively into Eq. (2.6):

$$0 = \nabla \cdot \varepsilon \nabla \delta\Phi - {r_c}^2 \nabla^2 \left((1 - \varepsilon_{11}) \nabla^2 \delta\Phi \right). \tag{2.74}$$

This approximate expression can be checked by replacing ∇ with $i\mathbf{k}$ and comparing the result with Eq. (2.64), expanding this dispersion relation to fourth order in k. However, it should be noted that this check only verifies the factor $1 - \varepsilon_{11}$, but does not justify its algebraic location between the two Laplacians. Dubin[6] shows, by using integration over unperturbed orbits in the large magnetic field limit, why this factor appears in the location it does here. Equation (2.74) generalizes the warm fluid theory mode equation of Ref. [6] by not taking the large magnetic field limit. This generalizion is important in helping to explain a discrepancy between the numerical Vlasov solution and the large magnetic field WKB analysis of Ref. [6].

We should emphasize that while Eq. (2.74) is consistent with the uniform plasma dispersion relation in the small wavenumber limit, many other forms of the equations could also be consistent. In fact, Dubin showed that many other terms appear at $O(r_c^2)$ in the warm fluid

theory equation in the large magnetic field limit; but he also showed that the other terms were subdominant in the WKB approximation. We have no way of knowing what the form of such terms are when the large magnetic field limit is not taken, so we cannot prove that such terms are also subdominant to those kept in Eq. (2.74). This equation should therefore be regarded skeptically, as an educated guess.

We use Eq. (2.74) only near the upper hybrid radius, and so we will now approximate its form in this region. Writing out Eq. (2.74) in cylindrical coordinates, and multiplying by ${r_c}^2$ to make each term dimensionless, we examine the resulting terms and drop those terms containing one or more factor of $\frac{r_c}{r}$, since the upper-hybrid radius is assumed to be many cyclotron radii from the origin. The result leaves the following:

$$-r_c^4(1-\varepsilon_{11})\delta\Phi^{(4)} + 2r_c^4\varepsilon'_{11}\delta\Phi^{(3)} + r_c^2(\varepsilon_{11}+r_c^2\varepsilon''_{11})\delta\Phi'' + r_c^2\varepsilon'_{11}\delta\Phi' = 0.$$

By repeated use of the product rule, this can be partially integrated to obtain

$${r_c}^2\frac{\partial}{\partial x}\left[(1-\varepsilon_{11})\delta\Phi''\right] - \varepsilon_{11}\delta\Phi' = C, \tag{2.75}$$

with C a constant of integration (prime represents derivative with respect to x). To connect with the Eikonal Eq. (2.72), which assumes $\varepsilon'_{11}/k \ll 1$, we take the dominant balance of terms, neglecting the term proportional to ε'_{11} in the first term of Eq. (2.75). Further, we use a linear expansion $\varepsilon_{11} \sim (r-r_{\mathrm{UH}})/\mathcal{L}$ near the upper-hybrid cutoff radius, defining the plasma scale length

$$\mathcal{L} \equiv 1/\frac{\partial\varepsilon_{11}}{\partial r}, \tag{2.76}$$

and write

$${r_c}^2(1-\varepsilon_{11})\delta\Phi''' - \frac{r-r_{\mathrm{UH}}}{\mathcal{L}}\delta\Phi' = C. \tag{2.77}$$

For r near $r_{\rm UH}$, the appearance of $1-\varepsilon_{11}$ in the first term can be replaced with 1, since ε_{11} is small compared to 1, and is assumed to change gradually anyways. After making this change, the expression can be manipulated into an inhomogeneous Airy equation by the substitution $r = r_{\rm UH} + (\mathcal{L}\, {r_c}^2)^{1/3}\, s$:

$$\delta\Phi''' - s\,\delta\Phi' = C'. \tag{2.78}$$

The solution to the corresponding homogeneous equation for $\delta\Phi'$ is solved by Airy Functions. We can solve the inhomogeneous problem by using variation of parameters to obtain

$$\delta\Phi'(s) = D_1 \mathrm{Ai}(s) + D_2 \mathrm{Bi}(s) + D_3 \mathrm{Ci}(s), \tag{2.79}$$

where

$$\mathrm{Ci}(s) \equiv \pi \mathrm{Ai}(s) \int_{-\infty}^{s} \mathrm{Bi}(\bar{s})\, d\bar{s} + \pi \mathrm{Bi}(s) \int_{s}^{\infty} \mathrm{Ai}(\bar{s})\, d\bar{s}. \tag{2.80}$$

The coefficients D_i in Eq. (2.79) are determined by matching asymptotic forms for the Airy functions to the corresponding asymptotic forms for the potential to the left and right of the cutoff. The asymptotic expansions of the Airy Functions are as follows:

$$\mathrm{Ai}(s) \sim \begin{cases} \frac{\sin(\frac{2}{3}(-s)^{3/2}+\frac{\pi}{4})}{\sqrt{\pi}(-s)^{1/4}}, & s \to -\infty \\ \frac{\exp(-\frac{2}{3}(s)^{3/2})}{2\sqrt{\pi}(s)^{1/4}}, & s \to \infty \end{cases} \qquad \mathrm{Bi}(s) \sim \begin{cases} \frac{\cos(\frac{2}{3}(-s)^{3/2}+\frac{\pi}{4})}{\sqrt{\pi}(-s)^{1/4}}, & s \to -\infty \\ \frac{\exp(\frac{2}{3}(s)^{3/2})}{\sqrt{\pi}(s)^{1/4}}, & s \to \infty \end{cases}$$

$$\mathrm{Ci}(s) \sim \begin{cases} \frac{1}{s} + \frac{\sqrt{\pi}\cos(\frac{2}{3}(-s)^{3/2}+\frac{\pi}{4})}{(-s)^{1/4}}, & s \to -\infty \\ \frac{1}{s}, & s \to \infty \end{cases} \tag{2.81}$$

From these approximations, we can obtain the solution for $\delta\Phi$ by integrating the left-side asymptotic expansion of Eq. (2.79) once. While the integral is not an elementary function, it can nonetheless be carried out in the asymptotic limit. We can also immediately drop the

term containing $\mathrm{Bi}(s)$, since the exponential growth outside the plasma is unphysical. Then the asymptotic result in the interior of the plasma is

$$\delta\Phi^{\leftarrow}(s) = D_1\left(\frac{-\sin(\frac{2}{3}(-s)^{3/2}-\frac{\pi}{4})}{\sqrt{\pi}(-s)^{3/4}}\right) + D_3\left(\frac{-\sqrt{\pi}\cos(\frac{2}{3}(-s)^{3/2}-\frac{\pi}{4})}{(-s)^{3/4}} + \log(-s)\right) + D_4, \tag{2.82}$$

where the notation $\delta\Phi^{\leftarrow}$ refers to a solution to the left of the upper hybrid radius, as in FIG. 2.6. We can read off the fluid and Bernstein solutions by separating oscillatory dependence from the logarithmic divergence. By comparing this expression to Eq. (2.25), one can see that the fluid component on the left side of the upper hybrid radius is

$$\overline{\delta\Phi}^{\leftarrow}(s) = D_3\log(-s) + D_4. \tag{2.83}$$

To the right of the upper hybrid radius, the asymptotic form requires that the Airy solution in Eq. (2.79) be integrated with the same constant of integration as was obtained in Eq. (2.82). To ensure this is the case, use is made of the identities $\int_{-\infty}^{\infty}\mathrm{Ai}(s)\,ds = 1$ and $\lim_{N\to\infty}\int_{-N}^{N}\mathrm{Ci}(s)\,ds = 0$. Once the evanescent Bernstein solution dies away, we are left with the outer fluid solution which now takes the form

$$\overline{\delta\Phi}^{\rightarrow}(s) = D_1 + D_4 + D_3\log(s). \tag{2.84}$$

Note that in Eq. (2.83), and Eq. (2.84), s can be replaced by $r - r_{\mathrm{UH}}$ since the multiplicative factor relating $r - r_{\mathrm{UH}}$ and s implies that $\log(\pm s)$ equals $\log(\pm(r - r_{\mathrm{UH}}))$ plus an additive constant that can be absorbed into D_4:

$$\overline{\delta\Phi}^{\leftarrow}(r) = D_3\log(r_{\mathrm{UH}} - r) + D_4. \tag{2.85}$$

$$\overline{\delta\Phi}^{\rightarrow}(r) = D_1 + D_4 + D_3\log(r - r_{\mathrm{UH}}). \tag{2.86}$$

These results agree in form with with the fluid theory near r_{UH} from Eq. (2.25) and Eq. (2.28). However the additive constant D_1 appears as an amplitude in the oscillatory Bernstein solution.

The Bernstein wave couples to the fluid solution, modifying it at the radius $r_{\rm UH}$, and introducing a jump in the form of the fluid solution across the transition region, due to the Bernstein wave coupling.

2.5.6 Matching solutions across $r_{\rm UH}$

Evaluating Eq. (2.85) and Eq. (2.86) at $r_{\rm UH_0}$, and recalling from Eq. (2.24) the definition $i\Delta r \equiv r_{\rm UH} - r_{\rm UH_0}$, we have

$$\begin{aligned}
\overline{\delta\Phi}^{\leftarrow}(r_{\rm UH_0}) &= D_3\log(i\Delta r) + D_4, & \overline{\delta\Phi}^{\leftarrow\prime}(r_{\rm UH_0}) &= -D_3/i\Delta r \\
\overline{\delta\Phi}^{\rightarrow}(r_{\rm UH_0}) &= D_3\log(-i\Delta r) + D_1 + D_4, & \overline{\delta\Phi}^{\rightarrow\prime}(r_{\rm UH_0}) &= -D_3/i\Delta r,
\end{aligned} \tag{2.87}$$

Note that $\Delta r < 0$ according to Eq. (2.23) because, for the case of interest here, ε_{11} is a monotonically increasing function of radius (see the discussion following Eq. (2.64)).

We can match the oscillatory part of $\delta\Phi^{\leftarrow}$ to $\widetilde{\delta\Phi}_{\rm WKB}$ by comparing Eq. (2.72) to Eq. (2.82). To do this, keep in mind that k is linked with the dielectric through Eq. (2.64), which as we approach $r = r_{\rm UH}$ (where ε_{11} is evaluated close enough to the upper-hybrid radius that it varies linearly in r), becomes

$$k = \sqrt{\frac{r_{\rm UH} - r}{r_{\rm c}^2\mathcal{L}}}. \tag{2.88}$$

Now use this to determine the integral in Eq. (2.72):

$$\int_{r_{\rm UH}}^{r} k(\bar{r})\, d\bar{r} = \frac{-2}{3r_{\rm C}\sqrt{\mathcal{L}}}(r_{\rm UH} - r)^{3/2} = -\frac{2}{3}(-s)^{3/2}. \tag{2.89}$$

This result can be used to replace the argument of the cosine and sine functions in Eq. (2.82) with integrals over $k(r)$, allowing us to match this result to the WKB eikonal form of Eq. (2.72). Using

Eq. (2.73), the matching requires that

$$\tan\left(\chi - \frac{\pi}{4}\right) = \frac{D_1}{\pi D_3}. \tag{2.90}$$

We can then use this expression to solve for D_1 and apply this in Eq. (2.87) to obtain jump conditions matching the inner and outer fluid solutions across transition region.

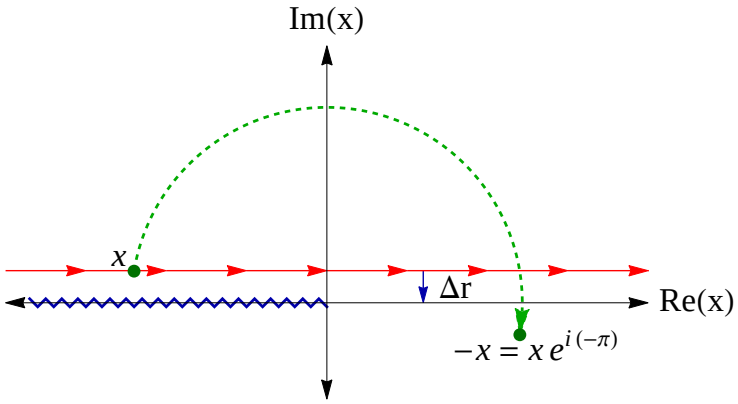

Figure 2.8: Complex plot of $x = r - r_{\rm UH}$. The real r axis is the red line (noting that Δr is negative). The dashed green contour relates x to $-x$ while avoiding the branch cut (blue zig-zag).

As shown in FIG. 2.8, we can express $\log(-x) = \log(x) - i\pi$, for all x on the left half of the red line when Δr is negative. Then we can use Eq. (2.87) to relate $\delta\Phi^{\leftarrow}$ and $\delta\Phi^{\rightarrow}$ via the jump conditions:

$$\begin{aligned}
&\overline{\delta\Phi}^{\rightarrow\prime}(r_{\rm UH_0}) = \overline{\delta\Phi}^{\leftarrow\prime}(r_{\rm UH_0}) \\
&\overline{\delta\Phi}^{\rightarrow}(r_{\rm UH_0}) = \overline{\delta\Phi}^{\leftarrow}(r_{\rm UH_0}) - i\Delta r\,\pi\,\overline{\delta\Phi}^{\leftarrow\prime}(r_{\rm UH_0})\left(\tan\left(\chi - \frac{\pi}{4}\right) + i\right).
\end{aligned} \tag{2.91}$$

For clarity, it should be noted that the choice of $r_{\rm UH0}$ in Eqs. (2.91) is merely a convenience. Eqs. (2.91) could also be evaluated at any other point r within the transition region near $r_{\rm UH}$, with the substitution $i\Delta r = r_{\rm UH} - r$. This relies on the fact that the functional forms of the fluid solutions, Eqs. (2.85) and (2.86), are both valid solutions of the fluid theory ODE Eq. (2.25) in the transition region, each matching on to the numerical fluid solutions on their respective side of

the upper hybrid radius.

In a similar vein, it is informative to consider what is going on with the jump conditions Eq. (2.91) as $\nu \to 0$. It appears that the last term in the second condition vanishes as $\nu \to 0$, because Δr is proportional to ν (see Eq. (2.23)). However, Eqs. (2.87) imply that $\Delta r \overline{\delta\Phi}^{\leftarrow\prime}(r_{\mathrm{UH0}})$ is independent of Δr as $\Delta r \to 0$, so the last term in the jump condition remains finite as $\nu \to 0$.

These jump conditions provide results for the potential that are correct to $O((\Delta r/\mathcal{L})^0)$, neglecting corrections that are proportional to higher powers of $\Delta r/\mathcal{L}$. This is because the conditions rely on low-order asymptotic forms for the fluid potential in the transition region, Eqs. (2.85) and (2.86), which are correct only up to and including order $(r - r_{\mathrm{UH}})^0$. As a consequence, the conditions are only useful provided that $\Delta r/\mathcal{L} \ll 1$.

We can now integrate the fluid theory Eq. (2.6) numerically from $r = 0$ to r_w, using the jump conditions Eq. (2.91) to continue integration across the upper-hybrid cutoff. Here χ is evaluated using Eq. (2.73). This result gives the fluid theory solution everywhere. Recalling how the perturbed potential can be expressed as a sum of a fluid theory solution and a Bernstein wave solution via Eq. (2.69), and also noting that the Bernstein wave solution is evanescent outside the upper hybrid radius, we can calculate the admittance $Y(\omega)$ by using Eq. (2.35), replacing $\delta\Phi \to \overline{\delta\Phi}$. That is,

$$Y = \left. \frac{r_W \frac{\partial \overline{\delta\Phi}}{\partial r}}{\overline{\delta\Phi}} \right|_{r=r_W} . \tag{2.92}$$

The value of χ in Eq. (2.91) is obtained using Eq. (2.73) by integrating over $k(r)$ numerically from $r = 0$ up to $r = r_{0\mathrm{UH}}$, assuming that ν is small so that the difference Δr between r_{UH} and $r_{0\mathrm{UH}}$ can be neglected. For given ω the function $k(r)$ is obtained by solving the dispersion relation, Eq. (2.64).

As another check of the jump conditions, in the cold plasma limit (i.e. as $r_c \to 0$) the argument of the tan function in Eq. (2.91) picks up a large negative imaginary part due to the influence of collisions on $k(r)$, and so $\tan(\chi - \pi/4) + i \to 0$. Then there is no-longer a jump in

the fluid theory solution across the upper hybrid radius; in other words, the fluid theory ODE can be integrated without change from the plasma interior to the wall, resulting in the same cold fluid admittance function $Y(\omega)$ as obtained previously.

As a final check, we compare the Bernstein mode frequencies obtained from Eqs. (2.91) in the large magnetic field limit to a result in Ref. [6]. In the large-field limit, the fluid potential for $r < r_{\mathrm{UH0}}$ is given by Eq. (2.12) with B chosen so that the solution is finite at $r = 0$:

$$\overline{\delta\Phi}^{\leftarrow} = Ar^{-\ell}\int_0^r dr' \frac{r'^{(2\ell-1)}}{D(r')}, \tag{2.93}$$

where A is an undetermined coefficient. Similarly, using Eq. (2.12) to match the outer potential to the potential at the wall yields

$$\overline{\delta\Phi}^{\rightarrow} = \delta\Phi_W(r_W/r)^{\ell} + Cr^{-\ell}\int_r^{r_W} dr' \frac{r'^{(2\ell-1)}}{D(r')}, \tag{2.94}$$

where C is a different undetermined coefficient. Applying these forms to the jump conditions allows us to determine the coefficients A and C. The solutions are simplified by keeping only terms of order Δr^0 and noting that $D(r_{\mathrm{UH0}}) \approx -i\Delta r/\mathcal{L}$. We find that the first condition implies that $A = -C + O(\Delta r)$, and using this in the second condition yields

$$C\left(\int_0^{r_W} dr' \frac{r'^{(2\ell-1)}}{D(r')} + \pi\mathcal{L}r_{\mathrm{UH0}}^{2\ell-1}(\tan[\chi - \pi/4] + i)\right) = -\delta\Phi_W r_W^{\ell}. \tag{2.95}$$

Bernstein modes occur at frequencies for which the coefficient of C vanishes. This condition can be rewritten as

$$\chi = \frac{\pi}{4} + n\pi + \arctan\frac{r_{\mathrm{UH0}}^{1-2\ell}}{\pi\mathcal{L}}\left(-\int_0^{r_W} dr' \frac{r'^{(2\ell-1)}}{D(r')} - i\pi\mathcal{L}r_{\mathrm{UH0}}^{2\ell-1}\right), \tag{2.96}$$

where n is any integer and the main branch of the arctan function is taken. Using Eq. (2.73) and

noting that, for small $\Delta r/\mathcal{L}$, the Plemelj formula can be applied to integrate past the pole in the integral over $1/D(r')$, we obtain

$$\int_0^{r_{\rm UH0}} k dr = \frac{(\ell+1)\pi}{2} + n\pi - \arctan\left(\frac{r_{\rm UH0}^{1-2\ell}}{\pi\mathcal{L}}\mathcal{P}\int_0^{r_W} d\bar{r}\frac{\bar{r}^{(2\ell-1)}}{D(\bar{r})}\right), \tag{2.97}$$

where $\mathcal{P}$ indicates that the principal part of the integral is taken. This expression for the Bernstein mode dispersion relation in the large field limit agrees with Eq. (152) in Ref. [6] (with a redefinition of the integer n to $n-1$).

2.6 Vlasov vs. New WKB and Old WKB Theories

We now present the results of the new WKB theory for various magnetic fields, values of ℓ, and density profiles, comparing the theory to numerical solutions of the Vlasov equation and to the prior large magnetic field WKB theory.[6]

We first study a $\ell = 4$ perturbation in a plasma with $r_p = 4.76, r_W = 10, \Omega = 5$, and $\nu = 1/300$. These parameters are similar to a case studied by Dubin. In FIG. 2.9 we compare the new WKB solution for the admittance to the Vlasov numerical method and to the prior WKB theory[6].

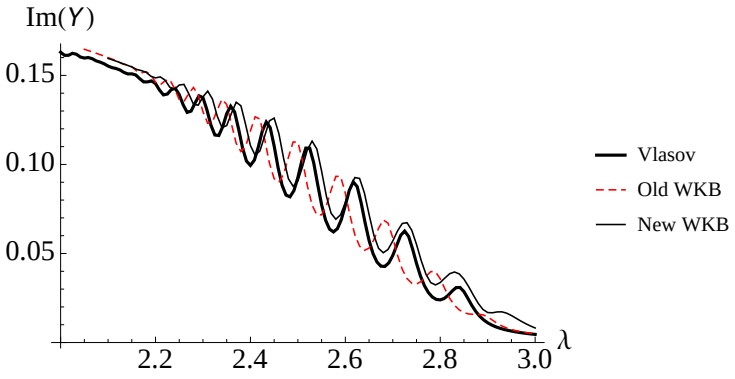

Figure 2.9: Comparison of Vlasov and WKB approximations, for $\Omega = 5$, $r_p = 4.76$, $r_W = 10$, $\ell = 4$, and $\nu = 1/300$. Vlasov code uses M_ψ=8, $M_r = M_v = 120$.

The new WKB theory produces a mode frequency prediction that is closer to the Vlasov solution than the old WKB theory. Again, the shift in the frequency between the old and new theories arises from the large magnetic field approximation for the cold-fluid dielectric that was used in the old theory. Also, both WKB theories have a slight, but consistent overestimation of the admittance. This is probably related to finite temperature corrections to the cold fluid theory that are neglected in the WKB approach used here.

In the next figures we vary the magnetic field strength. In FIG. 2.10 we vary Ω from 4 to 10 for an $\ell = 4$ perturbation, and in FIG. 2.11 we do the same for an $\ell = 2$ perturbation. For a

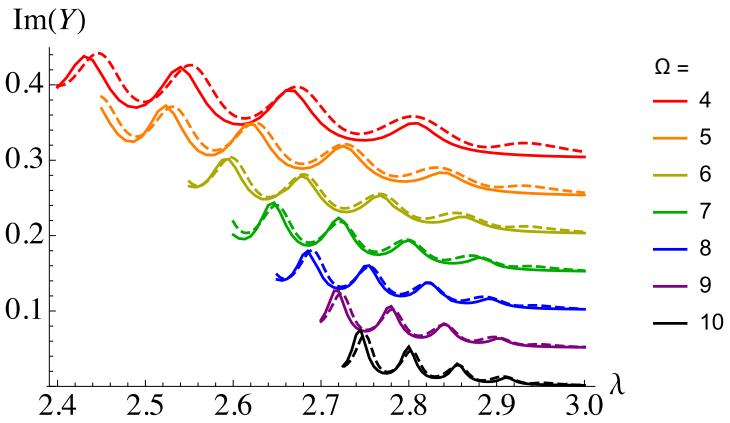

Figure 2.10: A family of Admittance plots (solid: Vlasov Theory; dashed: New WKB theory). $r_p = 4.76$, $r_W = 10$, and $\ell = 4$. $1/\nu = 2000 \cdot 2^{\frac{\Omega-10}{2}}$ (traces shifted vertically in steps of $1/20$, with $\Omega = 10$ trace unshifted).

given peak (corresponding to the number of radial nodes in the wave), the relative error in the scaled mode frequency λ tends to decrease as magnetic field increases from $\Omega = 4$ to $\Omega = 10$. (This is easiest to see in the second and third peaks, counting from the right). This is because the criterion for WKB theory to be valid is $k'(r)/k \ll k$, and k increases as magnetic field increases. This WKB criterion can also be written as $k\mathcal{L} \gg 1$ since $k/k' \approx \mathcal{L}$.

Interestingly, for a given magnetic field strength the figures show that the WKB method tends to produce more accurate results toward the right side of the plots, for larger frequencies and therefore *smaller* k (although the WKB theory tends to predict a weak extra peak at the largest

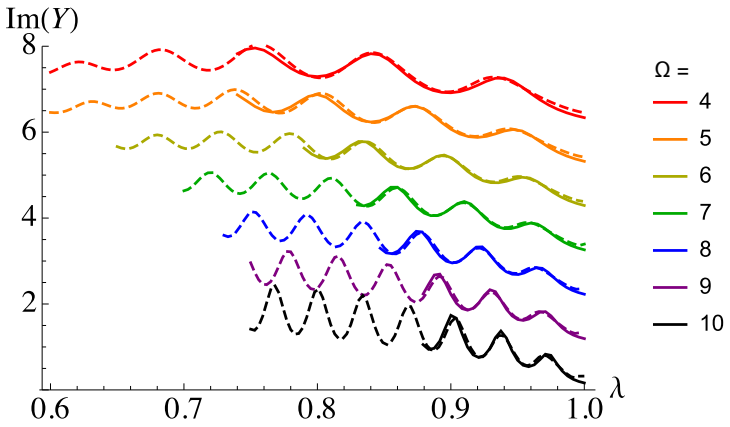

Figure 2.11: A family of Admittance plots (solid: Vlasov Theory; dashed: New WKB theory). $r_p = 4.76$, $r_W = 10$, and $\ell = 2$. $1/\nu = 2000 \cdot 2^{\frac{\Omega-10}{2}}$ (traces shifted vertically in steps of 1, with $\Omega = 10$ trace unshifted).

frequencies and for smaller magnetic fields). This can be understood because k'/k also varies as the frequency varies. As the frequency drops, k'/k becomes larger because the upper hybrid radius shifts to a larger radius where the density profile is steeper. A second reason for the increase in k'/k at lower frequencies is the appearance of wave-particle resonances. These resonances occur at radii r_{wpr} where the dielectric constant ε_{11} diverges. According to Eq. (2.7), the divergences occurs where $\hat{\omega}^2 - \Omega_v(\Omega_v - r\omega'_f) = 0$. Around such locations there is a strong resonant interaction between the wave electric field and particle cyclotron motion, which causes Landau damping of the wave. WKB theory breaks down here because as ε_{11} diverges k' also diverges. In FIG. 2.12 we plot the WKB criterion $k_0 \mathcal{L}_{min}$ versus frequency, where $\mathcal{L}_{min} = \min[\mathrm{Re}(\varepsilon_{11}/\varepsilon'_{11}(r))]$ is the minimum gradient scale length across the radial profile, and $k_0 = \mathrm{Re}[k(r=0)]$ is the real part of the central wavenumber. The WKB convergence parameter $k_0 \mathcal{L}_{min}$ approaches zero at the first appearance of a wave-particle resonance in the plasma, which occurs at frequencies on the left side of the plots for $\ell = 2$ and $\ell = 4$. The WKB parameter also decreases at higher frequencies, to the right side of the plots where the wavenumber of the modes is smaller. Consequently, the WKB method should work best at intermediate values of the frequency (and, of course, at larger magnetic fields). This expected behavior roughly corresponds to the results shown in

FIGs. 2.9-2.11.

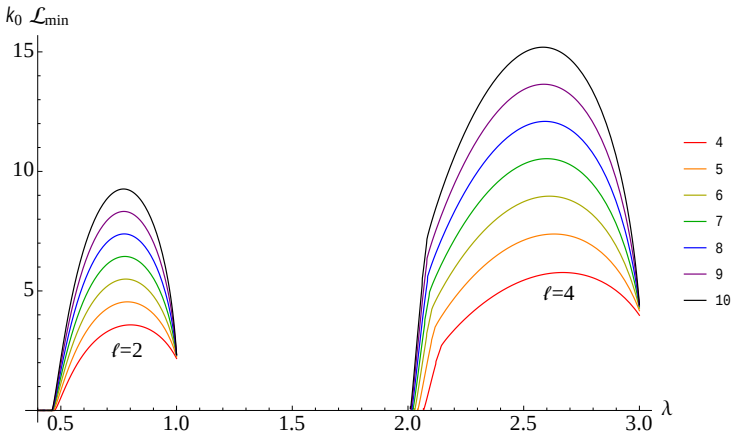

Figure 2.12: The WKB parameter $k_0\mathcal{L}_{min}$ plotted versus scaled frequency λ for a range of magnetic fields and for both $\ell = 2$ (left) and $\ell = 4$ (right), for the waves and magnetic fields considered in FIGs. 2.10 and 2.11. WKB theory works best when $k_0\mathcal{L}_{min} \gg 1$.

2.7 Limiting form for the Mode Frequencies

It would be useful to have an analytic expression to approximate the Bernstein Mode frequencies without having to numerically solve the fluid theory solution and impose a jump condition at $r_{\rm UH}$. In this regard, the analytic large magnetic field dispersion relation used in the old WKB theory, Eq. (2.97), is useful. A significant simplification can be made in the limit where the wall radius is large, $r_{\rm w}/r_p \to \infty$. In this case the argument of the arctan function in Eq. (2.97) approaches infinity. For instance, in the former limit, the Cauchy Principal integral is dominated by the vacuum region where $\mathcal{D} \to 1$, and the integrand grows without bound as a simple power law. Consequently, the argument of the arctan term approaches $\pi/2$. Making this approximation, Eq. (2.97) can be simplified to read

$$\int_0^{r_{\rm UH}} k dr = (\frac{\ell}{2} + n)\pi. \tag{2.98}$$

Although this result was obtained from the large magnetic field limit of the theory, it no-longer depends on the large-field fluid solution and so we might hope that it is more generally correct. We will test this hypothesis below. First, however, to standardize the integer n so that n indexes the modes starting from 1, we impose the constraint that the integral in Eq. (2.98) must be strictly positive, since $k > 0$ for $0 < r < r_{\rm UH}$. The issue is that $\ell/2$ term can be larger than 1, meaning that subtracting 1 from $n = 1$ (the lowest solution, by definition) would still produce a strictly positive right-hand side solution, which is not what we want. To solve this, we redefine n to absorb the largest integer that is still strictly less than $\ell/2$. The effect is that the right-hand side reads $n\pi$ when ℓ is even, and $(n-1/2)\pi$ when ℓ is odd:

$$\int_0^{r_{\rm UH}} k dr = (n + \mathrm{mod}(\ell, 2)/2)\pi. \tag{2.99}$$

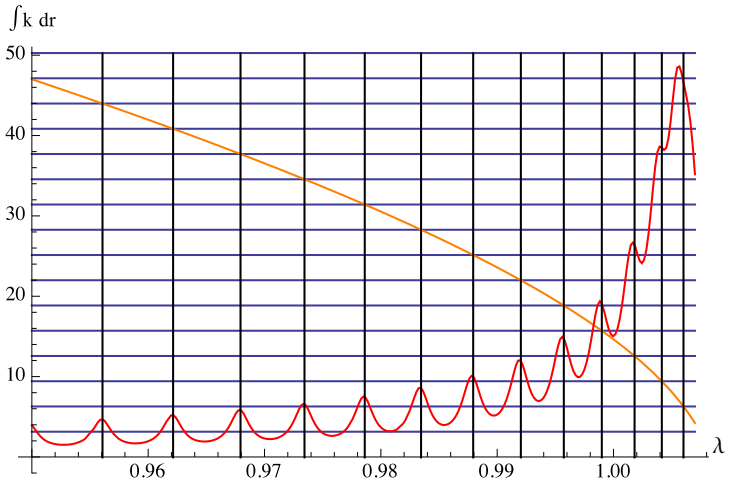

Figure 2.13: Determination of mode frequencies from Eq. (2.99). Orange curve: $\int_0^{r_{\rm UH}} k\, dr$, horizontal lines: $(n + \mathrm{mod}(\ell, 2)/2)\pi$, vertical lines: intersection of orange curve with horizontal blue lines, red peaks: ImY from the new WKB theory multiplied by $(r_W/r_p)^{2\ell}$ (scaled vertically to fit). $\Omega = 10$, $R_p = 20, \ell = 2, r_{\rm w}/r_p = \infty$.

Again, Eq. (2.99) assumes $r_{\rm w}/r_p$ is large. The functions $k(r)$ and $r_{\rm UH}$ must be calculated exactly using Eq. (2.63) as a function of the driving frequency. This result is similar to a result in

Ref. [6], where instead the limit $\mathcal{L}/r_{\mathrm{UH}} \ll 1$ was assumed; i.e. a nearly square density profile. While we tried assuming a square profile with upper hybrid radius equal to the plasma radius by writing $\int_0^{r_{\mathrm{UH}}} k dr \approx k(0) r_p$, this completely misrepresents the lowest-order modes because r_{UH} actually increases from zero quite rapidly for the first few modes due to the non-rectangular profile. Unfortunately, correct determination of Bernstein mode frequencies is strongly dependent on the assumed plasma profile. To understand this strong dependence, we can think of the right-hand side of Eq. (2.99) (divided by π) as counting the number of half-wavelengths within a radius r_{UH}. For the low-order modes, r_{UH} is very sensitive to profile shape in the nearly uniform region of the plasma (since even a small variation in the falloff of $k(r)$ corresponds to a large variation of r_{UH} due to the small gradient of $k(r)$). Consequently, even if $k(r)$ were known precisely, the number of half-wavelengths within this variable r_{UH} is also variable. On the other hand, for higher order modes, while r_{UH} is less sensitive to profile shape (since r_{UH} falls somewhere in the relatively thin plasma edge), $k(r)$ is larger, so even a small variation in r_{UH} admits a larger variation in the number of allowable half-wavelengths. In FIG. 2.13, the New WKB theory peaks are plotted against the prediction of the mode frequencies for infinite wall radius via Eq. (2.99). As can be seen, the mode frequencies are very well predicted by Eq. (2.99) for infinite wall radius, even for a warm plasma that doesn't satisfy $r_{\mathrm{UH}} \gg \mathcal{L}$.

2.8 Extension to Multiple Species

The analysis of previous sections can be extended to a multi-species plasma in a straightforward way. We make the assumption that the plasma is warm enough to not be centrifugally separated, which is done both as a simplifying assumption for the theory as well as to compare to experiments that operate in this regime, where Bernstein modes are more easily observed.

2.8.1 Resonant Species Approximation with no Species Separation

If the plasma species are not centrifugally separated, the densities of each species are related according to

$$n_\alpha(r) = \delta_\alpha n_{\rm tot}(r),\ \alpha = 1,2,\cdots n,$$

where $\delta_\alpha = n_\alpha(0)/n_{\rm tot}(0)$ is the central species concentration of species α. Consequently, knowledge of $n_{\rm tot}$, along with the species fractions is sufficient to determine the equilibrium for each species individually. To calculate this equilibrium, we note that under the approximation that the species are not centrifugally separated, the total unperturbed density $n_{\rm tot}$ behaves as a single species, so the equilibrium Eq. (2.2) still holds, where all quantities are normalized to the central parameters associated with the total plasma.

Then the multi-species generalization of the local WKB dispersion function Eq. (2.64) is

$$\mathcal{D}(\omega,k,r) = 1 - 2\sum_\alpha X_\alpha(\omega,r)\frac{e^{-\Lambda_\alpha} I_1(\Lambda_\alpha)}{\Lambda_\alpha}, \tag{2.100}$$

where $\Lambda_\alpha = k^2 r_{c\alpha}^2$ and X_α can be written as

$$X_\alpha(\omega,r) = \frac{{\omega_{p\alpha}}^2}{\hat{\omega}^2 - \Omega_{v\alpha}(\Omega_{v\alpha} - r\omega_f')}. \tag{2.101}$$

Here, $\Omega_{v\alpha} = \Omega_\alpha - 2\omega_f$, and Ω_α, $\omega_{p\alpha}$, and $r_{c\alpha}$ are the cyclotron frequency, plasma frequency and cyclotron radius of species α respectively. As in Eq. (2.64), we have dropped resonant terms at multiples of the cyclotron frequency for each species, since we are interested in the main resonance at the fundamental cyclotron frequency. There will then be a solution of the dispersion relation $\mathcal{D} = 0$ for each species; i.e. each species has a cyclotron wave associated with it.

In order to make further progress we will simplify this result assuming that the magnetic field is large. In this case we know that the plasma response is peaked in a narrow frequency range around the cyclotron frequency for each species, with $\omega - \Omega_\alpha \approx \omega_{p\alpha}^2/\Omega_\alpha$. We assume that

the magnetic field is large enough so that this range is small compared to the difference between any two cyclotron frequencies: $\Omega_\alpha - \Omega_\beta \gg \omega_p^2/\Omega$. In this case, for cyclotron waves associated with a given species β with $\omega \approx \Omega_\beta$, only the resonant term with $\alpha = \beta$ need be kept in the sum in Eq. (2.100) because $X_\alpha \ll X_\beta$, and the equation simplifies to

$$\mathcal{D}(\omega,k) = 1 - 2X_\beta(\omega)\frac{e^{-\Lambda_\beta} I_1(\Lambda_\beta)}{\Lambda_\beta}. \tag{2.102}$$

In other words, in this approximation we ignore the response of all non-resonant species. In this case the WKB theory carries through just as for a single species (the resonant species). Also, this approximation can easily be applied to the numerical Vlasov solution. Here, all species contribute to the equilibrium electric field appearing in Eq. (2.39), but δf is evaluated only for the resonant species.

2.8.2 Necessary conditions for Bernstein Modes

An important question to consider is "Under what conditions are Bernstein modes possible in a multi-species thermal equilibrium plasma?". As previously discussed for a single-species plasma, Bernstein waves can only propagate when $\mathrm{Re}(\varepsilon_{11}) < 0$. For a multi-species plasma in the resonant species approximation, this corresponds to $X_\beta > 1$ for resonant species β. There is a range of frequencies near Ω_β where this inequality is satisfied. To find this range, we utilize the high magnetic field limiting form of X_β:

$$X_\beta = \frac{\delta_\beta \cdot n}{\lambda + (2-\ell)\langle n\rangle + \frac{r\langle n\rangle'}{2}} = \frac{\delta_\beta \cdot n}{\lambda + (1-\ell)\langle n\rangle + n}, \tag{2.103}$$

where n is the total density scaled to the total density at $r = 0$, $\lambda \equiv \frac{\omega - \Omega_\beta}{\omega_E}$, $\omega_E = 2\pi e c n(r=0)/B$ is the central ExB rotation rate, $\langle n\rangle$ is the average total density within a radius r, and δ_β is the fraction of the mode resonant species β. The final expression follows by carrying out the radial

derivative of $\langle n \rangle$. The expression in Eq. (2.103) is useful because it allows insight into where both the cutoffs and wave-particle resonances occur:

$$\lambda = (\ell - 1) \langle n \rangle_r - (1 - \delta_\beta)\, n(r) \qquad \text{(cutoff)} \tag{2.104}$$

$$\lambda = (\ell - 1) \langle n \rangle_r - \; n(r). \qquad \text{(resonance)} \tag{2.105}$$

At the cutoff, $Re[X_\beta] = 1$ ($Re[\varepsilon_{11}] = 0$) while at the wave-particle-resonance, $X_\beta \to \infty$. A cutoff is typically required in order for propagating solutions to exist because $\varepsilon_{11} = 1$ outside the plasma but $Re[\varepsilon_{11}] < 0$ is necessary for wave propagation. Another way for ε_{11} to change sign is to go through infinity, at a wave-particle-resonance (WPR). However, a wave-particle resonance in the plasma strongly Landau-damps the Bernstein waves, so we look for conditions where the plasma has a cutoff but no resonance. For $\ell = 0$ or $\ell = 1$ Eqs. (2.104) and (2.105) imply that a cutoff is always accompanied by a resonance at a somewhat larger radius, so the Bernstein response is heavily-damped. However, for $\ell > 1$ one can find a frequency range with a cutoff but no resonance. The right-hand sides of Eqs. (2.104) and (2.105) are functions of r, and have maximum values as a function of r. Note that the maximum value for the wave particle resonance condition is clearly less than that for the cutoff condition.

Thus, for Bernstein modes to occur, λ must be less than the maximum value given by Eq. (2.104) but greater than the maximum given by Eq. (2.105): $\lambda_{\text{wpr}} < \lambda < \lambda_{\text{cut}}$ where

$$\lambda_{\text{cut}} = \max\left((\ell - 1) \langle n \rangle_r - (1 - \delta_\beta)\, n(r) \right) \tag{2.106}$$

$$\lambda_{\text{wpr}} = \max\left((\ell - 1) \langle n \rangle_r - \; n(r) \right), \tag{2.107}$$

and where $\max()$ is the global maximum operator as r varies. Notice that the wave-particle

resonance does not depend on δ_β because δ_β does not appear in the denominator of X_β. In fact,

$$\lambda_{\text{wpr}} = \lambda_{\text{cut}}|_{\delta_\beta \to 0}\,. \tag{2.108}$$

Consequently, plasmas with a small fraction δ_β of the resonant species exhibit Bernstein modes only over a narrow range of frequencies, so future experiments on Bernstein modes should strive to make the resonant species fraction as large as possible.

The next task is to understand the dependence of λ_{cut} and λ_{wpr} on the remaining parameters of the plasma, δ_β, r_p, and ℓ. In FIG. 2.14, it is clear that the Bernstein range in λ satisfies $\ell - 2 < \lambda < \ell - 1$, with warmer (i.e. smaller r_p) plasmas extending through that entire range, except for $\ell = 2$, which first acquires a wave-particle resonance at a higher frequency than $\lambda = \ell - 2 = 0$. It is also interesting to note that in the case of $\ell = 4$, the bottom limit of ω_{wpr} becomes constant at sufficiently small r_p due to the appearance of a second wave-particle resonance that first appears at the very center of the plasma, at a higher frequency than the wave-particle resonance appearing at non-zero r. The kinks in the curves for λ_{cut} at various δ_β show whether the region in which there are Bernstein wave solutions is a disk-shaped region or an annular region. That is, for sufficiently large r_p, the plasma has two upper hybrid radii. These annular solutions only occur for $\delta_\beta < 1$.

To understand the fluid theory in a concrete situation, we now study a particular plasma with parameters chosen to match some typical experimental conditions. Figure 2.15 shows several traces of $\varepsilon_{11}(r) = 1 - X_\beta$ for a range of driving frequencies. The red (dotted) curve shows the lowest frequency for which some part of the plasma has $\varepsilon_{11} < 0$ for $\nu = 0$, due to the dip in ε_{11} at roughly $r = 11.5$. This frequency is how we defined λ_{cut}, as shown by the dashed lines in FIG. 2.14. In this case $\varepsilon_{11} < 0$ only in a small region away from the origin, that is, this plasma exhibits Bernstein modes in an annular region, with evanescence both near the plasma center, and at the very edge of the plasma. As the driving frequency is lowered further, the dip in ε_{11} becomes

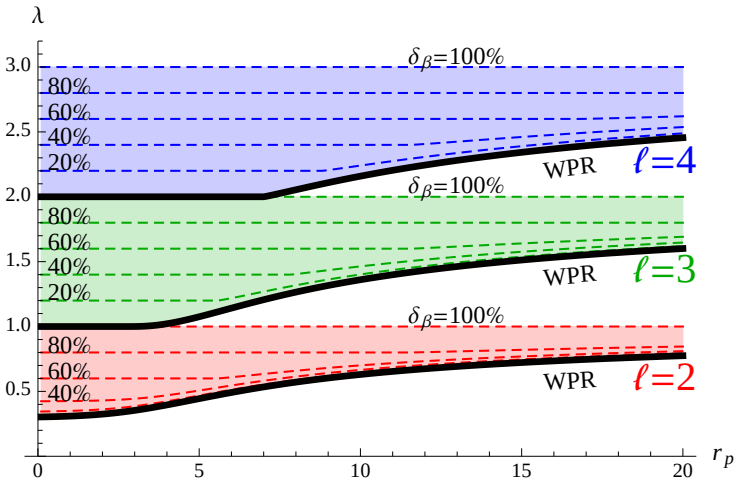

Figure 2.14: Predicted ranges of λ over which Bernstein modes occur in WKB theory for a multi-species plasma without species separation: $\lambda_{wpr} < \lambda < \lambda_{cut}$, as a function of scaled plasma radius for $\ell = 2$ through $\ell = 4$, with resonant species fraction $\delta_\beta \in \{100\%, 80\%, 60\%, 40\%, 20\%\}$.

increasingly deep until at some frequency $\lambda_{\rm wpr}$ the denominator appearing in ε_{11} vanishes and two wave-particle resonances are produced that damp out the Bernstein waves, as indicated by the thick black lines in FIG. 2.14.

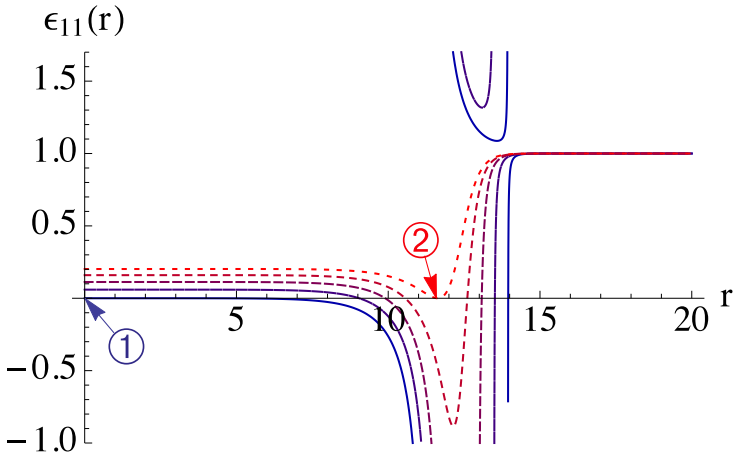

Figure 2.15: $\varepsilon_{11}(r)$ in a plasma with $\ell = 2$, $\Omega = 10.45$, $r_p = 10.5$, $\delta_\beta = 56.3\%$, $r_w = 83.54$, with driving frequencies starting from $\lambda = 0.711$ (red, dotted), down to $\lambda = 0.568$ (blue, solid). Locations where $\varepsilon_{11}(r) = \varepsilon'_{11}(r) = 0$ labeled.

2.8.3 Multi-species Results

In FIG. 2.16 we compare the multi-species results of the WKB theory for $\ell = 2$ modes in an $\Omega = 10$, $r_p = 4.76$ plasma, with two values of the resonant species purities δ_β, using the resonant-species approximation discussed previously. First, we take $\delta_\beta = 80\%$. Notice that the

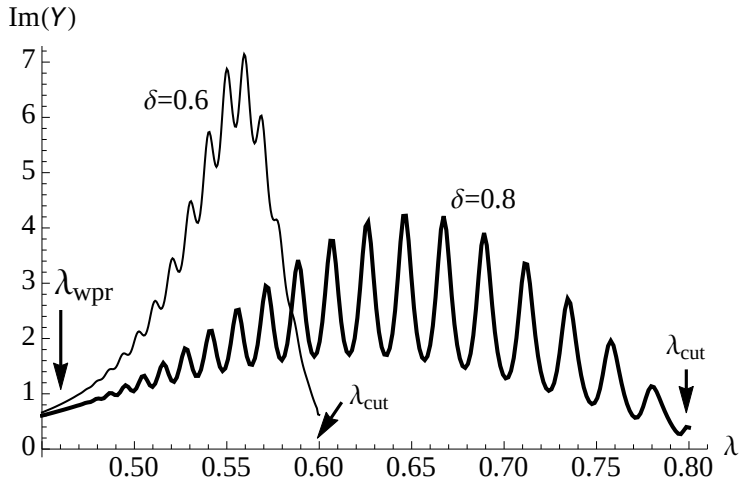

Figure 2.16: Imaginary part of the admittance for a multi-species plasma, using the WKB theory, for two resonant species fractions, $\delta_\beta = 60\%$ and 80%. $\Omega = 10$, $r_p = 4.76$, $r_W = 10$, $\ell = 2$ and $1/\nu = 4000$. Compare the fall-off of the response to the predictions for λ_{wpr} and $\lambda_{\rm cut}$ provided by FIG. 2.14 (arrows).

right side of FIG. 2.16 is at $\lambda = 0.8$, in agreement with the prediction by FIG. 2.14, since no Bernstein peaks appear at frequencies higher than this according to WKB theory. There appears to be a significant reduction in peak spacing compared to the pure plasma case (FIG. 2.11).

Next we consider an identical plasma except with $\delta_\beta = 60\%$. Again, the plot starts on the left at $\lambda = 0.6$, as expected from the appearance there of an $\ell = 2$ wave-particle resonance in this profile shown in FIG. 2.14. We also observe that the Bernstein peaks are more difficult to observe in a $\delta_\beta = 60\%$ plasma, especially for frequencies approaching $\lambda_{\rm cut}$ than it was for the $\delta_\beta = 80\%$ plasma. This is because the peak spacing is even closer together in the $\delta_\beta = 60\%$ plasma.

2.8.4 $\ell = 0$ Bernstein modes

We now briefly consider excitation and measurement of the $\ell = 0$ plasma response to an external perturbation near the cyclotron frequency, and compare these results to simulations by Hart and Spencer of $\ell = 0$ cyclotron waves[10]. There are two ways in which the $\ell = 0$ plasma response differs from the $\ell \neq 0$ response discussed previously.

First, for $\ell = 0$ a wave-particle resonance occurs that strongly damps Bernstein modes. Although previously we argued that Bernstein waves are completely absorbed at a wave-particle resonance, we will see that sometimes a weak Bernstein mode can still be set up. When the resonant radius occurs in the region of the plasma edge, and if this edge density falls rapidly to zero, a new effect occurs: Bernstein waves are partially reflected at the sharp plasma boundary rather than being completely absorbed, creating a damped standing wave inside the plasma. This is an effect beyond WKB theory. We therefore rely on numerical Vlasov solutions, comparing them to the predictions of cold fluid theory (which does not include the Bernstein response at all), and to the particle simulations of Hart and Spencer.

Second, we cannot drive an $\ell = 0$ plasma wave using an external wall potential, since a cylindrically-symmetric $z-$independent wall potential does not create a radial electric field for $r < r_W$. Also, $\ell = 0$ plasma oscillations cannot be detected at the wall, by Gauss's law in two-dimensions. (Experimentally, there can be z-dependence in the driver, and the plasma is finite-length, but such effects are beyond the two-dimensional theory presented here). We therefore must drive the plasma in a different manner than for $\ell \neq 0$, and we must diagnose the modes using a new definition of plasma admittance.

We will drive the plasma with an oscillatory θ-independent potential of the form $\delta\Phi_{ext}(r)e^{-i\omega t}$, where $\delta\Phi_{ext}(r)$ does *not* satisfy the 2-D Laplace equation; instead we simply take $\delta\Phi_{ext}(r) = Ar^2$. One can think of this as some approximation to the effective 2-D (z-averaged) driving one would obtain in a finite-length plasma from a z-dependent wall voltage.

Next, we require a new form for the admittance function. Hart and Spencer define their

measure of the $\ell = 0$ plasma response as the amplitude of the radial component of the fluid velocity, δV_r, at a fixed location on the interior of the plasma, $r_{\rm meas}$. We will use a related dimensionless quantity we call Y_a, the "acceleration admittance", defined as the (negative of) the radial acceleration of a fluid element at a given location $r_{\rm meas}$, divided by the acceleration produced by the external potential only:

$$Y_a \equiv -\frac{i\omega\delta V_r}{\partial\delta\Phi_{ext}/\partial r}\Big|_{r=r_{meas}} \tag{2.109}$$

Like the admittance Y, the quantity Y_a is independent of the amplitude A of the external driving potential; its imaginary part depends only on the plasma response; and it is sharply-peaked at the frequencies of weakly-damped normal modes.

There are (at least!) two ways to determine this admittance function from the Vlasov solution. In one method, one can integrate the numerically-determined distribution function δf over velocities to determine δV_r, and use this result in Eq. (2.109). Another, simpler, method uses a relation between δV_r and the perturbed plasma potential, $\delta\Phi_p$. To derive this relation, begin with the linearized continuity equation

$$-i\omega\delta n + \nabla\cdot\left(n\delta\mathbf{V} + \delta n\mathbf{V}_f\right) = 0, \tag{2.110}$$

where $\mathbf{V}_f(r) = \omega_f(r) r\hat{\theta}$ is the equilibrium cold-fluid rotational velocity and $n(r)$ is the equilibrium density (see Eqs. (2.1) and (2.9)). Integrating this equation over a disk of radius r centered with the plasma, and using the divergence theorem, we obtain

$$\oint n\delta\mathbf{V}\cdot\hat{n}ds + \oint \delta n\mathbf{V}_f\cdot\hat{n}ds = \int i\omega\delta n d^2r. \tag{2.111}$$

The second term on the left vanishes due to the purely azimuthal equilibrium flow. Using the

Poisson equation

$$\nabla^2 \delta\Phi_p = -\delta n. \tag{2.112}$$

another application of the divergence theorem, and cylindrical symmetry for $\ell = 0$, the right side of Eq. (2.111) can be expressed in terms of the radial plasma electric field, which gives the following expression for the perturbed radial velocity for an $\ell = 0$ plasma:

$$\delta V_r(r) = -\frac{i\omega}{n(r)} \frac{\partial \delta\Phi_p}{\partial r}. \tag{2.113}$$

We will use this result in Eq. (2.109) to determine the plasma response to an external potential oscillation for $\ell = 0$ using the Vlasov code. We will also compare these numerical Vlasov code results to the predictions of cold fluid theory. However, since the driving potential does not satisfy the Laplace equation, the cold fluid theory of Eq. (2.6) must be modified. The linearized cold fluid equations from which it is derived are the continuity and Poisson equations Eq. (3.1) and Eq. (2.112), as well as the linearized momentum equation,

$$-i\omega\delta\mathbf{V} + \mathbf{V}_f \cdot \nabla\delta\mathbf{V} + \delta\mathbf{V} \cdot \nabla\mathbf{V}_f = -\nabla\delta\Phi_p - \nabla\delta\Phi_{ext} - \Omega\delta\mathbf{V} \times \hat{z}. \tag{2.114}$$

These three equations can be combined to yield

$$\nabla \cdot \varepsilon \cdot \nabla\delta\Phi_p = \nabla \cdot (1 - \varepsilon) \cdot \nabla\delta\Phi_{ext}, \tag{2.115}$$

where ε is the cold-fluid dielectric tensor given by Eq. (2.7). This is a generalization of Eq. (2.6) to forcing potentials that do not satisfy the 2-d Laplace equation. If $\delta\Phi_{ext}$ did satisfy the Laplace equation, it could be combined with the plasma potential $\delta\Phi_p$ as $\delta\Phi = \delta\Phi_p + \delta\Phi_{ext}$ and $\delta\Phi$ would satisfy Eq. (2.6).

For $\ell = 0$ Eq. (2.115) can be solved analytically. Writing out the gradients in cylindrical

geometry yields

$$\frac{1}{r}\frac{\partial}{\partial r}\left(r\varepsilon_{11}\frac{\partial\delta\Phi_p}{\partial r}\right)=\frac{1}{r}\frac{\partial}{\partial r}\left(r(1-\varepsilon_{11})\frac{\partial\delta\Phi_{ext}}{\partial r}\right) \tag{2.116}$$

This equation can be integrated once. The constant of integration must be dropped to keep the potential finite at the origin, and therefore we have

$$\frac{\partial\delta\Phi_p}{\partial r}=\frac{1-\varepsilon_{11}}{\varepsilon_{11}}\frac{\partial\delta\Phi_{ext}}{\partial r} \tag{2.117}$$

Applying this expression to Eq. (2.113) and using this result in Eq. (2.109) yields the following expression for the acceleration admittance in cold fluid theory:

$$Y_a=\left.\frac{\omega^2(\varepsilon_{11}-1)}{n(r)\varepsilon_{11}}\right|_{r=r_{meas}}. \tag{2.118}$$

In FIG. 2.17 we compare the cold-fluid prediction for $Im[Y_a]$ from Eq. (2.118) to the numerically-determined values from the Vlasov code for the standard plasma profile with $r_p =$ 4.76 , $r_W = 10$. There are several differences in these results compared to previous $\ell \neq 0$ results. First, for $\ell = 0$ there are no secondary Bernstein peaks within the primary admittance peak. Also, the frequency at which the single peak occurs depends on which radius it is measured at. (For global normal modes this would not be the case.)

The cold fluid predictions give primary peaks at the same frequency locations as does the code. From Eq. (2.118), the peaks occur where $Re[\varepsilon_{1,1}(r,\lambda)] = 0$, which explains why the frequency λ of the peak varies with radius r: in fluid theory these peaks are local upper-hybrid oscillations excited by the forcing at the location where the upper hybrid frequency is equal to the forcing frequency. However, the code results are not as sharply-peaked as the fluid theory predicts, indicating there is some extra damping mechanism at work.

This damping mechanism becomes apparent when the perturbed density predicted by the Vlasov code is plotted versus radius. This is done in FIG. 2.18 for frequency $\lambda = -1$. Between the

cutoff radius r_{cut} and a wave -particle resonance at $r_{wpr} > r_{cut}$ a Bernstein wave causes the density to oscillate in r, with increasing wavenumber as the wave-particle resonance is approached. This is qualitiatively similar to what one would expect in WKB theory, since $X \to \infty$ at the wave-particle resonance, implying that $k \to \infty$ through Eq. (2.64). However, WKB theory would also predict that the wave becomes evanscent for $r > r_{wpr}$ as $Re[\varepsilon_{11}]$ changes sign, but this is not what the Vlasov code shows. On the other hand, the WKB equations do not apply near the resonance, so it is perhaps unsurprising that there is a discrepancy. To our knowledge, there is currently no detailed theoretical model for the behavior of the perturbed density in a Bernstein wave near a wave-particle resonance. This problem differs from, and is more difficult than, the standard "magnetic beach"[19] absorption of cyclotron waves with nonzero wavenumber k_z along the magnetic field. For $k_z = 0$ the wave-particle resonance mechanism involves drifting cyclotron orbits in a radially-nonuniform equilibrium electric field, and is consequently considerably more complex.

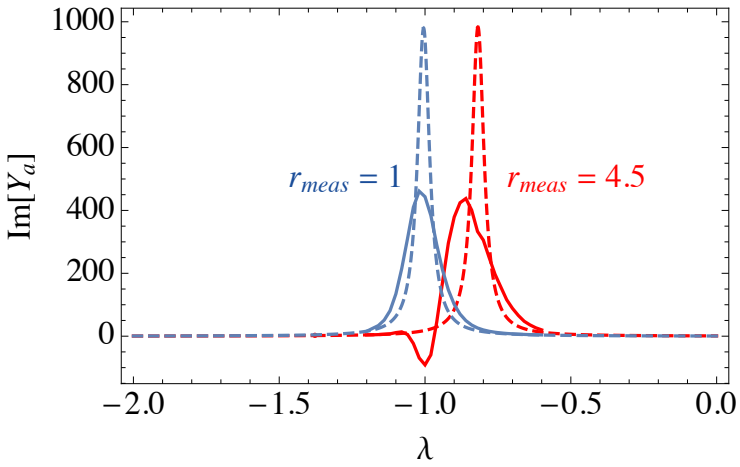

Figure 2.17: Imaginary part of the acceleration admittance, measured at two radii, plotted versus scaled frequency λ for $\ell = 0$, for a plasma with $r_p = 4.76$, $r_W = 10$, and $\Omega = 5$. Dashed lines are the fluid theory prediction, Eq. (2.118), and solid lines are the results of the Vlasov code with $M_r = 180, M_v = 90, M_\psi = 18$.

However, we can qualitatively understand the mode broadening and increased damping caused by this Bernstein wave. One can see in FIG. 2.18 that the real and imaginary parts of the

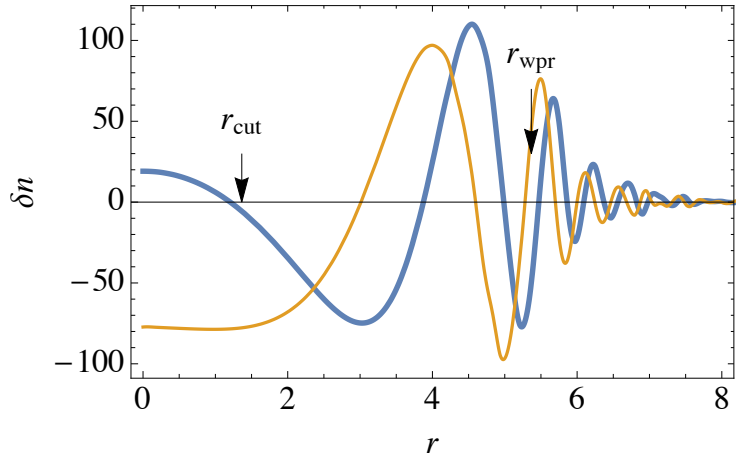

Figure 2.18: Real (thick line) and imaginary (thin line) parts of the perturbed density δn versus radius, from the Vlasov code solution, for frequency $\lambda = -1$, for the same conditions as the previous figure. The small rapid oscillations on the right-hand side of the figure are not fully-converged, but the oscillations near and to the left of r_{wpr} are well-converged.

oscillatory density perturbation are roughly 90^o out of phase, indicating a travelling wave rather than a standing wave. The oscillating source $\delta\Phi_{ext}$ is launching a Bernstein wave perturbation that is absorbed at the wave particle resonance, sapping energy from the plasma response. This Bernstein wave does not set up a normal mode because of the absorbing "boundary condition" for the wave at the location of the wave-particle resonance. The damping caused by wave absorption at the resonance is not included in the cold fluid analysis (because this analysis entirely neglects Bernstein waves), and this is why the admittance peaks are sharper in cold fluid theory.

Similar enhanced damping caused by Bernstein wave absorption at a resonance was predicted via WKB analysis for $\ell \neq 0$ Bernstein waves, in Ref [6], Sec. IXC.3. One complication in any similar WKB analysis for the $\ell = 0$ response is that the waves are now launched by a source $\delta\Phi_{ext}$ that is nonzero within the plasma. This requires a solution to the inhomogeneous wave equation, involving a WKB expression for the Green's function associated with the Bernstein mode operator; this Green's function solution was not required in Ref. [6] because there the source was a potential oscillation on the wall, outside the plasma. The WKB Green's function would produce both a fluid and a Bernstein wave response to forcing, but its functional form has

not yet been derived.

We now describe the $\ell = 0$ plasma response for a second case, a plasma at lower temperature and weaker magnetic field than in the previous example: $\Omega = 1.633$, $r_p = 43.67$, and $r_W = 2r_p$. This is the case studied by Hart and Spencer. This is a plasma with a nearly uniform density and a relatively sharp edge. Figure 2.19 shows the result of our numerical Vlasov method for an $\ell = 0$ perturbation. There is a large peak in the admittance at $\lambda \approx -1.2$. This admittance peak is fairly well described by the cold fluid theory (the dashed line). This is an upper hybrid mode (the cold fluid admittance is peaked at the upper hybrid frequency where $Re[\varepsilon_{11}] = 0$; see Eq. (2.118)). However, there are also two other weaker peaks in the admittance that are not in the cold fluid theory. These peak locations in the plasma response were also observed in the simulations by Hart and Spencer (the arrows). These peaks are fairly strongly-damped Bernstein modes.

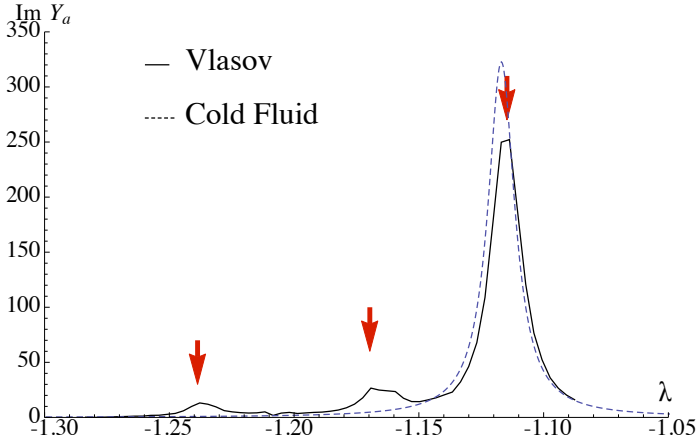

Figure 2.19: Comparison of the Vlasov code, cold fluid theory, and the PIC simulation by Hart and Spencer. $\Omega = 1.633$, $r_p = 43.67$, $r_{\text{meas}} = 27.5$, $\ell = 0$, and $\nu = 1/500$. Vlasov code uses M_ψ=20, $M_r = 240, M_v = 90$. Arrows show the locations of modes found in the simulations of Ref. [10].

In FIG. 2.20 we display the real and imaginary parts of the perturbed density from the Vlasov code for λ values at the three peaks. The big "cold fluid" peak is a simple "breathing mode" where the density change throughout the plasma is nearly uniform, as the plasma radially expands and compresses. There is nearly no Bernstein wave activity, which explains why cold

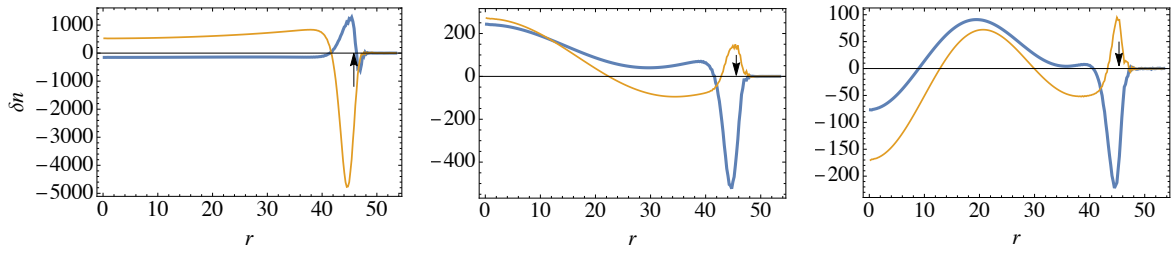

(a) (b) (c)

Figure 2.20: Real (thick line) and imaginary (thin line) parts of the perturbed density response for $\ell = 0$ in a cold weakly-magnetized plasma, at three frequencies corresponding to the peaks of the admittance in FIG. 2.19. (a) $\lambda = -1.11$ (b) $\lambda = -1.17$ (c) $\lambda = -1.24$.

fluid theory is a good fit to the admittance peak. The next two peaks show true Bernstein mode responses. The plasma density oscillates in space and the real and imaginary oscillations are not 90^o out of phase; these are (damped) standing waves, not travelling waves. There is no cutoff for these modes; the Bernstein waves propagate from $r = 0$ out to a wave-particle resonance in the plasma edge (shown by the arrows). Because the wave particle resonance occurs in the plasma edge, and this edge is sharp, Bernstein waves can apparently partially reflect from the edge before they are fully absorbed at the wave-particle resonance, setting up damped normal modes.

The large variation of δn in the plasma edge exhibited in these figures is due to the "surface charge" associated with wave motion of the sharp plasma edge. One might hope that one could model this problem using an appropriate warm fluid theory for a uniform plasma with a sharp edge, but we currently have no theoretical model for the correct wave boundary condition at this edge, since the edge both reflects and absorbs the wave due to the wave-particle resonance. Some progress has been made on this problem by treating the plasma as an elastic fluid with an anisotropic pressure tensor,[10] but this approach neglects the wave damping effect of the wave-particle resonance.

2.9 Conclusions

Two electrostatic cyclotron modes propagate in a nonneutral plasma column: surface cyclotron and Bernstein waves. In this chapter we have considered the z-independent ($k_z = 0$) versions of these waves. We focussed on these z-independent waves because for $k_z \neq 0$ there can be strong Landau-damping on the parallel velocity distribution via the "magnetic beach" mechanism[19] when $(\hat{\omega} - \Omega_v)/k_z$ is of order the thermal speed v_t. Since $\hat{\omega} - \Omega_v$ is of order the plasma rotation frequency ω_r, the condition for negligible Landau damping of $k_z \neq 0$ cyclotron modes can be written as $\omega_r \gg k_z v_t$. This regime requires cold plasmas, where the Bernstein response of chief interest in this chapter would be difficult to observe.

The surface wave propagates only along θ, and causes density perturbations confined to the surface of the plasma. The theory of these modes is adequately described by the cold fluid theory described in Section 2.3. These surface modes can be driven and detected from the wall by applying or measuring voltage on wall electrode sectors. In experiments these modes provide diagnostics for plasma density, species concentration, and charge to mass ratio.

On the other hand, the Bernstein wave is a finite temperature effect coming from the non-zero Larmor radius of the particle orbits, introducing radial variation extending from the plasma center to the upper-hybrid radius r_{UH}, where the waves become evanescent and eventually match onto the vacuum potential outside the plasma. This is possible because the upper-hybrid radius acts as a classical turning point, where the Bernstein waves are reflected, which enables a standing wave on the interior of the plasma. In general, a plasma can have more than one upper-hybrid radius, which causes annular regions where Bernstein modes are present, where the plasma dielectric $\varepsilon_{11} < 0$. We also found that for appropriate frequencies, it is possible for the plasma to have a local wave-particle resonance where the vortex frequency Ω_v matches the mode frequency as seen in the rotating frame. At radii where a resonance is present, or nearly present, the Bernstein wave energy is absorbed, making the measured wall signal significantly smaller.

Our theory began from a z-independent global thermal equilibrium density profile, and determined the linear modes and mode frequencies in two different ways. First, we described and presented results from a numerical solution to the Vlasov equation; and second, we derived a new WKB theory which corrects a frequency shift in the predicted mode frequencies (predicted in the existing literature[6]) for moderately-sized bare cyclotron frequency Ω. Mode frequencies were obtained and compared by picking out peaks in the admittance function $Y(\omega)$, where the mode is resonant.

The numerical solution to the Vlasov equation described in section 2.4 is valuable because it doesn't carry out the mathematical approximations used in the WKB theory, and therefore the results obtained from the code are "exact" (provided the numerics have converged). These numerical results showed both the surface cyclotron mode response, broadened in frequency by the variation of the $E \times B$ rotation rate across the plasma radius, as well as showing a number of individual Bernstein modes coupled to the surface cyclotron mode. We showed a number of results at various temperatures and magnetic fields, for single-species plasmas at various θ-mode numbers ℓ, and then described WKB theory and presented results for plasmas with multiple species. Finally, we compared to an existing azimuthally symmetric PIC simulation, and found good agreement with our Vlasov solution.

The semi-analytic WKB approach makes some simplifying assumptions, so these results were validated with the Vlasov method. In the WKB theory, the plasma was separated into four partially-overlapping regions where different approximations were made. For the center of the plasma, where the plasma density is uniform, we made use of the derivation in section 2.5.1 giving the general form for a differential wave equation operator in a uniform, isotropic plasma. Away from the origin where the plasma density changes gradually, the Bernstein dispersion relation was used to determine the local wavenumber as a function of radius, where Bernstein waves are present. Using a 4th order wave equation valid near r_{UH}, we found that the presence of an internal Bernstein mode only couples to the surface mode through the matching conditions on the cold

fluid perturbed potential $\overline{\delta\Phi}$ at r_{UH}. This matching condition is modulated by the local phase χ of the Bernstein wave, which is responsible for shifting the vacuum potential outside the plasma and ultimately changing the (normalized) electric field measured at the wall Y, which we used as a proxy for the plasma response. This new WKB theory has very good agreement with the Vlasov solution for $\Omega \geq 4\omega_p$, which was not the case for the existing WKB theory which assumed $\Omega \gg \omega_p$. We also found an approximate dispersion relation valid for strong magnetic fields and small plasma to wall radius ratio, which shows that the mode frequencies occur whenever the Bernstein wave phase χ changes by a multiple of π. We also provided a plot (FIG. 2.14) that predicts the frequency range in which Bernstein modes are allowed, as a function of the plasma radius scaled to the Debye length, ℓ, and the species concentration δ_β.

There are still some aspects of this problem that need to be extended or otherwise further studied. The results in this chapter were focused on Bernstein modes near the cyclotron frequency Ω, but there are also modes at multiples of Ω. Both of the main methods described in this chapter can be extended to consider such higher harmonic modes without trouble. Also, as we already noted, the theory described here is a 2D analysis; it assumes the axial mode number $k_z = 0$, and also that the plasma length is very long. Many experiments do not operate in this regime, so the theory may need to be extended to include finite length effects. Finally, our analysis brings up an interesting puzzle regarding the physics occurring near a wave-particle resonant radius. In this chapter, we found many circumstances under which such a resonant radius absorbs waves, attenuating Bernstein modes, and leading to smaller measured Bernstein mode wall signals. On the other hand, we also reviewed an example originally considered by Hart and Spencer[10] in which the plasma edge (containing the resonant radius) instead acts as a reflector, allowing damped standing waves to be generated on the interior of the plasma. The mechanism of this reflection and absorption is not fully understood, so this question should be pursued in future work.

2.10 Acknowledgements

Chapter 2, in full, is a reprint of the material as it appears in Physics of Plasmas: Daniel Walsh and Daniel H. E. Dubin, "Bernstein modes in a non-neutral plasma column", *Physics of Plasmas*, **25**, 052119 (2018). Daniel Walsh was the primary investigator and author of this paper.

The authors thank Prof. C. F. Driscoll and Drs. F. Anderegg and M. Affolter for useful discussions. This work was funded by DOE grant number DE-SC0018236.

Chapter 3

Finite-Length Diocotron Modes and Temperature Effects

3.1 Background

There has been extensive work done in trying to understand diocotron modes in non-neutral plasmas. These modes arise due to $\vec{E} \times \vec{B}$ drift dynamics, in which the guiding center of a charged particle undergoes a drift motion perpendicular to both the electric and magnetic fields. The mechanistic origin of this drift becomes obvious when considering that as the particle executes cyclotron motion due to the magnetic field, the particle velocity is greater on the portion of the orbit at lower electric potential energy, and conversely is lower on the portion with higher electric potential energy (by conservation of energy). This asymmetry implies that during each cyclotron orbit, the particle has moved farther on one side of the orbit than the other, leading to an average drift velocity along constant electric potential. The modes we consider here emerge when considering a plasma with a density of, say, $10^7 \mathrm{cm}^{-3}$, where both the self-consistent effects of plasma motion, and the particle-dynamics come into play. The 2-dimensional version of this problem, applicable to a plasma column of infinite length, is theoretically well-understood

for modes with azimuthal mode number ℓ. For instance, the infinite length theory for the frequency of the azimuthal mode number ℓ has a simple, closed-form expression for an (infinite) cylindrical plasma with uniform density. Another notable theoretical success due to Levy[14] is the understanding that the infinite-length $\ell = 1$ mode frequency is independent of the radial density profile, and is simply comprised of a translation to the equilibrium plasma. This $\ell = 1$ mode is driven entirely by the field produced by the image charges in the enclosing conductive cylindrical wall. On the other hand, the finite-length theory of diocotron modes is less developed, with a few notable exceptions: a $\ell = 1$ finite-length diocotron mode theory was developed by Fine and Driscoll [7] which calculated the diocotron mode frequency using the fact that the mode frequency is directly proportional to the net force on the plasma column exerted per column displacement (taking advantage of Levy's result). Another theory paper due to Hilsabeck and O'Neil [11] considers the same problem (focusing primarily on $\ell = 1$), but including bounce-averaging over the axial bounce motion, accounting for plasma end shape. In this paper, we demonstrate a relationship between these two theories– the first, an analytic theory only suitable for the $\ell = 1$ mode; and the second, the bounce-averaged kinetic numerics that can handle $\ell \geq 1$. In finding the connection between these approaches, we show how to develop a finite-length theory that takes the positive aspects of both theories: the new theory is a closed-form mathematical expression (like the Fine result), yet is also applicable to $\ell \geq 1$ (like the Hilsabeck result). We also show that this new theory recovers Fine's result for the special case $\ell = 1$.

3.2 Infinite Length Fluid Theory

We start by reviewing the infinite length drift theory: a plasma of infinite length confined within a conducting, cylindrical wall. We use the guiding-center $\vec{E} \times \vec{B}$ drift model in cylindrical geometry, assuming flute perturbations, as a 2D problem. The dynamics are governed by the

continuity equation for incompressible drift flow, which is a simple advection equation:

$$\frac{\partial n}{\partial t} + \nabla \cdot (\vec{v} n) = \frac{\partial n}{\partial t} + \vec{v} \cdot \nabla n = 0, \tag{3.1}$$

and the drift velocity equation

$$v = \frac{c}{B} \vec{E} \times \hat{z}. \tag{3.2}$$

In cylindrical geometry, after substituting (3.3) into (3.1), we obtain

$$\left\{ \frac{\partial}{\partial t} + \frac{c}{Br} \left(\frac{\partial \phi}{\partial r} \frac{\partial}{\partial \theta} - \frac{\partial \phi}{\partial \theta} \frac{\partial}{\partial r} \right) \right\} n(r, \theta; t) = 0. \tag{3.3}$$

Next, we linearize (3.3), assuming density and potential of the forms

$$n(r, \theta; t) = n_0(r) + \delta n(r) e^{-i\omega t + i\ell\theta} \tag{3.4}$$

$$\phi(r, \theta; t) = \phi_0(r) + \delta\phi(r) e^{-i\omega t + i\ell\theta}, \tag{3.5}$$

where of course Poisson's equation must be satisfied for both the perturbed and unperturbed potentials and densities, respectively. This results in the linearized eigenvalue equation

$$(\omega - \ell \omega_r(r))\, \delta n = -\frac{c\ell}{Br} \frac{\partial n_0}{\partial r} \delta\phi, \tag{3.6}$$

along with Poisson's equation

$$\nabla_\ell^2 \delta\phi = -4\pi q\, \delta n(r). \tag{3.7}$$

where $\omega_r(r) \equiv \frac{c}{Br} \frac{\partial \phi_0}{\partial r}$ is the equilibrium drift rotation frequency. In the next section, we study analytically tractable solutions to Eqs. (3.6) and (3.7).

3.3 Piecewise Constant Density Fluid Theory

One case that can be analytically studied using fluid theory is a piecewise constant, θ-symmetric density plasma, which can be used to approximate an experimental plasma. Such a plasma has an equilibrium profile comprised of uniform density "steps". Here we develop a general, and convenient formalism to compactly determine the diocotron mode frequencies for such a plasma using matrix algebra. Rather than expressing the functional form of the perturbed potential $\delta\phi$ as a function of space, instead we will encode $\delta\phi$ using a two-component vector that is sufficient to specify the two constant coefficients required in each region of constant density. Using the solution to Eq. (3.6) for a uniform region, the solution for the i^{th} uniform region from the center of the plasma is

$$\delta\phi_i = B_i r^\ell + C_i r^\ell. \tag{3.8}$$

To record a dimensionless "state" of the potential in the i^{th} region, we will define the vector ψ_i as follows

$$\psi_i = \begin{pmatrix} \frac{\delta\phi_i(b_i)}{b_i{}^\ell} \\ \frac{\delta\phi_i'(b_i)}{\ell b_i{}^{\ell-1}} \end{pmatrix}, \tag{3.9}$$

Where b_i is the radius of the i^{th} density transition counting from $i = 0$ at the plasma center. Since in the absence of a central charge the potential remains finite at $r = 0$, $C_i = 0$ in the innermost region $i = 0$, so

$$\psi_0 = \begin{pmatrix} 1 \\ 1 \end{pmatrix}. \tag{3.10}$$

Here we define the multiplicative constant $B_1 = 1$ since we are solving a homogeneous problem with vanishing boundary condition at the wall, so any multiple of the solution will still be a solution. Next, we work towards a "propagator" matrix that takes $\psi_i \to \psi_{i+1}$ via left matrix multiplication. First, we determine the linear relationship taking us from the coefficients B_i and C_i to the potentials evaluated on the inner edge of the i^{th} region, which is expressed in Eq. (3.8),

which becomes

$$\begin{pmatrix} \delta\psi_i(r) \\ \delta\psi_i'(r) \end{pmatrix} = \begin{pmatrix} r^{\ell} & r^{-\ell} \\ \ell r^{\ell-1} & -\ell r^{-\ell-1} \end{pmatrix} \begin{pmatrix} B_i \\ C_i \end{pmatrix}. \tag{3.11}$$

This expression is good for any r inside plasma region i. This linear relationship, along with its inverse, shows us how to relate perturbed potentials and their derivatives on the leftmost side of a plasma region to those on the rightmost side of the same region (just inside where the transition occurs). Next, we need a relationship connecting the potentials (and their derivatives) from just inside and just outside the outer radius of the i^{th} region, that is, the jump condition in crossing from the outermost edge of the i^{th} region to the innermost edge of the $i+1^{\text{th}}$ region. By studying the differential equation for a step profile, the appropriate relationship is found to be

$$\begin{pmatrix} {\delta\phi_i}^{+} \\ {\delta\phi_i}'^{+} \end{pmatrix} = \begin{pmatrix} 1 & 0 \\ \frac{-\ell\delta{\omega_p}^2}{b_i\Omega(\omega-\ell\omega_{\mathrm{E}})} & 1 \end{pmatrix} \begin{pmatrix} {\delta\phi_i}^{-} \\ {\delta\phi_i}'^{-} \end{pmatrix}, \tag{3.12}$$

where the $+$ and $-$ symbols indicate which side of the transition the potentials and derivatives are measured. Putting all this together, and converting from the vector with ψ and its derivative to our convenient state variable ψ, we obtain the relationship

$$\psi_{i+1} = P_i\psi_i, \tag{3.13}$$

with

$$P_i \equiv \frac{1}{2}\begin{pmatrix} 1+\beta_i & 1-\beta_i \\ (1-\beta_i)+(1+\beta_i)W_i & (1+\beta_i)+(1-\beta_i)W_i \end{pmatrix}, \tag{3.14}$$

where $\beta = \left(\frac{b_{i+1}}{b_i}\right)^{2\ell}$,$W = \frac{-2\Delta\omega_{\mathrm{D}}}{\omega-\ell\omega_{\mathrm{E}}}$, and $\omega_{\mathrm{D}} = \frac{-2\pi n_0 qc}{B}$, and Δ signifies the change in the quantity from the i^{th} to the $i+1^{\text{th}}$ region. Thus, the statement that the potential vanishes at the conducting

wall can be compactly written as

$$0 = \begin{pmatrix} 1 & 0 \end{pmatrix} \left(\prod_{i=1}^{i_{\max}} P_i \right) \begin{pmatrix} 1 \\ 1 \end{pmatrix}. \tag{3.15}$$

In Eq. (3.15), the order of the matrix product is defined to multiply matrices from right to left. The simplest non-trivial case of this expression that will serve as a starting point for this chapter is an (infinite length) plasma cylinder consisting of two regions, the plasma interior with uniform non-zero density, and the vacuum region outside, surrounded by a conducting wall at radius $r = a$. That is, consider a rectangular electron plasma profile of the form

$$n_0(r) = \begin{cases} n_0, & r \leq R_p \\ 0, & r \geq R_p \end{cases}, \tag{3.16}$$

where the symbol n_0 is used both for the name of the function and the central plasma density. In the innermost plasma region, the inner radius is zero, so $\beta = 0$, and W is determined by the change in the density between the interior and vacuum region. In the vacuum plasma region, the value of W_2 is irrelevant, since the entries in P_2 containing W_2 only appear in the bottom row which is annihilated by the row vector on the left in Eq. (3.15). The result is

$$\left(\frac{R_\mathrm{p}}{R_\mathrm{w}} \right)^{2\ell} = \frac{1}{2W} \implies \omega = \frac{-2\pi n_0 q c}{B} \left(\ell - 1 + \left(\frac{R_\mathrm{p}}{R_\mathrm{w}} \right)^{2\ell} \right). \tag{3.17}$$

The resulting mode frequency for this profile is

$$\omega = \frac{-2\pi q n_0 c}{B} \left(\ell - 1 + \left(\frac{R_\mathrm{p}}{R_\mathrm{w}} \right)^{2\ell} \right), \tag{3.18}$$

Incidentally, in the case $\ell = 1$, only the final term in parentheses survives, and the plasma radius cancels entirely when written in terms of the line density Λ:

$$\omega_{\ell=1} = \frac{-2q\Lambda c}{BR_{\rm w}^2}. \tag{3.19}$$

In fact, the linear $\ell = 1$ mode frequency has no dependence on the radial profile shape at all (even for a non-square profile), thanks to the eigenfunction representing a simple circular translation of the plasma mode. The plasma density perturbation takes the form

$$\delta n(r) = \frac{\eta}{R_p}\delta(r - R_p), \tag{3.20}$$

while the corresponding potential perturbation can be concisely written

$$\delta\phi(r) = \frac{-2e\pi\eta}{\ell}\left[\frac{r_<^\ell\left(r_>^\ell - R_{\rm w}^{2\ell}r_>^{-\ell}\right)}{R_{\rm w}^{2\ell}}\right], \tag{3.21}$$

where $r_> \equiv \max(r, R_{\rm p})$, and $r_< \equiv \min(r, R_{\rm p})$.

3.4 Vlasov Interpretation

$\vec{E} \times \vec{B}$ dynamics generates incompressible flow, so the r-θ plane can be viewed as a plane of phase space. This perspective will become useful when we discuss thermal effects in Diocotron modes. In the drift approximation, the kinematic momentum perpendicular to the magnetic field vanishes, so the only contribution to the Hamiltonian is the axial kinetic energy and the electric potential energy:

$$H = \frac{p_z}{2m} + q\Phi(r, \theta, z). \tag{3.22}$$

The dynamics of this equation are governed by the Vlasov Equation using the Poisson bracket:

$$\frac{\partial f}{\partial t} + \{f, H\} = 0, \tag{3.23}$$

Where f is the distribution function. In this geometry the conjugate variables are (z, p_z) and (θ, p_θ), where $p_\theta = \frac{qBr^2}{2c}$. Writing (3.23) explicitly in terms of polar coordinate variables gives

$$\left[\frac{\partial}{\partial t} + \frac{c}{Br}\left(\frac{\partial \phi}{\partial r}\frac{\partial}{\partial \theta} - \frac{\partial \phi}{\partial \theta}\frac{\partial}{\partial r}\right) + \frac{p_z}{m}\frac{\partial}{\partial z} - q\frac{\partial \phi}{\partial z}\frac{\partial}{\partial p_z}\right] f(r, \theta, z, p_z; t) = 0. \tag{3.24}$$

The last two terms in the bracket disappear in the z-symmetric problem, leaving us with an expression nearly identical to (3.3), except with the distribution function rather than the density. The physical interpretation is that each slice at constant p_z of the z-independent Vlasov description of this problem is identical to the z-independent fluid theory. This will not be the case where the potential and distribution function are also functions of z.

3.5 Description in Action-Angle Variables

We can make further progress by making a canonical transformation of (3.23) to Action-Angle variables $(p_\theta, \bar{\theta}, \psi, J)$ in favor of the old coordinates, and also linearize. First write the equation in linear form, where the zeroth order distribution f_0 is an equilibrium of H_0:

$$0 = \frac{\partial f_0 + \delta f}{\partial t} + \{f_0 + \delta f, H_0 + \delta H\} \xrightarrow{\text{linearize}} 0 = \frac{\partial \delta f}{\partial t} + \{\delta f, H_0\} + \{f_0, \delta H\}. \tag{3.25}$$

The perturbation δH comes entirely from the perturbed electric potential $\delta\phi$ (there is no kinetic perturbation). Therefore we can take $\delta H = q\delta\phi$. Next, we write out this equation explicitly in

terms of the action-angle variables mentioned above:

$$0 = \frac{\partial \delta f}{\partial t} + \frac{\partial \delta f}{\partial \psi} \underbrace{\frac{\partial H_0}{\partial J}}_{\equiv \langle \omega_B \rangle} - \frac{\partial \delta f}{\partial J}\frac{\partial H_0}{\partial \psi} + \frac{\partial \delta f}{\partial \bar{\theta}} \underbrace{\frac{\partial H_0}{\partial p_\theta}}_{\equiv \langle \omega_E \rangle} - \frac{\partial \delta f}{\partial p_\theta}\frac{\partial H_0}{\partial \bar{\theta}} + q\left(\frac{\partial f_0}{\partial \psi}\frac{\partial \delta\phi}{\partial J} - \frac{\partial f_0}{\partial J}\frac{\partial \delta\phi}{\partial \psi} + \frac{\partial f_0}{\partial \bar{\theta}}\frac{\partial \delta\phi}{\partial p_\theta} - \frac{\partial f_0}{\partial p_\theta}\frac{\partial \delta\phi}{\partial \bar{\theta}}\right). \tag{3.26}$$

We define $\frac{\partial H_0}{\partial J} = \langle \omega_E \rangle$, and $\frac{\partial H_0}{\partial J} = \langle \omega_B \rangle$, but the bracket notation used here should be justified, since it suggests that an average is taking place, which needs justification. In fact, the bracket turns out to simply be an average over one full period of the z orbit. To see this, note that the z-period $\tau_z = \oint \frac{dz}{|v_z(p_\theta, z, p_z)|}$ (full period) is constant in time since the z-velocity v_z can be expressed in terms of the conserved total energy, and the z-integral occurs over a full period. This enables us to define ψ so that $z(\psi)$ is periodic with period 2π. Consequently, the bounce period for z and ψ are equal, and it immediately follows that their average bounce frequencies are also equal. A parallel argument follows similarly for $\langle \omega_E \rangle$. This enables the identification used above. Next, we have chosen J and p_θ to be constants of the motion, $\bar{\theta}$ and ψ are cyclic coordinates in the Hamiltonian, so the two terms involving them drop out. Further, since we assume an equilibrium profile for f_0, its derivatives with respect to the generalized positions ψ and $\bar{\theta}$ vanish. This leaves the following more manageable equation:

$$0 = \frac{\partial \delta f}{\partial t} + \langle \omega_B \rangle \frac{\partial \delta f}{\partial \psi} + \langle \omega_E \rangle \frac{\partial \delta f}{\partial \bar{\theta}} - q\left(\frac{\partial f_0}{\partial J}\frac{\partial \delta\phi}{\partial \psi} + \frac{\partial f_0}{\partial p_\theta}\frac{\partial \delta\phi}{\partial \bar{\theta}}\right). \tag{3.27}$$

Because some experiments satisfy $\omega_B \gg \omega_E$, we can simplify considerably by not following the dynamics along ψ, but rather keep only the average δf along orbits. This effectively detaches the ψ-dependence from our problem so that we can focus on the dynamics we are interested in. Also, we are interested in studying perturbations with the standard $\bar{\theta}$ wave dependence going like $e^{i\ell\bar{\theta} - i\omega t}$. To pull out the average component along the bounce trajectories of δf, and also take

into account the azimuthal dependence, we express δf (and $\delta\phi$) as follows:

$$\delta f = \sum_{n=-\infty}^{\infty} \widetilde{\delta f}_n(r) e^{i\ell\bar{\theta}+in\psi-i\omega t},\ \delta\phi = \sum_{n=-\infty}^{\infty} \widetilde{\delta\phi}_n(r) e^{i\ell\bar{\theta}+in\psi-i\omega t}. \tag{3.28}$$

This way, the "bounce-averaged" contribution to a quantity is simply its zeroth Fourier harmonic ($n = 0$). We now write down the Fourier version of (3.27):

$$0 = \left(-i\omega + in\left\langle\omega_B\right\rangle + i\ell\left\langle\omega_E\right\rangle\right)\widetilde{\delta f}_n - q\left(in\frac{\partial f_0}{\partial J} + i\ell\frac{\partial f_0}{\partial p_\theta}\right)\widetilde{\delta\phi}_n. \tag{3.29}$$

Then the Vlasov equation is easily solved, given $\widetilde{\delta\phi}_n$:

$$\widetilde{\delta f}_n = \frac{q\left(in\frac{\partial f_0}{\partial J} + i\ell\frac{\partial f_0}{\partial p_\theta}\right)\widetilde{\delta\phi}_n}{-i\omega + in\left\langle\omega_B\right\rangle + i\ell\left\langle\omega_E\right\rangle}. \tag{3.30}$$

We concern ourselves in this paper where this bounce-averaged term dominates all other terms in the Fourier expansion ($\delta f_0 \gg \delta f_n$ for $n \neq 0$). To this end, we assume that $\delta f = \widetilde{\delta f}_0$, which we refer to as the bounce-average assumption, which gives

$$\delta f = q\frac{i\ell\frac{\partial f_0}{\partial p_\theta}\widetilde{\delta\phi}_0}{-i\omega + i\ell\left\langle\omega_E\right\rangle}. \tag{3.31}$$

This equation can only be solved when either $\delta\phi$ is known, or when we have another equation relating δf to $\delta\phi$. Here we are interested in potential perturbations arising from the electrostatic potential due to the plasma itself. By integrating (3.31) over p_z, we can obtain the perturbed density, which is related to $\delta\phi$ through Poisson's equation. Here we will make another simplification that $\bar{\theta} = \theta$, which physically says that the θ position of the bouncing particle is the same as if it were uniformly drifting at its average angular speed. In actuality, the particle drifts change as they enter the varying end potential, which allows the particle to sample the potential at slightly different θ positions. However, long plasmas ($L \gg \lambda_D$) ensure particles spend relatively little time

in the end potential compared to in the uniform region of the plasma, and for that reason do not appreciably drift away from the "expected" uniform drift position. With the $\bar{\theta} = \theta$ approximation, we obtain the equation

$$\nabla_\ell^2 \delta\phi = 4\pi q^2 \int_{-\infty}^{\infty} \frac{\ell \frac{\partial f_0}{\partial p_\theta} \langle \delta\phi \rangle}{\omega - \ell \langle \omega_E \rangle} \, dp_z. \tag{3.32}$$

Let us take a moment to interpret the form of (3.32). We have eliminated the distribution function perturbation in favor of the electric potential perturbation. This equation can be viewed as a generalization of (the θ transformed) Poisson's equation in r and z, with the modification that the inhomogeneous part is now a non-local operator acting on ϕ. The non-locality enters due to $\langle \delta\phi \rangle$, which is a function of (p'_θ, z', p'_z), representing the average value of ϕ taken along the entire trajectory of a test particle with initial conditions (p'_θ, z', p'_z). This couples the potential at every point to every other point with equal p_θ (since p_θ is a constant of the motion). While this non-local generalization certainly sets it apart from the local form of Poisson's equation, it will be useful to keep this analogy in mind as we solve this equation.

3.6 Solving the Bounce-Averaged Diocotron Problem

The non-locality present in the Bounce-Averaging makes the form of our equation not analytically tractable. In this section, we turn to discretize the problem on a grid in r and z, and work out some difficulties with performing a discrete version of the bounce-average operation. In order to do this, we must unpack the bounce-average operator by expressing it as an integral over space.

The bounce-average operator is a ψ-average, or equivalently, an average through time:

$$\langle a \rangle \equiv \frac{1}{\tau} \oint a \, dt' = \frac{2}{\tau} \int_{z_{\min}}^{z_{\max}} \frac{a}{|v'_z|} \, dz', \tag{3.33}$$

where the bounce period τ is simply given by

$$\tau \equiv \oint dt' = 2\int_{z_{\min}}^{z_{\max}} \frac{dz'}{|v'_z|}. \tag{3.34}$$

In the second identity in the definition of the bounce average and of τ, a change-of-variables from t' to z' is performed, and the factor of 2 appears to count the identical contribution from the particle's return trip. A source of concern is the appearance of the particle velocity v' in the denominator of the integrand, which diverges at the turning points of the particle. However, while the integrand diverges, the integral remains finite, as we expect from an average. However, upon discretizing this integral operator, care must be taken near the turning points where the integrand varies very rapidly and a simple Riemann sum will converge slowly. The solution is to assume the potential ϕ_0 varies linearly between grid points, which immediately implies that E_z, and therefore the z-acceleration, are constant ($a_z = \frac{qE_z}{m}$)between two adjacent grid points. Then the time $\Delta t_{j'}$ spent between two adjacent grid points $z_{j'}$ and $z_{j'+1}$ is given by simple kinematics:

$$\Delta t_{j'} = \frac{m\Delta v_{j'}}{qE_{z\,j'}}, \tag{3.35}$$

where $\Delta v_{j'}$ is the change in velocity of the particle between $z_{j'}$ and $z_{j'+1}$ and $E_{z\,j'}$ is the (assumed uniform) electric field between $z_{j'}$ and $z_{j'+1}$. When the particle reaches a turning point, it does not pass through both adjacent grid points. In this case, exactly one of the final or initial velocities will be zero, where the particle stops and reverses direction. The velocity changes are calculated using conservation of energy:

$$v'(H, r, z') = \sqrt{\frac{2}{m}(H - q\phi(r, z'))}, \tag{3.36}$$

where H is the total energy, and the p_θ dependence has been re-expressed in terms of r, through $p_\theta = \frac{qB}{2c}r^2$. To compute bounce averages of a quantity a, we use $\Delta t_{j'}$ in (3.35) as weights for

the quantity being bounce averaged, as in (3.33). Since the quantities being averaged (ω_E and $\delta\phi$) do not diverge, we assign values to each step in z to be the average of the values of a on the end-points of the grid step. First we express the orbit time in this way, taking advantage of the symmetry of the problem around the center of the trap at z=0, which implies that the time τ is simply four times the time to travel from $z = 0$ to the turning point:

$$\tau = 4 \sum_{j'=0}^{j'_{\max}} \Delta t_{j'}. \tag{3.37}$$

Here $j'_{\max}$ is the index of the grid point with the largest value of z that lies within the particle trajectory, that is, $j'_{\max}$ is the largest integer j' solving

$$v'(H, r, z_{j'}) > 0. \tag{3.38}$$

Next, unpack the definition of $\Delta t_{j'}$, being careful to correctly take care of the contribution at the turning point:

$$\tau = 4 \sum_{j'=0}^{j'_{\max}-1} \frac{m(v_{j'+1} - v_{j'})}{qE_{z\,j'}} + 4\frac{m(0 - v_{j'_{\max}})}{qE_{z\,j'_{\max}}}, \tag{3.39}$$

Where $v_{j'}$ is given by (3.36) evaluated at grid point j'. Now, to compute bounce-averaged quantities $\langle S \rangle$, we simply perform a weighted average of $S_{j'}$, using the $\Delta t_{j'}$ that appear across the sum in (3.39) as weights. Since these weights are times spent between grid points, each $S_{j'}$ should be interpolated to the regions between the grid. Here we interpolate by taking $S_{j'\,\text{interp}} = \frac{S_{j'+1} + S_{j'}}{2}$. This gives the following expression for the bounce average operator:

$$\langle S \rangle = \frac{1}{\tau} \left(4 \sum_{j'=0}^{j'_{\max}-1} \left(\frac{S_{j'+1} + S_{j'}}{2} \right) \frac{m(v_{j'+1} - v_{j'})}{qE_{z\,j'}} - 4 \left(\frac{S_{j'_{\max}+1} + S_{j'_{\max}}}{2} \right) \frac{m v_{j'_{\max}}}{qE_{z\,j'_{\max}}} \right). \tag{3.40}$$

S is some function on r and z. When we calculate its bounce average, we are doing an average of S over the z-dimension, where the weights are determined by the initial radius and energy of the

test particle. Next, we need to discretize the rest of the equation, which can be expressed as a linear operator acting on the perturbed potential:

$$\left\{ \nabla^2{}_{ij}^{i'j'} + 4\pi q^2 \left(\int dv \right)^k \left(\frac{\ell \left(\frac{\partial f_0}{\partial p_\theta} \right)_{ij}}{-\omega + \ell \left\langle \omega_E \right\rangle_{ij}} B_{ij}^{i'j'} \right)_k \right\} \widetilde{\delta\phi}_{i'j'} = 0 \tag{3.41}$$

This is a non-standard eigenvalue equation for ω, where the eigenvalue appears in the denominator of the integrand. To solve this equation, we replace the zero on the right-hand side with $\lambda\widetilde{\delta\phi}_{i'j'}$, which turns it into a regular eigenvalue equation when omega is held fixed. Then we adjust ω until an eigenvalue λ passes through zero, which indicates that (3.41) is satisfied. Numerically, we make an initial guess for ω, then find the smallest norm eigenvalue $\lambda_{\min}(\omega)$, and use a root-finding algorithm to approach the correct value of ω.

One numerical difficulty with this algorithm that considerably slows down progress is that the matrix appearing in Eq. (3.41) is itself a function of ω, and therefore cannot be computed once-and-for-all at the beginning of the calculation. Using our iterative numerical method, new guess values of ω are generated, which requires that the matrix be reevaluated each time with a new value of ω. The evaluation of this matrix can take considerable time. If we had expressed the eigenvalue problem by using δf as our independent variables to be solved for, the system becomes a standard eigenvalue problem for the mode frequency ω, but the price one pays is that the matrix equation grows substantially, since δf is a function of the z momentum p_z as well as the spatial coordinates r and z. As we learned in Chapter 2, using numerical linear algebra routines to solve the Vlasov equation in 3D is painfully slow, and has its own set of difficulties. So for this problem we choose to proceed by performing smaller matrix eigenvalue problems, multiple times, to converge to the correct mode frequency.

3.6.1 Numerics and Convergence

When the theory developed in section 3.5 is solved numerically, one needs to have confidence that a high enough grid resolution was used to obtain convergence. First, even axial parity of the solution was exploited by solving the problem on the half domain, in order to reduce the linear algebra problem size. Second, the rapid falling off factor in the integrand coming from the finite radial extent of the plasma in Eq. (3.41) causes all solution points in this vacuum region to reduce simply to Laplace's equation, as would be physically expected. We can take advantage of this by replacing the form of Eq. (3.41) in these regions with Laplace's equation, meaning that the bounce-averaged quantities and velocity integral can be skipped for these grid points. This considerably speeds up the matrix construction time, and solve time, since there are fewer off-diagonal terms (coming from the non-local bounce-average of $\delta\phi$ along the particle trajectories).

When we solve non-uniform temperature profiles, it also becomes necessary to be more nuanced about the numerical velocity integration. Hot portions of the plasma obviously have broader axial velocity distributions than colder portions, so the grid used to evaluate velocity integrals is chosen to be "stretched" across a larger velocity range. The scheme to determine the maximum kept velocity on this grid is to keep some number of thermal velocities, which will be a function of r in the cases with non-uniform radial profile. We choose to keep the number of velocity grid points per field line fixed, so that the grid spacing is reduced for hotter grid points.

There are two levels of convergence for this numerical solution method. Equation (3.41) is first solved with a guess value for ω, and as described earlier, the smallest eigenvalue λ_{small} of the system is determined. A physical solution to the problem requires λ_{small} be exactly zero, that is, be a root of $\lambda_{\text{small}}(\omega)$. A root-finding algorithm is employed for this purpose, which converges on the correct value of ω. In practice, it was found that $\lambda_{\text{small}}(\omega)$ is nearly linear between any reasonable initial guess (say the infinite-length diocotron mode frequency) and the actual solution. This was fortunate, since using a simple secant method for root-finding converges

rapidly. The second level of convergence is checking that the numerical grid is fine enough that the solution to the discretized equations is an accurate representation of the continuous solution to the physical problem. To determine this, the dimensions of the equilibrium plasma are considered, with attention to the scale lengths associated with the plasma ends and radial edge. Both of these lengths should span many grid points, since these are the finest scale lengths in the problem. Typically $50-100$ radial grid points, and $150-200$ axial grid points were sufficient for convergence. A good starting guess for the number of velocity grid points is the number of grid points needed to correctly estimate the integral of a Maxwellian distribution with the temperature of the plasma to within the error desired in the solution to the physical problem. In practice, this number of grid points was found to be much lower than the number needed for the spatial dimensions (even 10 velocity grid points was found to be enough to obtain converged results). The reason for this appears to be that the velocity dependence of the quantities in the integrand of Eq. (3.41) change gradually, and are therefore well-approximated by even seemingly few grid points. This is in contrast to the problem studied in Chapter 2 where the number of velocity grid points had an unexpected effect on the stability of the problem. For this problem, very small fractional changes on the order of 10^{-3}eV^{-1} are studied, and these small changes required an appropriately high resolution to obtain accurate results. A side effect of this is that a very high accuracy in the absolute frequency is corresponds to an accuracy in the relative frequency change reduced by a factor of 1000. In order to compare this theory to experiment and a second theory to be described in a later section, it is decided that only 5% accuracy in the fractional changes, (or 5×10^{-3} in the absolute frequencies) is required, so the grid resolution is increased until these conditions are met. This was done by calculating the fractional frequency shift, using five different plasma temperature solutions and computing the best fit, and repeating this process for increasing resolutions until convergence is reached.

3.6.2 Results of Bounce Averaged Vlasov Theory

In this section, we study temperature dependence predictions of the bounce averaged Vlasov theory, and for $\ell = 1$, compare to the existing finite-length theory. To make comparison to experimental regimes at UCSD, we use plasma parameters similar to those used in the experiments. Here we study a plasma in axial thermal equilibrium with $N = 1.62 \times 10^9$, $R_p = 1$ cm, $R_{\rm w} = 3.5$ cm, and confinement potential $V_{\rm c} = 100V$, with distance between confinement cylinders $d_{\rm conf} = 38.5$ cm. The external magnetic field used for Fig. 3.4 is $B = 10000$ Gauss.

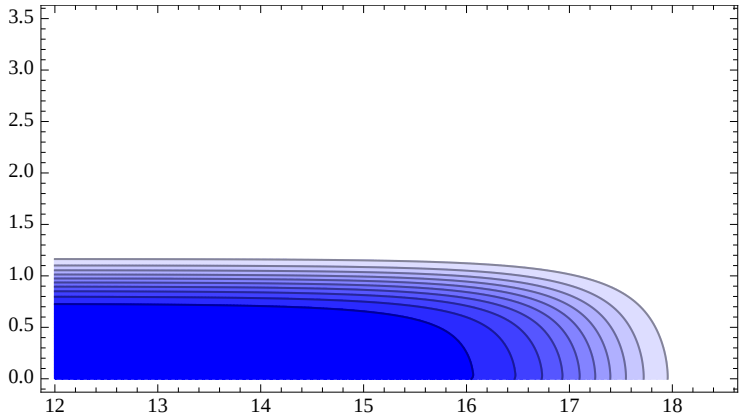

Figure 3.1: A contour plot showing $n_0(r,z)$, with horizontal axis z and vertical axis r, near the right end of the column on a linear scale. For $z < 12$cm, the density loses z-dependence, so can be inferred from the values on the plot at $z = 12$ The central density (darkest blue) is about $n_{\rm cent} = 1.5 \times 10^7 {\rm cm}^{-3}$.

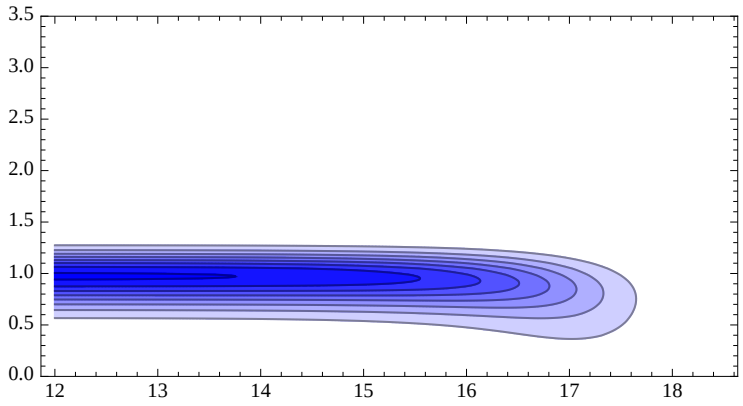

Figure 3.2: A contour plot showing the perturbed plasma density, with horizontal axis z and vertical axis r, on a linear scale, calculated from the bounce-average theory.

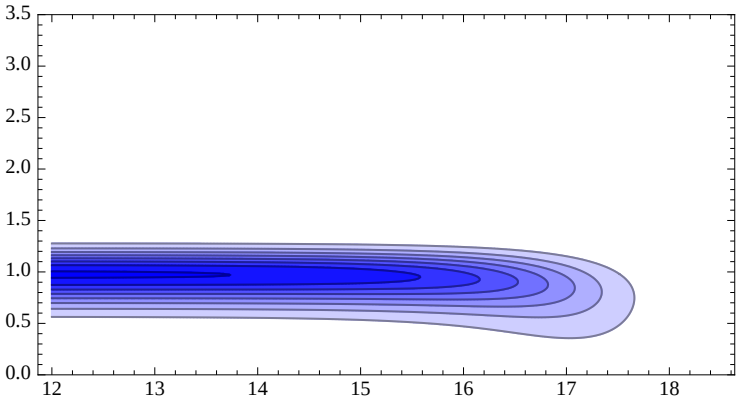

Figure 3.3: A contour plot showing the radial derivative of the equilibrium density, with horizontal axis z and vertical axis r, shown in Fig. 3.1, which is the density eigenmode for an infinite plasma column. Comparing with Fig. 3.2, the two agree better than expected; there appears to be little, or no discernible difference between the solution and radial derivative guess.

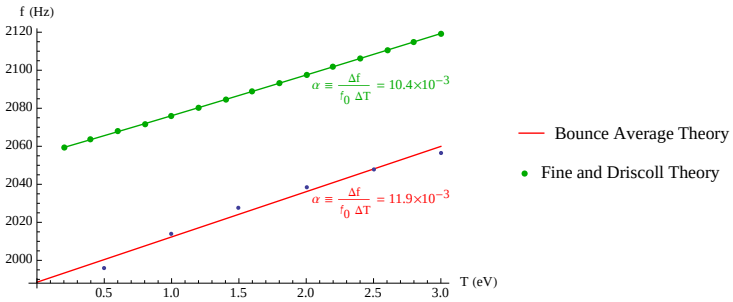

Figure 3.4: Comparison of our Bounce-Average theory to the analytic theory from Fine and Driscoll [7], which we will generalize later a new way later in the paper. Additive shift between data can be attributed to the ambiguity in definition of the "length" of a real plasma with rounded ends.

In Fig. 3.4, The temperature-dependent, computational bounce-averaged problem for $\ell = 1$ is solved using the method described in Section 3.6, and compared to the existing analytic result valid for $\ell = 1$. The vertical axis of the plot is labeled in "experimentalist frequency" $f = 2\pi\omega$, and it is seen that the predictions of the temperature dependence of the mode frequency is correctly predicted to within about four percent. It is important to keep in mind that when comparing the bounce-averaged theory (which solves the Poisson-Vlasov equations for the complete thermal equilibrium density profile) and the existing finite-length analytic theory, the analytic theory uses a somewhat arbitrary choice of "plasma length". We would like to confirm

that the additive "shift" in Fig. 3.4 can be quantitatively attributed to this arbitrariness in plasma length. To zeroth order in b/L, the analytic result simply takes the form of an infinite-length plasma, as in Eq. (3.19), where the line density is replaced via $\Lambda = N/L$:

$$\omega_{\ell=1} = \frac{-2qNc}{BLR_{\mathrm{w}}^2}. \tag{3.42}$$

Since Eq. (3.42) is inversely proportional to L, a small fractional change f in the plasma length corresponds to an opposite fractional change $-f$ in the predicted mode frequency. There is necessarily a somewhat arbitrary choice made when a physical plasma with rounded ends is to be assigned a single, characteristic length to be compared to a uniform cylinder of the same length. There is not an optimal "unique" way to define a single plasma length of a plasma with rounded ends like this; to give a few examples, one could define it as the full length at half maximum of the density on the axis $r = 0$, or as a density-weighted average of the lengths across all radii, or even simply the ratio of the number of particles to the line density of the plasma at $z = 0$. In this paper, we will use the latter as our working definition of plasma length, but we need to recognize that this simplification needs to be taken with a grain of salt. That being said, the absolute frequency predicted by the existing analytic theory should be expected to be accurate to the same fractional error as the fractional ambiguity in the plasma length, which could be about 5%. Being that Eq. (3.42) shows a 3% frequency shift between the bounce-average theory and the Fine and Driscoll theory, we can conclude that the small disagreement in the absolute frequency of the mode can be resolved by making the plasma length L 3% larger, which is completely reasonable. For this reason, this chapter is less interested in computing the absolute frequency prediction to a higher degree of accuracy, but it instead concerns itself with accurate prediction of the mode frequency as a function of temperature (i.e. the slope of the lines appearing in Fig. 3.4), which is considerably harder to measure, as in the regime of interest these frequency changes are on the order of one part in *one thousand* (fractional change) per eV of temperature increase. In the

present example, we find good agreement between the fractional frequency shifts per electron volt for $\ell = 1$. The next question is to examine the frequency dependence for the $\ell = 2$ mode, shown in Fig. 3.5, where this time we focus on the temperature dependence by comparing relative changes in diocotron mode frequency between $T = 0$ and various temperatures ranging up to 3eV. Anticipating the results, the reader might expect qualitative similarity between the $\ell = 1$ and $\ell = 2$ results: likely the temperature dependence factor α will vary somewhat in magnitude between the two azimuthal mode numbers, but nonetheless show a similar increasing trend as temperature increases. Surprisingly, this intuitive guess is completely wrong. In Fig. 3.5, the

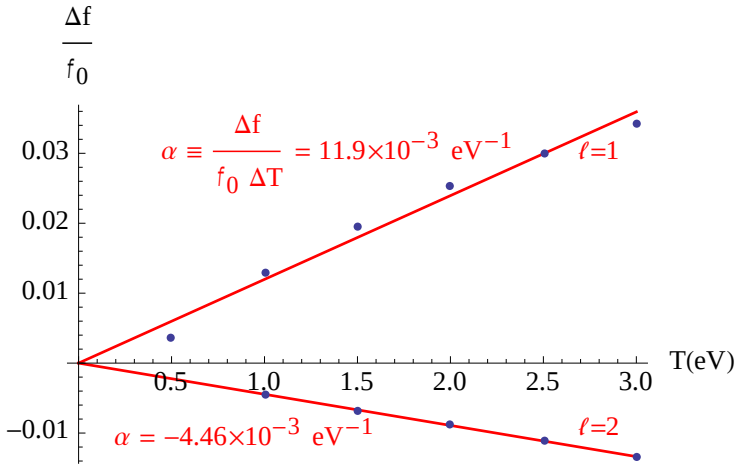

Figure 3.5: The fractional frequency shift away from the zero-temperature result predicted by the Bounce-Average theory for $\ell = 1$ and $\ell = 2$. A spatial Landau resonance appears for $\ell \geq 3$, which introduces numerical difficulty in integrating the discrete equations. Question: "Why are the frequency shifts for $\ell = 1$ and $\ell = 2$ in opposite directions as temperature is increased?"

data show that while the $\ell = 1$ mode frequency is linearly increasing with temperature, the $\ell = 2$ mode frequency actually decreases linearly with temperature! Evidently there is some physical mechanism not yet understood here that is responsible for this frequency shift reversal. Also, we need an analytic expression analogous to the existing $\ell = 1$ result in order to provide an additional check of the bounce-averaged theory. It is the purpose of section 3.10 to explain what physical principle is at work here. But first, we first must develop some formalism and analytic results to reach that point, which will be discussed in the next sections.

3.7 z-integrated Vlasov Theory

To develop a simplified finite-length theory for Diocotron modes, we will begin from the bounce-averaged drift-kinetic theory covered in Section 3.4, integrating out p_z (and as we will see, also z), at fixed p_θ and θ, in order to obtain an effective fluid theory. Starting from (3.31) written without a division, and already imposing the bounce-average assumption ($\delta f = \widetilde{\delta f}_0$), we have

$$-i\omega\delta f + i\ell \langle \omega_E \rangle \delta f = i\ell q \frac{\partial f_0}{\partial p_\theta} \langle \delta\phi \rangle . \tag{3.43}$$

$\langle \cdot \rangle$ signifies the bounce average, or equivalently the Fourier term with $n = 0$. We will call this the "Bounce-Average assumption". As stated, we integrate in p_z in order to make a fluid theory, and also integrate in z for reasons that will become clear later. This gives

$$0 = -i\omega \int dz\, \delta n + i\ell \int dz\, dp_z\, \delta f \langle \omega_E \rangle - i\ell q \int dz\, dp_z \frac{\partial f_0}{\partial p_\theta} \langle \delta\phi \rangle . \tag{3.44}$$

the perturbed density does not appear in (3.44) in the second and third terms, so we would like to cast it into a form that resembles a "z-integrated fluid theory", where δf is entirely absent. To do this, we will transform the integrals in the second and third terms into action-angle coordinates. In general, such a change of coordinates requires a Jacobian determinant. When integration is over all phase space coordinates, we can take advantage of the symplectic structure of canonical transformations; phase space areas are conserved, and the following integral operators are equivalent:

$$\int d\theta\, dp_\theta\, dz\, dp_z \longleftrightarrow \int d\theta\, dp_\theta\, dJ \oint d\psi. \tag{3.45}$$

This is sometimes referred to as Liouville's Theorem: the Jacobian determinant of a canonical transformation is unity. In the problem at hand, we are only integrating over z and p_z, so there is no immediate guarantee that we can use a similar trick to integrate over this sub-surface

of phase-space alone. Instead, we will have to calculate this partial ψ, J Jacobian determinant explicitly to carry out the change of variables:

$$\mathcal{J}_{\psi,J} = \begin{bmatrix} \frac{\partial \psi}{\partial z} & \frac{\partial \psi}{\partial p_z} \\ \frac{\partial J}{\partial z} & \frac{\partial J}{\partial p_z} \end{bmatrix}. \tag{3.46}$$

On the other hand, the Jacobian determinant for the entire canonical transformation equals unity by Liouville's Theorem, but can also be calculated in terms of $\mathcal{J}_{\psi,J}$:

$$1 = |\mathcal{J}| = \begin{vmatrix} \frac{\partial \bar{\theta}}{\partial \theta} & \frac{\partial \bar{\theta}}{\partial p_\theta} & \frac{\partial \bar{\theta}}{\partial z} & \frac{\partial \bar{\theta}}{\partial p_z} \\ \frac{\partial p_\theta}{\partial \theta} & \frac{\partial p_\theta}{\partial p_\theta} & \frac{\partial p_\theta}{\partial z} & \frac{\partial p_\theta}{\partial p_z} \\ \frac{\partial \psi}{\partial \theta} & \frac{\partial \psi}{\partial p_\theta} & \frac{\partial \psi}{\partial z} & \frac{\partial \psi}{\partial p_z} \\ \frac{\partial J}{\partial \theta} & \frac{\partial J}{\partial p_\theta} & \frac{\partial J}{\partial z} & \frac{\partial J}{\partial p_z} \end{vmatrix} = \begin{vmatrix} 1 & \frac{\partial \bar{\theta}}{\partial p_\theta} & \frac{\partial \bar{\theta}}{\partial z} & \frac{\partial \bar{\theta}}{\partial p_z} \\ 0 & 1 & 0 & 0 \\ 0 & \frac{\partial \psi}{\partial p_\theta} & \frac{\partial \psi}{\partial z} & \frac{\partial \psi}{\partial p_z} \\ 0 & \frac{\partial J}{\partial p_\theta} & \frac{\partial J}{\partial z} & \frac{\partial J}{\partial p_z} \end{vmatrix} \tag{3.47}$$

The first column follows from the θ-symmetry of the unperturbed Hamiltonian allows that the new canonical coordinates do not depend on θ, except for $\bar{\theta} = \theta + \delta\theta(p_\theta, z, p_z)$. The second row follows from the fact that p_θ appears in both the old and new coordinates, so p_θ is independent from all of the old variables except p_θ itself.

By performing the determinant by expansion by minors along the first column, we can reduce this expression simply to the determinant of the lower right 3×3 matrix. Then, expanding this 3×3 matrix around its first row, we can further reduce this expression to the determinant of the bottom right 2×2 matrix, which is simply $\left|\mathcal{J}_{\psi,J}\right|$. Then we have

$$\left|\mathcal{J}_{\psi,J}\right| = |\mathcal{J}| = 1. \tag{3.48}$$

The conclusion is the following operators are equal:

$$\int dz\, dp_z = \int dJ \oint d\psi, \tag{3.49}$$

that is, we can perform the same sort of integral manipulation as we did for the full phase space in (3.45) (this time with only z, p_z), provided we are making the assumption that $\theta = \bar{\theta}$. We can now return to (3.44) and make further progress.

$$0 = -i\omega \int dz\, \delta n + i\ell \int dJ \oint d\psi\, \delta f \langle \omega_E \rangle - i\ell q \int dJ \oint d\psi\, \frac{\partial f_0}{\partial p_\theta} \langle \delta\phi \rangle . \tag{3.50}$$

Next, notice that the quantity multiplying the bounce-averages in both of the second two terms has no ψ-dependence (from the Bounce-Average Assumption and the fact that f_0 is an equilibrium). Then the bounce average brackets can be extended to include these ψ-independent terms, which then makes the bounce average redundant since we immediately integrate in ψ afterwards. Thus the bounce-averages can be removed, at which point we can use (3.49) again in reverse to restore the original integration measure involving z and p_z variables. Now that we have eliminated all bounce-averages from the equation, the only p_z-dependent quantities are f_0 and δf, allowing us to perform the p_z integrals, changing these distribution functions into densities. Converting to radius from p_θ, the result is

$$\omega \int \delta n(r,z)\, dz = \frac{c\ell}{Br} \left(\int \frac{\partial \phi_0(r,z)}{\partial r} \delta n\, dz - \int \frac{\partial n_0(r,z)}{\partial r} \delta\phi\, dz \right). \tag{3.51}$$

We have now succeeded in obtaining an effective fluid-theory from the bounce-averaged kinetic theory. It is useful to note that (3.51) is identical to the infinite-length fluid theory in (3.6), with the only distinctions being that (3.51) integrates over z, and allows z-dependence in the densities and potentials. This simplification reduces the dimension of phase space by one; $(r,z,p_z) \to (r,z)$, making analysis significantly more tractable. The caveat is that we have integrated out z from (3.51), so this fluid theory cannot predict the z-dependence of the perturbation on its own. Luckily, it is often true (for all cases studied in this paper) that the z-dependence of the mode is quite predictable, with the perturbed density remaining z-independent on the plasma interior and falling off within a few Debye lengths at the end. This can be verified by solving the full bounce-averaged

Vlasov theory, (3.32), numerically, and verifying the spatial dependence of the perturbed density. In light of this, the mode can be estimated by an ansatz: for instance, take the perturbed density of the plasma to match infinite-length theory inside the z-range of the plasma, and zero outside. Another example is to assume the plasma is always in thermal equilibrium along each magnetic field line as the mode evolves in time. As it happens, taking even the cruder of these two approximations does a good job of predicting results in experiments at UCSD.

3.8 Net Force Analysis and Generalizations

Before solving Eq. (3.51), we discuss its connection to an alternative approach to the $\ell = 1$ diocotron mode by relating the mode frequency of the plasma to the net electrostatic force exerted on the column[7]. We will call this approach the "Net Force Analysis". Afterwards, we will see how Eq. (3.51) is an equivalent description for linear $\ell = 1$ modes. Equation (3.51) is equivalent to the z-integrated, linearized fluid theory, so the non-perturbative form of Eq. (3.51) is the same as integrating Eq. (3.1) over all z. To make connection to the Net Force Analysis, we will integrate Eq. (3.1) over the entire volume within the trap walls with a moment $r^\ell e^{-i\ell\theta}$.

$$\int r^\ell e^{-i\ell\theta} \frac{\partial n}{\partial t}\, dV + \int r^\ell e^{-i\ell\theta} \nabla \cdot (n\vec{v})\, dV = 0. \tag{3.52}$$

For small amplitude waves, the full density in the first term is composed of the equilibrium density (which integrates to zero with the complex exponential term in the theta integral), plus the perturbed density, which we will still assume is small enough to have $e^{i\ell\theta - i\omega t}$ dependence, so we can still use the replacement $\frac{\partial n}{\partial t} \to -i\omega n$. In the second term, we integrate by parts, allowing the spatial derivative to act on the $r^\ell e^{-i\ell\theta}$ factor:

$$-i\omega \int n r^\ell e^{-i\ell\theta}\, dV = \int n\vec{v} \cdot \nabla \left(r^\ell e^{-i\ell\theta} \right) dV. \tag{3.53}$$

Table 3.1: $\vec{s}(x,y)$ and $p(x,y)$ for various ℓ.

	$\vec{s}(x,y)$	$p(x,y)$
$\ell = 1$	$\vec{x}$	1
$\ell = 2$	$2(\vec{x}-\vec{y})$	x^2-y^2
$\ell = 3$	$3(x^2-y^2)\hat{x}-6xy\hat{y}$	x^3-3xy^2

Using the fact that $i\nabla\left(r^\ell e^{-i\ell\theta}\right) = \hat{z}\times\nabla\left(r^\ell e^{-i\ell\theta}\right)$, we can write

$$\omega\int nr^\ell e^{-i\ell\theta}\,dV + \int n\,(\vec{v}\times\hat{z})\cdot\nabla\left(r^\ell e^{-i\ell\theta}\right)\,dV, \tag{3.54}$$

where the vector operators have been modified using a scalar triple product identity. Finally, using the definition of the drift velocity from Eq. (3.3), we can write the mode frequency as

$$\omega = \frac{\frac{-c}{B}\int n\vec{E}\cdot\nabla\left(r^\ell e^{-i\ell\theta}\right)\,dV}{\int nr^\ell e^{-i\ell\theta}\,dV} \tag{3.55}$$

A similar equation follows for a real-valued perturbation (cosine perturbation) when ω is real, when we can simply take the real part of the numerator and denominator of Eq. (3.55), giving

$$\omega = \frac{-\frac{c}{B}\int n\vec{E}\cdot\vec{s}(x,y)\,dV}{\int np(x,y)\,dV}, \tag{3.56}$$

where $p(x,y) = r^\ell\cos\ell\theta$, and $\vec{s}(x,y) = \nabla\left(p(x,y)\right)$, with examples for various ℓ shown in 3.1.

There are two advantages to this formulation. First, it is computationally convenient because neither the perturbed nor the unperturbed densities and electric fields are needed to calculate the mode frequency; only the total quantities n and $\vec{E}$ are required. Secondly, using Eq. (3.56) in the case of $\ell = 1$ provides the intuitive Net Force Result as expected:

$$\omega_{\ell=1} = \frac{-\frac{c}{B}\int nE_x\,dV}{\int nx\,dV}, \tag{3.57}$$

which simply states that the mode frequency obtained by applying the net force on the column

via the $\vec{F} \times \vec{B}$ drift expression to a rod at a position of the x-center-of-mass is consistent with Eq. (3.51).

3.9 Solving the Effective Fluid Theory

To obtain an analytic formula for the diocotron mode frequency as a function of the parameters of our plasma, we will consider a radius b, length L, uniform-density equilibrium plasma excited with the following arbitrary ℓ diocotron surface mode:

$$n_0(r,z) = n_0 \Theta(R_\mathrm{p} - r)\Theta\left(\frac{L}{2} - |z|\right), \tag{3.58}$$

$$\delta n(r,z) = \frac{\eta}{R_\mathrm{p}} \delta(r - R_\mathrm{p})\Theta\left(\frac{L}{2} - |z|\right). \tag{3.59}$$

This is a cylindrical plasma with flat ends and top-hat profile, with a surface perturbation existing only on the radial edge. Substituting into (3.51) and simplifying shows that every term is proportional to $\delta(r-b)$, which can be factored out of the entire equation. Solving for ω gives

$$\omega = \frac{c\ell}{BL}\left(\frac{1}{b}\int_{-L/2}^{L/2} \left.\frac{\partial \phi_0}{\partial r}\right|_{r=b} dz + n_0 \int_{-L/2}^{L/2} \left.\frac{\delta\phi}{\eta}\right|_{r=b} dz\right). \tag{3.60}$$

Now all that remains is determining the equilibrium and perturbed potential from Poisson's equation. The potentials are then resolved into separate contributions: an infinite-length portion, minus the left and right semi-infinite ends that are not present in a finite-length plasma. The equilibrium potential also has a contribution from the confinement potential used to trap the plasma:

$$\frac{\partial \phi_0}{\partial r} = \frac{\partial {\phi_0}^\infty}{\partial r} - \frac{\partial {\phi_0}^\leftarrow}{\partial r} - \frac{\partial {\phi_0}^\rightarrow}{\partial r} + \frac{\partial {\phi_0}^\mathrm{C}}{\partial r}, \tag{3.61}$$

$$\delta\phi = \delta\phi^\infty - \delta\phi^\leftarrow - \delta\phi^\rightarrow. \tag{3.62}$$

The infinite-length electric quantities are found by using Gauss's law for ϕ_0^∞, and the 2D Green's function for $\delta\phi^\infty$:

$$\left.\frac{\partial {\phi_0}^\infty}{\partial r}\right|_{r=R_\mathrm{p}} = -2\pi q n_0 R_\mathrm{p}, \tag{3.63}$$

and

$$\delta\phi^\infty|_{r=R_\mathrm{p}} = \frac{4\pi\eta q}{2\ell}\left(1-\left(\frac{R_\mathrm{p}}{R_\mathrm{w}}\right)^{2\ell}\right). \tag{3.64}$$

When these expressions are substituted into (3.60), the left and right portions of the equilibrium and perturbed contributions ($\delta\phi^{\leftrightarrows}$ and $\phi_0{}^{\leftrightarrows}$) are equal by symmetry. Also, since the missing potentials drop off quickly at the ends, integral limits involving these quantities can be extended to infinity when $L \gg a$, and z can be redefined so $z = -L/2$ becomes $z = 0$ for mathematical convenience (that is, shifting the origin to the left end of the plasma). $\phi_0^{\leftarrow}(r,z)$ and $\delta\phi^{\leftarrow}(r,z)$ will be understood to accept this new shifted z from this point forward. The result is

$$\begin{aligned}\omega = \omega_\infty + \ell\tilde{\omega}_2^\infty \frac{R_\mathrm{p}}{L}\Bigg(&\underbrace{\frac{1}{\pi R_\mathrm{p}^2}\int_0^\infty \frac{1}{n_0 q}\left.\frac{\partial\phi_0^{\leftarrow}}{\partial r}\right|_{r=R_\mathrm{p}} dz}_{\text{(A)}} + \underbrace{\frac{1}{\pi R_\mathrm{p}}\int_0^\infty \left.\frac{\delta\phi^{\leftarrow}}{\eta q}\right|_{r=R_\mathrm{p}} dz}_{\text{(B)}} \\ &+ \underbrace{\frac{-1}{\pi R_\mathrm{p}^2}\int_0^{L/2}\left.\frac{\partial\phi_0^\mathrm{C}}{\partial r}\right|_{r=R_\mathrm{p}} dz'}_{\text{(C)}}\Bigg),\end{aligned} \tag{3.65}$$

Where $\omega'_\infty = \frac{-2\pi q n_0 c}{B}$ is the infinite-length $\ell = 2$ mode frequency in the absence of a conducting wall ($a \gg b$), and z' is the original z-coordinate with $z = 0$ at the plasma center. Eq. (3.65) determines the finite length diocotron frequency in terms of three frequency shifts away from the infinite-length theory, namely (A), (B), (C). The first two come from the finite length of the plasma providing weaker total fields near the plasma end compared to the infinite plasma, while

the last shift is due to the external confinement potentials that were not present for an infinite plasma.

We will evaluate these three bracketed integrals in Eq. (3.65) individually to aid in organization. First, we will calculate the final confinement term (C), and afterwards we will calculate the first and second integrals appearing in (3.65) by writing out the Green's functions in our cylindrical geometry and integrating over the appropriate charge distribution.

3.9.1 Confinement Term

The confinement term (C) depends strongly on the location of the end of the plasma, since the radial electric confinement field $E_r^{\mathrm{C}} = -\frac{\partial \phi_0^{\mathrm{C}}}{\partial r}$ (to lowest order) grows exponentially. However, in previous work[7] for $\ell = 1$, a shortcut was used to determine the force along the direction of the diocotron offset (call it x) due to the confinement potential that circumvents the need for the plasma length. In brief summary, the $\ell = 1$ argument in the existing literature shows that the net confinement x-force on the plasma is directly related to the net confinement z-force on the right half of the equilibrium plasma. Since this confinement force must balance the thermal and electrostatic forces being exerted between the left and right halves, the conclusion is that the confinement x-force can be determined without knowing the plasma length, but instead knowing the plasma temperature. We will show that there is a generalization of this shortcut that works for arbitrary ℓ, where we instead consider a integral involving the *radial* component of the confinement electric field.

The confinement term (C) appearing in (3.65) can be rewritten in the following way:

$$\text{(C)} = \frac{-1}{\pi R_{\mathrm{p}}^2} \int_0^{L/2} \int_0^{R_{\mathrm{w}}} r\, dr \frac{\partial \phi_0^{\mathrm{C}}}{\partial r} \delta(r - R_{\mathrm{p}}) dz', \tag{3.66}$$

where a integral over r with a delta function has been introduced to produce the evaluation at $r = R_{\mathrm{p}}$, and divided by R_{p} at the expense of multiplying by r. By integrating this expression by

parts over r, and then again multiplying and dividing by $2\pi r$ to restore the $2\pi r\,dr$ measure, the integral can be written to resemble the radial term appearing in Laplace's equation, giving

$$\textcircled{C} = \frac{1}{2\pi^2 R_{\rm p}^3 n_0 q}\int_0^{L/2}\int_0^{R_{\rm w}} 2\pi r\,dr\frac{1}{r}\frac{\partial}{\partial r}\left[r\frac{\partial \phi_0^{\rm C}}{\partial r}\right] q n_0 \Theta(R_{\rm p}-r)dz'. \tag{3.67}$$

Notice that $n_0(r,z) = n_0\Theta(R_{\rm p}-r)$ inside the z-integration. Using Laplace's equation, which is satisfied by the confinement potential, we can replace the radial portion of the Laplacian with $\frac{\partial}{\partial z}E^{\rm C}$. Finally, using the fact that the electric field grows exponentially at the ends, with

$$E_z{}^{\rm C} \approx Ae^{\frac{j_{01}}{R_{\rm w}}}, \tag{3.68}$$

$$\frac{\partial E_z{}^{\rm C}}{\partial z} \approx \frac{j_{01}}{R_{\rm w}} E_z{}^{\rm C} \tag{3.69}$$

on the right half of the plasma, we can write the entire expression in terms of a volume integral involving the z-electric field:

$$\textcircled{C} = \frac{-{\rm j}_{01}}{2\pi^2 R_{\rm p}^3 n_0{}^2 q^2 R_{\rm w}}\int dV\, qE(r,z)n_0(r,z) = \frac{-{\rm j}_{01}}{2\pi^2 R_{\rm p}^3 n_0{}^2 q^2 R_{\rm w}} F_{z{\rm C}}, \tag{3.70}$$

where $F_{z{\rm C}}$ is the confinement force on the right half of the plasma. Now we are in a position to make use of the fact that clearly there is no net force on the right half of the equilibrium plasma column, or equilvalently, that the forces exerted from the left half of the plasma on the right half must cancel F_zC. This force acting between the two plasma halves is the sum of the electrostatic repulsion force, and the thermal pressure force acting across the cross-section of the plasma at $z = 0$. That is,

$$F_{\text{electric from left}} + F_{\text{thermal}} = -F_{z{\rm C}}. \tag{3.71}$$

The lefthand side of this equation has already been evaluated in the paper studying finite $\ell = 1$

diocotron modes[7] in the case of a top-hat cylindrical plasma; the result is

$$\textcircled{C} = \frac{\mathrm{j}_{01} R_\mathrm{p}}{2R_\mathrm{w}} \left(\frac{T}{\pi R_\mathrm{p}^2 n_0 q^2} + \frac{1}{4} + \log \frac{R_\mathrm{w}}{R_\mathrm{p}} \right). \tag{3.72}$$

This shows that Eq. (3.72) predicts a thermal correction to the mode frequency.

3.9.2 Green's Function Terms

The Green's function we will use here is

$$G(\vec{x},\vec{x}') = \frac{2}{\pi} \int_0^\infty dk \cos k(z-z') \times \left[\sum_{m=-\infty}^{\infty} \mathrm{I}_m(kr_<)\mathrm{K}_m(kr_>) - \frac{\mathrm{K}_m(kR_\mathrm{w})}{\mathrm{I}_m(kR_\mathrm{w})} \mathrm{I}_m(kr_<)\mathrm{I}_m(kr_>) \right] e^{-im(\theta-\theta')}. \tag{3.73}$$

During integration of the Green's function, orthogonality picks out only the appropriate m term ($m = \ell$ for the perturbed potential, and $m = 0$ for the unperturbed potential). Then it is convenient to define a reduced Green's function $G_m(r,r';z-z')$ for a density perturbation with an implied $e^{im\theta}$ dependence that satisfies ${\nabla_m}^2 G_m(r,r';z-z') = -\frac{4\pi}{r'}\delta(r-r')$, with $e^{im\theta}$ dependence implied on both sides:

$$G_m(r,r';z-z') = 4 \int_0^\infty dk \cos k(z-z') \times \left[\mathrm{I}_m(kr_<)\mathrm{K}_m(kr_>) - \frac{\mathrm{K}_m(kR_\mathrm{w})}{\mathrm{I}_m(kR_\mathrm{w})} \mathrm{I}_m(kr_<)\mathrm{I}_m(kr_>) \right]. \tag{3.74}$$

The potentials are found by evaluating

$$\phi_m(r,z) = \int r' dr' dz' n_m(r,z) G_m(r,r';z-z'). \tag{3.75}$$

Equation (3.75) will be used to compute both the perturbed and unperturbed potential.

We will begin with the perturbed potential evaluated at $r = b$, to work towards the

evaluation of (B). We obtain

$$\delta\phi^{\leftarrow}|_{r=R_{\rm p}} = 4\eta q \int_0^\infty dk \left[\int_{-\infty}^0 \cos k(z-z')dz'\right] \times \left[\mathrm{I}_\ell(kR_{\rm p})\mathrm{K}_\ell(kR_{\rm p}) - \frac{\mathrm{K}_\ell(kR_{\rm w})}{\mathrm{I}_\ell(kR_{\rm w})}\mathrm{I}_\ell(kR_{\rm p})^2\right]. \tag{3.76}$$

Notice that the integral in square brackets can be written as $\int_{-\infty}^0 \cos k(z-z')dz' = \pi\delta(k) - \frac{\sin kz}{k}$, allowing the answer to be separated into a z-independent and z-dependent part (See Appendix C). After making suitable variable substitutions, and performing the integral over z as a limiting process as $Z \to \infty$, we find

$$\begin{aligned}\text{(B)} = \frac{1}{\pi R_{\rm p}}\int_0^\infty \frac{\delta\phi^{\leftarrow}}{\eta q}dz = \frac{-Z}{R_{\rm p}\ell}\left(1-\left(\frac{R_{\rm p}}{R_{\rm w}}\right)^{2\ell}\right) - \frac{4}{\pi R_{\rm p}}\int_0^\infty dk\,\frac{1-\cos(kZ)}{k^2} \\ \times\left[\mathrm{I}_\ell\left(kR_{\rm p}\right)\mathrm{K}_\ell\left(kR_{\rm p}\right) - \frac{\mathrm{K}_\ell(kR_{\rm w})}{\mathrm{I}_\ell(kR_{\rm w})}\mathrm{I}_\ell\left(kR_{\rm p}\right)^2\right].\end{aligned} \tag{3.77}$$

A similar process happens for the integral involving the equilibrium potential. The potential is again evaluated at $r = b$, but since now we have an integral over r' with $r' \le b$, we can safely take $r_< = r'$ and $r_> = R_{\rm p}$. After computing this integral, taking the derivative in r, and integrating in z from 0 to ∞, we get

$$\frac{1}{\pi R_{\rm p}^2}\int_0^\infty \frac{\phi_0^{\leftarrow}}{n_0 q}dz = \frac{-Z}{R_{\rm p}} - \frac{4}{\pi R_{\rm p}}\int_0^\infty dk\,\frac{1-\cos(kZ)}{k^2} \times \left[-\mathrm{I}_1\left(kR_{\rm p}\right)\mathrm{K}_1\left(kR_{\rm p}\right) - \frac{\mathrm{K}_0(kR_{\rm w})}{\mathrm{I}_0(kR_{\rm w})}\mathrm{I}_1\left(kR_{\rm p}\right)^2\right]. \tag{3.78}$$

Notice that since we are calculating the unperturbed integral, this expression now involves Bessel functions of index 0 and 1, rather than index ℓ. Also, notice the minus sign in the first Bessel function in Eq. (3.78), which was not present in Eq. (3.77). Next we will perform two variable substitutions: $v = kR_{\rm p}$ for the first terms, which we call "non-image" terms due to their origin in the Green's function; and $u = kR_{\rm w}$ for the second terms, which we similarly call "image" terms, in order to enable an expansion to lowest order in $R_{\rm p}/R_{\rm w}$ for the sum (A)+(B), which appears

in Eq. (3.65). At this point, we arrive at a fork in the road depending on whether $\ell = 1$ or $\ell > 1$. For $\ell > 1$, the image terms in (3.77) and (3.78) are subdominant in $R_\mathrm{p}/R_\mathrm{w}$, so the first terms dominate. However, when $\ell = 1$, these first two terms precisely cancel between (A) and (B), so that the lowest order contribution instead comes from the second terms in each expression. This cancelation for $\ell = 1$ is an algebraic validation that the plasma exerts no net force on itself, as was argued on physical grounds in Fine and Driscoll's paper[7]. Consequently, the process to solve for the mode frequency for $\ell = 1$ differs from that of $\ell > 1$, so we will now consider these two cases separately in the following sections.

3.9.3 Case for $\ell = 1$

Substituting Eqs. (3.77), (3.78) into Eq. (3.65) for $\ell = 1$, we see that the two terms arising from the non-image potentials precisely cancel (the first Starting from Eqs. (3.78) and (3.77), we calculate (A)+(B) to first order in $R_\mathrm{p}/R_\mathrm{w}$. We find

$$\text{(A)}+\text{(B)} = \left(\frac{R_\mathrm{p}}{R_\mathrm{w}}\right)\left(\frac{1}{\pi}\int_0^\infty \frac{\mathrm{K}_0(u)}{\mathrm{I}_0(u)} + \big(1-\cos(Z''u)\big)\,\frac{\mathrm{K}_1(u)}{\mathrm{I}_1(u)}\,du + -Z''\right), \tag{3.79}$$

where Z'' is another limiting variable with $Z'' \to \infty$. In the limit, both Z'' and the order 1 Bessel function integral both diverge, but their divergences cancel with each other in the process. The limit as $Z'' \to \infty$ is a bit cumbersome, so it is useful to remove it by converting it into another similar divergent integral with the same value:

$$Z'' = \frac{-2}{\pi}\int_0^\infty \frac{1-\cos(Z''u)}{u^2}, \tag{3.80}$$

Allowing us to combine all terms into a single proper integral:

$$-\mathbb{M}_1\frac{b}{a} \equiv \frac{R_\mathrm{p}}{R_\mathrm{w}}\frac{1}{\pi}\int_0^\infty \frac{-2}{u^2} + \frac{\mathrm{K}_1(u)}{\mathrm{I}_1(u)} + \frac{\mathrm{K}_0(u)}{\mathrm{I}_0(u)} \approx -0.671479\frac{R_\mathrm{p}}{R_\mathrm{w}}. \tag{3.81}$$

The reader may recognize the numerical value $\mathbb{M}_1$ from Eq. (3.81) as the same number appearing in reference [7]. The existing derivation for $\ell = 1$ started from a finite, zero radius line charge of plasma displaced a small distance from the origin, so the displacement is greater than the plasma radius, and consequently this is not a linear density perturbation. Here we have shown here that the same result holds to leading order for a plasma of finite radius shifted off-axis by linear perturbation theory. Of course, if desired the finite radius corrections can be included by using the original form of (A) and (B) in Eq. (3.77) without expanding in $R_\mathrm{p}/R_\mathrm{w}$. Gathering the contributions from (A), (B), (C), and inserting into Eq. (3.65), we obtain an equivalent result from reference [7]:

$$\frac{\omega}{\omega_\infty} = 1 + \left[\frac{\mathrm{j}_{01}}{2}\left(\frac{1}{4} + \log\frac{R_\mathrm{w}}{R_\mathrm{p}} + \frac{T}{\Lambda q^2}\right) - \mathbb{M}_1\right]\frac{R_\mathrm{w}}{L}, \tag{3.82}$$

$$\mathbb{M}_1 \equiv \frac{1}{\pi}\int_0^\infty \frac{-2}{u^2} + \frac{\mathrm{K}_1(u)}{\mathrm{I}_1(u)} + \frac{\mathrm{K}_0(u)}{\mathrm{I}_0(u)} = 0.671479\ldots \tag{3.83}$$

In this expression, $\Lambda = n0\pi R_\mathrm{p}^2$ is the line density of the plasma.

3.9.4 Case for $\ell > 1$

The important terms for $\ell > 1$ are opposite to the result found in section 3.9.3. This time, the dominant terms in (3.77) and (3.78) are the ones that previously canceled entirely for $\ell = 1$: the *non-image* terms. The image field contribution now enters at higher order in b/a than the bulk field contribution, and will be ignored for simplicity in this analysis. Again, finite-radius corrections can be included by using the full forms of (A) and (B) in Eqs. (3.78) and (3.77) rather than expanding in $R_\mathrm{p}/R_\mathrm{w}$. The calculation for (A) is a bit more involved as discussed earlier because there is no radial delta function in the equilibrium density. This time, we instead perform the substitution $v = kb$, keeping only the non-image term. The result is

$$(\mathrm{B}) = \frac{2}{\ell\pi}\left(Z' - \int dv \frac{1-\cos(Z'v)}{v^2}\left[2\ell \mathrm{I}_\ell(v)\mathrm{K}_\ell(v)\right]\right). \tag{3.84}$$

Again, Z' can be transformed into an integral using a similar expression to Eq. (3.80). The final result, for all $\ell > 1$, is fortunately integrable in terms of elementary functions:

$$\text{(B)} = \frac{2}{\ell\pi}\int_0^\infty \frac{1-2\ell \mathrm{I}_\ell(v)\mathrm{K}_\ell(v)}{v^2} = \frac{8}{\pi(4\ell^2-1)}. \tag{3.85}$$

(A) is almost identical the result in Eq. (3.85), except negated, and with $\ell \to 1$.

$$\text{(B)} = -\frac{2}{\ell\pi}\int_0^\infty \frac{1-2(1)\mathrm{I}_1(v)\mathrm{K}_1(v)}{v^2} = \frac{-8}{3\pi}. \tag{3.86}$$

Then the sum (A)+(B) is given by

$$\mathbb{N}_\ell \equiv \text{(A)} + \text{(B)} = \frac{32}{3\pi}\frac{\ell^2-1}{4\ell^2-1}. \tag{3.87}$$

Now we can write the equation for the mode frequency for $\ell > 1$ by again combining (A), (B), (C):

$$\frac{\omega}{\omega_\infty} = 1 + \frac{\ell}{\ell-1}\left[\frac{\mathrm{j}_{01}}{2}\frac{R_\mathrm{p}}{R_\mathrm{w}}\left(\frac{1}{4} + \log\frac{R_\mathrm{w}}{R_\mathrm{p}} + \frac{T}{\Lambda q^2}\right) - \mathbb{N}_\ell\right]\frac{R_\mathrm{p}}{L}, \tag{3.88}$$

$$\mathbb{N}_\ell \equiv \frac{32}{3\pi}\frac{\ell^2-1}{4\ell^2-1}. \tag{3.89}$$

There are some changes between Eq. (3.88) and Eq. (3.82). First, the numerical quantity has changed from $\mathbb{M}_1$ to $\mathbb{N}_\ell$. Second, there is a factor of $\frac{\ell}{\ell-1}$ in front of all of the correction terms. Third, the first term in square brackets now has a new factor of $R_\mathrm{p}/R_\mathrm{w}$, and finally, the correction for $\ell > 1$ is of order R_p/L, not R_w/L as for $\ell = 1$. This final fact is a consequence of the correction for $\ell = 1$ coming from the image field, while for higher ℓ, the non-image field dominates.

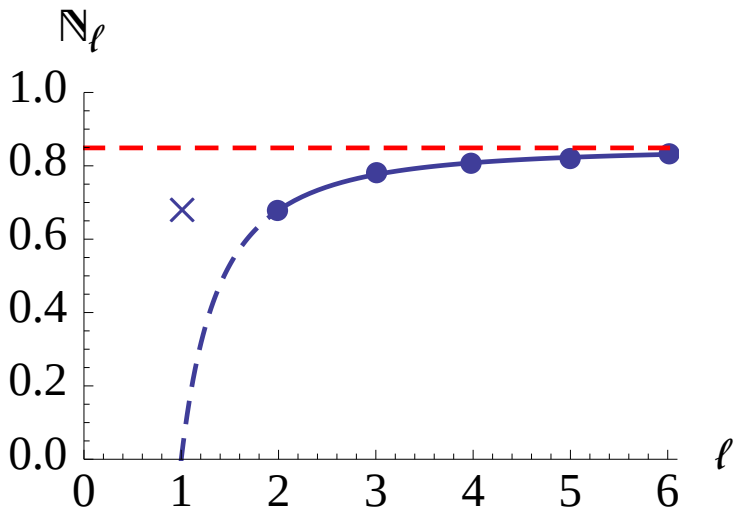

Figure 3.6: Graphical depiction of $\mathbb{N}_\ell = \frac{32}{3\pi}\frac{\ell^2-1}{4\ell^2-1}$ ($\mathbb{M}_1$ shown with a cross) for various values of ℓ. For large values of ℓ, $\mathbb{N}_\ell \to \frac{8}{3\pi}$ (shown by the red, dashed line). The dashed blue line extends the curve to $\ell = 1$ to illustrate the vanishing of net non-image forces of the $\ell = 1$ plasma on itself.

3.10 Temperature effect on Frequency

In this section, we discuss the details of the predictions given by Eqs. (3.82) and (3.88). In discussing the equations, a subtlety emerges that must be addressed carefully in order to obtain the correct answer. The diocotron problem we are discussing has several physical parameters that define the plasma, and they are not all independent quantities. For instance, the line density, is defined as $\Lambda = N/L$, so the three quantities Λ, N, and L cannot be chosen independently. Consequently, we first need to clearly define what quantities are being held fixed as the temperature is varied. For the present analysis, we study the case that is carried out in the experiments, in which a plasma is injected into the trap with some known number of particles N, which remains constant throughout the experiment (assuming particle loss is negligible). Due to the guiding center drift approximation, p_θ, or equivalently r, is a constant of the motion of the unperturbed Hamiltonian, so the z-integrated equilibrium density $\sigma(r)$ is also effectively constant over the experiment time. In actuality, the plasma does expand gradually over time, but this evolution occurs on a much longer time scale than the diocotron period, so it is not of interest here.

We can now precisely define which quantities should be held fixed as T changes. That is, we wish to calculate the frequency shift of the plasma brought about by a uniform temperature change while holding $\sigma(r)$–or equivalently, plasma radius and N for a top-hat profile–fixed. As the temperature of the plasma increases, its length also increases, due to the increased thermal velocity driving particles deeper into the confinement potentials on either end of the trap. Consequently, the relationship $\Lambda = N/L$ implies that Λ (and similarly, n_0) must decrease as plasma temperature increases. Since both of these quantities appear in Eqs. (3.82) and (3.88), it is not sufficient to simply vary T, since the equilibrium is a function of T, and therefore so is L and Λ. While the thermal equilibrium density is not analytically tractable, as with the bounce-averaged theory it can be solved numerically by solving the Poisson-Boltzmann equations. However, it would be advantageous to obtain frequency dependence on temperature results without having to solve for a new equilibrium at each temperature. To do this, we can linearize $\Lambda(T)$ for small T by introducing a length coefficient λ:

$$\Lambda(T) = \Lambda(0)(1 - \lambda T), \tag{3.90}$$

Or equivalently in terms of length defined as $L = N/\Lambda$ (for small T):

$$L(T) = L(0)(1 + \lambda T). \tag{3.91}$$

λ can be determined experimentally, with numerics, or analytically as we will soon see. Notice that λ, being a quantity that describes the equilibrium plasma, has no dependence on ℓ. To reduce Eqs. (3.82) and (3.88) into a single "algebraic blueprint" that describes both, write the following:

$$\omega(T) = \omega_\infty(T)(1 + h\varepsilon(T) + \mu T), \tag{3.92}$$

where $\varepsilon(T) \equiv R_w/L(T)$ is a small quantity that depends on T through $L(T)$, and h and μ are

coefficients determined from Eqs. (3.82) and (3.88). Throughout this chapter, we will often refer to the frequency correction coming entirely from μ as the *magnetron shift*, since this effect is due to the azimuthal "kick" given to the particles as they approach the confinement rings. We will refer to λ as the *lengthening shift*, since this factor arises simply because a longer plasma in the absence of a magnetron shift (with equal particle number) has a lower mode frequency since the central density is reduced in the lengthening process. Since $\omega_\infty(T)$, the infinite-length diocotron frequency for a plasma with the same line density, changes as a function of T, it is useful to replace $\omega_\infty(T)$ to make its temperature dependence manifest. The infinite-length frequency in Eq. (3.18) is directly proportional to n_0, which is itself proportional to Λ. Using this fact along with Eq. (3.90), we can obtain an analogous expression for the infinite-length temperature dependence:

$$\omega_\infty(T) = \omega_\infty(0)(1-\lambda T). \tag{3.93}$$

Combining Eqs. (3.93) and (3.92), we obtain an expression for the temperature dependence of the diocotron mode frequency in terms of the infinite-length, zero temperature frequency:

$$\omega(T) = \omega_\infty(0)(1-\lambda T)(1+h\varepsilon(T)+\mu T). \tag{3.94}$$

Eq. (3.94) will prove to be a useful result in the next paragraph to understand how T affects the mode frequency.

Now we are in a position to expand Eq. (3.94) to determine an expression for the fractional frequency change as a function of temperature by defining the frequency dependence in terms of a thermal coefficient α:

$$\alpha \equiv \left.\frac{\partial\omega}{\partial T}\right|_{T=0} / \omega(0). \tag{3.95}$$

The quantity α is what we will use to make comparisons of the frequency dependence on plasma

temperature throughout the remainder of this chapter. Evaluating Eq. (3.95) gives the result

$$\alpha = \frac{\mu - \lambda - 2h\varepsilon\lambda}{1 + h\varepsilon} \approx (\mu - \lambda) - h\varepsilon(\mu + \lambda). \tag{3.96}$$

We organize Eq. (3.96) as a term involving the difference of μ and λ, and another term of order ε involving their sum. We keep the order ε term because in the case where μ and λ are approximately equal, the difference term can be much smaller than the sum term, even for small ε. For $\ell = 1$, we read off the parameters appearing in Eq. (3.92) from Eq. (3.82):

$$h_1 = \frac{\mathrm{j}_{01}}{2}\left(\frac{1}{4} + \log\frac{R_\mathrm{w}}{R_\mathrm{p}}\right) - \mathbb{M}_1, \tag{3.97}$$

and

$$\mu_1 = \frac{\mathrm{j}_{01} R_\mathrm{w}}{2q^2 N}. \tag{3.98}$$

We will see how to compute the remaining quantity λ shortly. For $\ell > 1$, we have

$$h_{\ell>1} = \frac{\ell}{\ell - 1}\frac{\mathrm{j}_{01}}{2}\frac{R_\mathrm{p}^2}{R_\mathrm{w}^2}\left(\frac{1}{4} + \log\frac{R_\mathrm{w}}{R_\mathrm{p}}\right) - \frac{R_\mathrm{p}}{R_\mathrm{w}}\mathbb{N}_{\ell>1}, \tag{3.99}$$

and

$$\mu_{\ell>1} = \frac{\ell}{\ell - 1}\frac{R_\mathrm{p}^2}{R_\mathrm{w}^2}\mu_1. \tag{3.100}$$

The remaining quantity, λ, will be computed in the next paragraph.

To obtain a closed theory to predict the frequency dependence, we need a way to predict λ from theory, rather than using a number determined experimentally. Since the equilibrium plasma internal pressure balances the confinement force on the ends, λ can be evaluated by considering a small change in T, with the constraint that the pressure and confinement forces remain in balance [7], that is,

$$F_\mathrm{press} = \Lambda T + \Lambda^2 q^2 (\frac{1}{4} + \log\frac{R_\mathrm{w}}{R_\mathrm{p}}) = F_\mathrm{zC}. \tag{3.101}$$

This expression arises from an equilibrium consideration, and consequently holds for all ℓ. The first term on the right-hand side of Eq. (3.101) is the thermal pressure, and the second term is the electrostatic pressure, which comes from integrating the Maxwell Stress Tensor over the surface of the semi-infinite cylinder, extending to the wall, enclosing one half of an infinitely long plasma. Assuming a plasma with flat ends, the confinement force on the half of the plasma with $z > 0$ can be computed with a simple integral over the linear force density:

$$F_{z\mathrm{C}} = \int_0^{L/2} Cn_0 \exp\left(\frac{\mathrm{j}_{01} z}{R_\mathrm{w}}\right) = -\frac{Cn_0 R_\mathrm{w}}{\mathrm{j}_{01}}\left(1 - \exp\left(\frac{\mathrm{j}_{01} L}{2R_\mathrm{w}}\right)\right), \tag{3.102}$$

Where the unity term is negligible compared to the exponential term, for a moderately long plasma. As the plasma lengthens, its density is transformed via

$$\frac{-\Delta\Lambda}{\Lambda} = \frac{-\Delta n}{n} = \frac{\Delta L}{L} = \lambda \Delta T, \tag{3.103}$$

due to the relationship $\Lambda = N/L$, with N held constant. The linearized form for the confinement force is then

$$\Delta F_{z\mathrm{C}} = F_{z\mathrm{C}}\left(\frac{\mathrm{j}_{01} L}{2a} - 1\right)\frac{\Delta L}{L}. \tag{3.104}$$

The first term comes from the extra electrostatic energy required to produce a longer column with the same density, and the second term adds the correction that the density has actually reduced slightly as the plasma has lengthened. Similarly, the linear expansion of Eq. (3.104) around $T = 0$:

$$\Delta F_\mathrm{press} = \Lambda \Delta T + 2q^2 \Lambda\, \Delta\Lambda \left(\frac{1}{4} + \log\frac{a}{b}\right). \tag{3.105}$$

Setting Eqs. (3.105) and (3.105) equal gives a theoretical prediction for λ:

$$\lambda = \frac{2\Lambda R_\mathrm{w}}{(\mathrm{j}_{01} L + 2R_\mathrm{a})\,\Lambda^2 q^2 \left(\frac{1}{4} + \log\frac{R_\mathrm{w}}{R_\mathrm{p}}\right)}. \tag{3.106}$$

This expression for λ now allows us to calculate the frequency change coefficient α directly from analytic theory.

Some time should be spent discussing the previous results in order to acquire a physical understanding of the equations. Notice that Eq. (3.106) does not depend on ℓ, unlike Eq. (3.100), where μ does depend on ℓ. Also notice that the form of $\mu_{\ell>1}$ is considerably different from μ_1. One change is the factor of $\ell/(\ell-1)$, which introduces a new factor of 2 between the $\ell=1$ result and the $\ell=2$ result. The second change is that we see that μ is suppressed from the $\ell=1$ result by a factor of R_p^2/R_w^2. This result is less surprising when considering that the $\ell=1$ and $\ell=2$ infinite-length mode frequencies to lowest order in R_p/R_w, given in Eq. (3.18) differ by a factor b^2/a^2. This means that an equal absolute magnetron shift for $\ell=1$ and $\ell=2$ produces a *fractional* change in mode frequency (as characterized by μ) that is much larger for $\ell=1$ than for $\ell=2$, since the $\ell=1$ mode frequency is so much lower than the $\ell=2$ mode frequency. On the other hand, the lengthening shift correction affects the mode frequency *multiplicatively* (as can be seen by Eq. (3.93)), and thus shifts the mode frequencies for all ℓ by the same fractional factor. Consequently, for $\ell>2$, μ is typically much smaller than λ, so the frequency shift is often well approximated merely by accounting for the shift predicted by infinite-length theory due to changes in the central density from lengthening alone. This phenomenon is particularly apparent when the wall radius is much smaller than the wall radius, although this effect is even noticeable (but less pronounced) for plasmas with $R_p/R_w \approx 3$, as are typically seen in the experiments in the experimental portion of our group at UCSD.

3.11 Comparisons to Experiment

Now that we have developed a simple theory for arbitrary ℓ diocotron modes, we can compare to experiment. In the lab, a single plasma is excited with modes $\ell=1,2,3$ at very low temperature. After the mode frequencies are measured, the plasma temperature is increased by

Table 3.2: Comparison of $\alpha(\times 10^{-3}\text{eV}^{-1})$ between the z-integrated (cylindrical plasma) theory and the Bounce-Averaged Vlasov Theory, using the plasma from Fig. 3.5.

	$\ell = 1$	$\ell = 2$
Bounce-Average	11.9	-4.46
z-integrated	7.30	-5.30

Table 3.3: Comparison of Diocotron Mode thermal frequency coefficient $\alpha(\times 10^{-3}\text{eV}^{-1})$ to a specific experiment with $R_p = 1.2\text{cm}$, $R_p = 3.5\text{cm}$, $N = 2 \times 10^9$, $L = 34\text{cm}$.

	$\ell = 1$	$\ell = 2$	$\ell = 3$
Experiment	4.05	-3.80	-4.29
z-integrated theory	5.52	-3.52	-4.36

1eV, and the mode frequencies are recorded. The following shows a plot of the experimental results for $\ell = 1$ and $\ell = 2$.

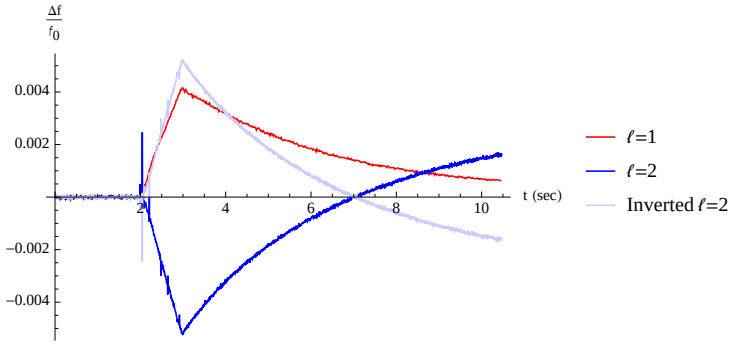

Figure 3.7: Experimental results of Andrey Kabantsev show mode frequency of $\ell = 1$ and $\ell = 2$ have opposite temperature trends. In light blue the $\ell = 2$ plot has been inverted to compare magnitude directly with $\ell = 1$.

There is good agreement between the z-averaged Vlasov theory and the experiment, as detailed in Tab. 3.3, especially for $\ell = 2$ and $\ell = 3$. Comparing to Fig. 3.5, we see the same behavior where the $\ell = 1$ mode increases, while the $\ell = 2$ mode decreases as temperature increases. The magnitude of the results are different between these two cases because the parameters of the plasma are a bit different, most notably where N is larger by 25%, which has the effect of reducing the mode frequencies for all ℓ, since both λ and μ are inversely proportional to N. This is the reason the plots in Fig. 3.5 have greater temperature dependence; the total number of

particles is different for these two cases. Using the theory to compare directly to Fig. 3.5 thus also gives good agreement: Notice that Tab. 3.2 shows that the z-integrated theory overestimates the Bounce-Average result both for $\ell = 1$ and $\ell = 2$. This appears to be due to the approximations in solving for λ analytically. We obtained λ in Eq. (3.106) using a force balance by assuming that the plasma is an ideal cylinder with N held constant with a variable length. In fact, the equilibrium shape of the plasma is quite complex; the ends of the plasma both change shape and axial density profile as a function of temperature.

Comparing the theoretical λ with a value numerically computed using a Poisson-Boltzmann solver, it turns out that the analytically-predicted λ can overestimate the numerical value. This appears to be due to the fact that when T increases, the plasma length increases, but the Debye fall-off at the plasma ends becomes broader, which has the effect of decreasing the density just inside the nominal plasma end, and increasing just outside this end. The effect is that the confinement restoring force is larger than the cylindrical model predicts, which is consistent with the result that the results produce smaller results than the cylindrical theory for λ, since the same plasma temperature change, which generates a pressure change, is more readily counteracted by the confinement potentials with a smaller requisite plasma length change. The z-integrated theory uses λ calculated from a cylindrical plasma assumption. Consequently, these z-integrated theories for $\ell = 1$ and $\ell = 2$ would overestimate λ, resulting in an underestimate in $\alpha \approx \mu - \lambda$ for both values of ℓ, consistent with Tab. 3.2.

3.12 Radial Temperature Dependence

So far we have considered the diocotron mode dependence on the uniformly applied temperature. How is the answer affected when the temperature is non-uniform? As we saw in previous sections, thermal effects in the diocotron mode can come from two sources: first, from a change to the infinite-length mode frequency (a bulk effect, e.g. the plasma density

changing as the plasma expands); and second, from finite-length effects (an end-effect). First, let us consider how radial temperature profile affects the infinite length diocotron mode frequency, restricting our analysis to $\ell = 1$ for simplicity. Since the infinite-length $\ell = 1$ mode frequency depends only on the line density Λ, it suffices to study how Λ (at $z = 0$) is affected by the radial temperature profile. Λ is an equilibrium quantity, so the following analysis is conducted using a Poisson-Boltzmann solver to study the radial temperature dependence. For a given z-integrated profile $\sigma(r) = \int n_0(r,z)dz$ (considered as pre-determined), the line density is a *functional* $\Lambda[T(r)]$ mapping the temperature profile $T(r)$ to the resulting line density Λ. Since there is an infinite set of possible "test" temperature profiles $T(r)$, it is not practically possible to enumerate all of them. Instead, we can linearize the functional $\Lambda[T(r)]$ around a uniform, low-temperature profile (which we will take to be $T_0(r) = 0$ as was implicitly done in the previous section) with the functional derivative:

$$\frac{d}{d\varepsilon}\Lambda[\varepsilon T(r)]\bigg|_{\varepsilon=0} = \int_0^a \frac{\delta\Lambda}{\delta T} T\, dr, \tag{3.107}$$

where $T(r) = \Delta T(r)$ is the absolute temperature, and also the change in temperature, since we chose to expand around $T_0(r) = 0$. By writing $T(r) = \int T(s)\delta(r-s)\, ds$, and interchanging the order of integration, we have

$$\frac{d}{d\varepsilon}\Lambda[\varepsilon T(r)]\bigg|_{\varepsilon=0} = \int_0^a \left(\int_0^a \frac{\delta\Lambda}{\delta T}\delta(r-s)\, dr \right) T(s)\, ds. \tag{3.108}$$

The portion of the integrand in parentheses is simply the total derivative where the delta function $\delta(r-s)$ is used as the test function. So we can write the previous equation as

$$\Delta\Lambda[T(r)] \approx \frac{d}{d\varepsilon}\Lambda[\varepsilon T(r)]\bigg|_{\varepsilon=0} = \int_0^a \frac{d}{d\varepsilon}\Lambda[\varepsilon\delta(r-s)]\bigg|_{\varepsilon=0} T(s)\, ds. \tag{3.109}$$

The advantage of Eq. (3.109) is that it is an expression for $\Delta\Lambda[T(r)] = \Lambda[T(r)] - \Lambda[T_0(r)]$, with any $T(r)$, where using Dirac Delta temperature profiles, since they formally serve as a basis for

the space of small temperature profile functions around $T(r) = 0$ (or whatever temperature profile was used as the base of the expansion). Knowing only the derivative term which multiplies $T(s)$ is sufficient to evaluate an arbitrary $\Lambda[T(r)]$. This derivative is a useful quantity, so we will give it a special notation:

$$\left.\frac{\delta\Lambda[T(r)]}{\delta T(s)}\right|_{(T(r)=0)} = \left.\frac{d}{d\varepsilon}\Lambda[\varepsilon\delta(r-s)]\right|_{\varepsilon=0}. \tag{3.110}$$

We will refer to this equation as "the (functional) partial derivative of Λ at $r = s$. Physically, this quantity encodes how sensitive the line density Λ is to changes at temperature at radius $r = s$, holding all temperatures elsewhere fixed (this motivates the term "partial"). The explicitly notated evaluation of $T(r) = 0$ will usually be dropped, since evaluations always occur at $T_0(r) = 0$. It is important to briefly consider the units of the functional derivative in Eq. (3.110). Since the product of $\varepsilon\delta(r-s)$ must have units of temperature, epsilon has units of eVcm. Consequently, the derivative has units of $[\Lambda] \cdot \mathrm{eV}^{-1}\mathrm{cm}^{-1}$, which has a factor of cm^{-1} that the reader may deem unexpected based on treating it like a regular (non-functional) derivative. The left-hand side of Eq. (3.109) is simply the $O(\varepsilon\Delta T(r))$ term in a Taylor expansion of $\Lambda[T(r)]$. Then the line density for any temperature profile near $T_0(r)$ (with the same $\sigma(r)$) is computed by

$$\Lambda[T(r)] = \Lambda[T_0(r)] + \int_0^a \frac{\delta\Lambda[T(r)]}{\delta T(s)}(T(s) - T_0(s))\, ds, \tag{3.111}$$

Where we have reinserted an arbitrary $T_0(r)$, for generality. Eq. (3.111) takes a generally non-linear functional $\Lambda[T(r)]$, and linearizes it about a particular temperature profile $T_0(r)$ (often chosen to be identically zero, as previously stated).

Numerically, instead of using true delta functions in Eq. (3.109), we will use their numeric approximations: rectangular pulse functions, then approximate the partial derivative of Λ at $r = s$ in Eq. (3.109) by evaluating the finite difference

$$\left.\frac{d}{d\varepsilon}\Lambda[T_0(r) + \varepsilon\delta(r-s)]\right|_{\varepsilon=0} = \lim_{\varepsilon\to 0}\frac{\Lambda\left[T_0 + \varepsilon\bar{\delta}(r-s)\right] - \Lambda[T_0]}{\varepsilon}. \tag{3.112}$$

To put it simply, the right-hand side is evaluated simply as the difference in the line-density with and without a nascent delta function "bump" (denoted $\bar{\delta}$) at $r = s$. Then to determine the line density for a given $T(r)$, one uses Eq. (3.111) along with the numerically determined form of the partial derivative. As a numerical aside, $T_0(r) = 1\text{eV}$, (rather than $T_0(r) = 0\text{eV}$) since evaluating equilibria for zero temperature plasmas makes the Debye length vanish, thus making the ends of the plasma harder to resolve numerically on a grid. This will not make any difference to our results provided that $T_0(r) = 1\text{eV}$ remains within the region where linear approximation around $T_0(r) = 0$ is justified. Eqs. (3.111) and (3.110) are very useful, as they can also be used to calculate functionals other than $\Lambda[T(r)]$, for example, $\mu[T(r)]$, or $\omega[T(r)]$. As before, the partial functional derivative implicitly depends on the plasma profiles $\sigma(r)$, so The behavior of Fig. 3.8

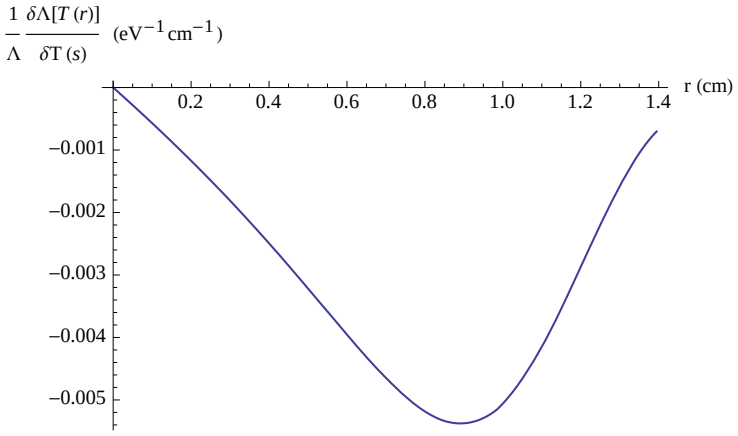

Figure 3.8: The (logarithmic) partial functional derivative of the line density functional $\Lambda[T(r)]$ with respect to the temperature profile. Here a plasma with line density $\Lambda = 4.91 \times 10^7 \text{eV}^{-1}4$, with a very gradual density profile of the form $n(r) \sim \exp\left(-r^4/(1\text{cm})^4\right)$.

can be understood as follows: the line density functional is roughly a function of only the total thermal energy. At both large and small radius, there are few particles to heat; at large radius at the edge of the plasma, the density drops off, and at small radius, geometry dictates that the number of particles near that radius is also small, which mirrors the result shown in Fig. 3.8. We could equivalently express this same data by plotting the functional derivative with respect to the radial energy density, which may be more convenient for some purposes. For our purposes

now, we wish to study the effect of the change in Λ while a deposition of heat spreads outward via radial thermal conduction. To simplify analysis, suppose that the temperature profile remains rectangular, with total thermal energy held fixed (as is approximately true in the experiments, neglecting cyclotron cooling). That is, consider the rectangular thermal profile with radius R:

$$\Delta T(r) = 1\text{eV}\frac{\int_0^b 2\pi r' n(r')\,dr'}{\int_0^R 2\pi r' n(r')\,dr'}\Theta(R-r), \tag{3.113}$$

where Θ is the Heaviside step function. The normalization factor is chosen to make the thermal energy in the plasma equal to the thermal energy in a uniform 1eV plasma with the same density profile, which ensures that if the plasma were to thermally equilibrate radially, it would be a uniform 1eV plasma. Now we can use Eq. (3.109), along with Eq. (3.113) to study how the line density varies as thermal energy diffuses radially. In Fig. 3.9, we plot the change in line density as the thermal skirt grows, while keeping the thermal energy constant. Clearly, $\Lambda(R)$ is rather

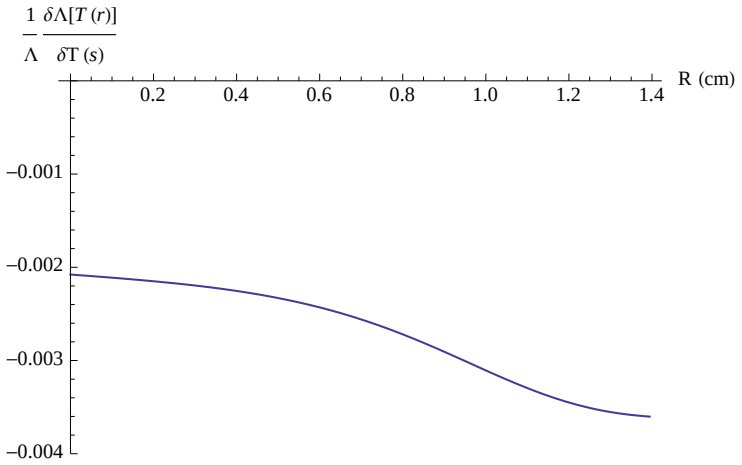

Figure 3.9: This figure shows the fractional change in Λ, for a rectangular thermal profile of radius R, holding the total thermal energy fixed. The right side of the plot asymptotes to a uniform temperature plasma of 1eV.

flat where the plasma is uniform, and decreases once the plasma density begins to fall off. This example was calculated for a density profile $n(r) \sim \exp\left(-r^4/(1\text{cm})^4\right)$, which is a broad profile compared to those observed in experiments. Consequently, a more rectangular profile, with a

broader uniform region and a narrower edge would be even more uniform in the central region, and reduce by a lesser amount in the edge. This analysis shows that the infinite-length mode frequency used in Eqs. (3.88) and (3.82) is reduced by 0.1% when heat is redistributed from near the center to uniformly distributed throughout, while the overall quantity (compared to before any heat was added at all) is reduced by 0.35%. This demonstrates that the infinite-length correction (coming from plasma lengthening with temperature) is only a third of the correction from adding the temperature uniformly. This analysis contributes a small decrease in mode frequency as thermal energy spreads radially.

To introduce radial temperature dependence into our theory, we make relevant changes to Secs. 3.9 and 3.10 to allow radial dependence. For this analysis, we will restrict ourselves to the simpler case where $\ell = 1$, and we will drop the corrections involving $\mathbb{M}_1$, since we found that these terms drop out to lowest order in the frequency change. Then the generalization of the theory of Eq. (3.96) is obtained simply by replacing appearances of λT and μT in Eq. (3.96) with *linear functionals* $\overline{\lambda}[T(r)]$ and $\overline{\mu}[T(r)]$. Then the frequency change parameter $\overline{\alpha}$, which is now itself a functional, takes the form (to zeroth order in $h\varepsilon$)

$$\overline{\alpha}[T(r)] = -\overline{\lambda}[T(r)] + \overline{\mu}[T(r)]. \tag{3.114}$$

To restore the mode frequency from this calculation, we simply use the definition of $\overline{\alpha}[T(r)]$ to calculate $\omega[T_0(r)]$:

$$\omega[T] = \omega[0]\left(1 + \overline{\alpha}[T(r)]\right). \tag{3.115}$$

where, $T(r)\delta r$ is the again, T_0 is usually taken to be a constant initial temperature profile, often chosen to be identically zero. In fact, we have already calculated $\overline{\lambda}[T(r)]$ numerically; it is the negative of the function plotted in Fig. 3.8, using the delta function as the test function (this can

be seen by carrying out the functional version of Eq. (3.90)). Thus, we use the definition

$$\overline{\lambda}[T_0(r)] = \frac{-1}{\Lambda[T(r)=0]} \int_0^a \left.\frac{\delta\Lambda}{\delta T(s)}\right|_{T=0} T(s)\, ds. \tag{3.116}$$

Our previous treatment of (the scalar quantity) λ is a special case of this equation, where $T(r) \to T$ (a constant function). In that case, ΔT can be pulled outside the integral, and $\overline{\lambda}[T] = \lambda T$ (the functional dependence becomes a simple product). The resulting compatibility requirement from Eq. (3.116) for λ and μ, to ensure consistency between the radial-dependent theory and the non-radial dependent theory is simply

$$\overline{\lambda}[T] = \lambda T, \tag{3.117}$$

$$\overline{\mu}[T] = \mu T. \tag{3.118}$$

The units in these equations may still seem strange, since Eqs. (3.117) appear to indicate that λ and μ, compared to their barred, functional counterparts, have different units. This actually depends on the interpretation of Eqs. (3.117). If the units are associated with the evaluation of the functionals (by substituting a particular $T(r)$), then it is true that they are unitless while λ and μ had units eV^{-1}. If the units are instead associated with the functionals *before* evaluation (i.e. as an operator not yet acting on T(r)), then there is perfect agreement between the barred and unbarred variants. It is the latter of these two interpretations that will be used in this chapter.

Next, we want to study $\overline{\mu}[T(r)]$. With this change, we need to revise the analysis of Sec. 3.9, because introducing a piecewise constant thermal profile spoils our assumption that the equilibrium density is constant (since the plasma will expand and contract non-uniformly in r). Luckily, the analysis is readily revised to allow for a non-uniform plasma density. Studying Eq. (3.51), we can see that the evaluation of the radial electric field at the plasma radius comes from δn being a delta function centered at $r = b$. This came from assuming that the mode was a simple surface shift to the plasma column. We will make the same assumption here for $\ell = 1$, and

assume $\delta n(r) = -\eta \frac{\partial n_0}{\partial r}$. The trick to handle this situation is to integrate both sides of r times Eq. (3.82) over the cross-sectional area. Then, as before, we can integrate by parts as in Sec. 3.9.1 and observe that the result can again be written in terms of the total confinement z-force on the right half of the column, and takes the same form as before. As before, this force is balanced by the electrostatic and thermal forces originating from the axial center of the plasma. However, these forces will not be the same as those calculated with a uniform temperature profile, because a temperature gradient introduced into a uniform radial density profile will introduce radial dependence into the density. In order to properly account for the radial temperature dependence, this calculation has to be carried out in more detail, which we will do next.

First, we will see how the thermal pressure term changes. The total thermal force between the two halves of the cylinder is simply the integrated pressure:

$$F_{\text{therm}} = \int n(r)T(r)\, dA, \tag{3.119}$$

which is proportional to the total thermal energy in the plasma. We wish to compare to the experiments which introduce thermal energy into the center of the plasma, and allow it to gradually conduct to the outside of the plasma (or vice versa) *while keeping the total thermal energy fixed*. Then the thermal force in Eq. (3.119) remains constant during this process, and therefore has no contribution to the mode frequency. The second way to have radial temperature dependence on the axial pressure is through the total electrostatic force between the two halves of the cylinder. As before, this is found by integrating the Stress Tensor:

$$F_{\text{elec}} = \frac{1}{8\pi} \int E^2\, dA, \tag{3.120}$$

where $E = \frac{2q\Lambda_{\text{enc}}}{r}$ via Gauss's Law, for example. For simplicity, and in order to estimate whether this effect is significant, we use the piecewise constant model where $n(r) = n_0$ when $r < r_0$, and $n(r) = n_1$ when $r_0 \leq r < r_1$, and zero otherwise. This non-uniform profile is a result of the

non-uniform radial temperature profile having the effect of perturbing the density. We define $\Delta n \equiv n_0 - n_1$, and $n_\mathrm{f} = \frac{A_0 n_0 + A_1 n_1}{A_1 + A_2}$, where A_0 and A_1 are the cross-sectional areas of the central circle of radius r_0, and the annulus with inner radius r_0 and outer radius r_1. That is, n_f is the area-weighted average density, which we can think of as an estimate for the final thermal equilibrium density profile, assuming that the line density remains constant during radial thermal equilibration. After some algebra, F_elec can be written

$$F_\mathrm{elec} = q^2\Lambda^2 \left(\left(\frac{1}{4} + \log \frac{R_\mathrm{w}}{R_\mathrm{p}} \right) + \frac{A_0 A_1}{2(A_0 + A_1)^2} \frac{\Delta n}{n_\mathrm{f}} \right). \tag{3.121}$$

Notice that the first term is identical (after dividing by $q^2\Lambda^2$) to h_1 (see Eq. (3.97)) found for the uniform profile. This is no surprise, since the algebraic origin of h_1 comes directly from F_elec. so the remaining term offers a correction to h_1 due to the non-uniform profile. With this result, we can estimate the importance of this correction term in comparison to the experiments. The term $\Delta n/n_\mathrm{f} \sim O(\Delta L/L) \approx 10^{-3}$ for a 1eV temperature change. Assuming, for example, that the area of the annulus and central disk are comparable, the factor involving the ratio of areas in Eq. (3.121) is $1/8$, reducing the second term down by another order of magnitude. The zeroth order term in Eq. (3.121) is typically $O(1)$. Then h_1 changes by about 1 part in 10^4. Once taking into account that the appearance of this corrected term h_1 in Eq. (3.82) is multiplying a term of order a/L (another small quantity: $\approx 1/10$ in relevant experiments), it becomes clear that this correction contributes around 1 part in 10^5, to the final mode frequency, while the effects we are interested in are corrections of 1 part in 10^3. The preceding analysis suggests that there is no significant μ radial dependence according to the theoretical model described here, that is, $\mu[T(r)] = \mu T_\mathrm{eq}$, where T_eq is the radial thermal equilibrium temperature of the plasma. Combined with the result for $\lambda[T(r)]$, we expect a small frequency decrease as thermal energy diffuses radially outwards, coming entirely from the λ effect. The general result is then a minor modification of Eq. (3.96), where we explicitly keep the $\overline{\mu}[T(r)]$ in functional form even though we determined that they can

be written entirely in terms of the radial equilibrium temperature.

$$\overline{\alpha}[T(r)] \approx (\overline{\mu}[T(r)] - \overline{\lambda}[T(r)]) - h\varepsilon(\overline{\mu}[T(r)] + \overline{\lambda}[T(r)]), \tag{3.122}$$

which is the more accurate form of Eq. (3.114). Since we found no radial dependence in $\overline{\mu}$, then $\overline{\lambda}$ provides the only radially dependent frequency correction. As shown in Fig. 3.9, $\overline{\lambda}$ this signifies a (-1.5%) mode frequency shift corresponding to the radially outward flux of thermal energy.

3.12.1 Radial Temperature Effect according to the Bounce-Averaged Theory

To check for more subtle effects than the analytic theory from the previous section can provide, we return to the Bounce-Averaged solution described in Sec. 3.6, where this time we introduce a non-uniform temperature profile. To check for any nontrivial frequency functional dependence $\alpha[T]$, we consider a realistic plasma with rounded ends and non-rectangular density profile. We then reproduce the experiments by injecting heat into only the central portion of the plasma, and using the theory to calculate the diocotron mode frequency. Next, we do the same thing for the plasma after it has come to thermal equilibrium along r, to compare to the experiments. If our previous theoretical analysis is correct, we should see only a small frequency decrease due to the $\lambda[\Delta T]$ as outlined in Fig. 3.9. In this numerical study, we take a rounded-square plasma with $n_{\text{cent}} = 1.5 \times 10^7 \text{cm}^{-3}$ and radius $R_{\text{p}} = 1.35\text{cm}$ initially at $T = 1\text{eV}$, and heat the center $r < 0.2\text{cm}$ of the plasma up to $T_{\text{cent}} = 6\text{eV}$, shown in Fig. 3.12.

The plasma is then allowed to thermally equilibrate, keeping the total thermal energy throughout the plasma fixed. The initial and final theoretical mode frequencies are plotted in Tab. 3.4. Interestingly, Tab. 3.4 predicts a 0.25% *increase* in mode frequency as heat flows from the plasma center outward, which is opposite to the result predicted in the previous section, and much more pronounced. While the mechanism is not presently understood, clearly one of

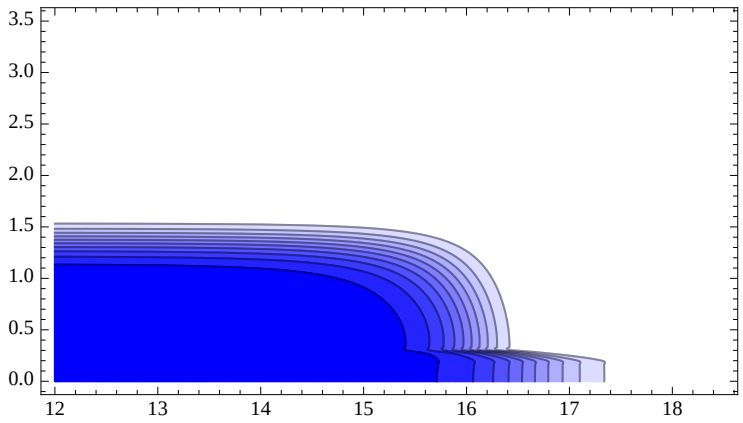

Figure 3.10: The initial density as a function of z (horizontal) and r (vertical) with a 6eV central region surrounded by a 1eV region.

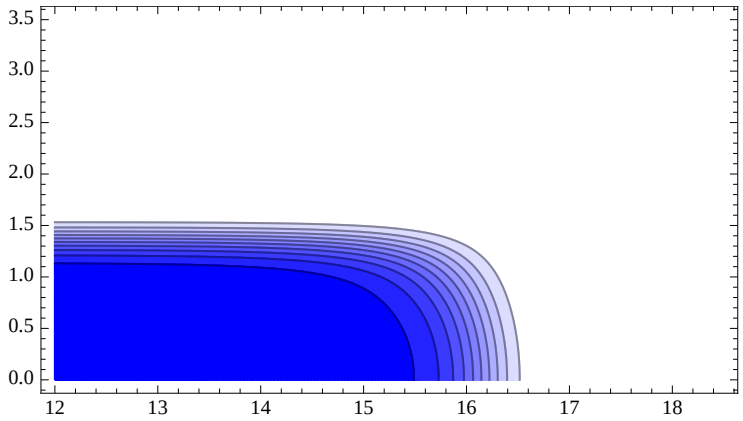

Figure 3.11: The final density as a function of z (horizontal) and r (vertical) after the plasma in Fig. 3.10 has come to radial thermal equilibrium.

the assumptions made in the preceding analysis needs to be improved in order to capture this effect. Inspection of the bounce-averaged eigenfunction for $\ell = 1$ shows that the perturbed density is indistinguishable from a uniform translation to the equilibrium density $n_0(r,z)$, even for a non-uniform temperature profile. This indicates that the discrepancy does not come from the effective fluid theory making this assumption for the eigenmode.

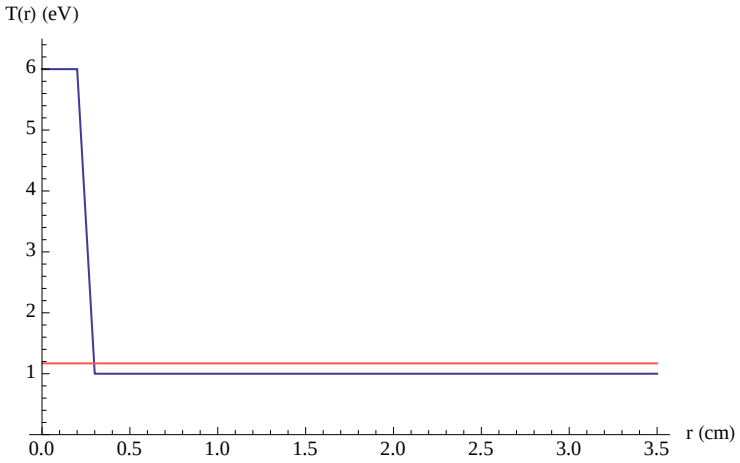

Figure 3.12: The initial thermal profile (blue), and the thermal profile once the plasma has equilibrated (red). Results shown in Tab. 3.4.

Table 3.4: $\ell = 1$ diocotron mode frequency before and after the hot inner plasma core comes to thermal equilibrium with the rest of the plasma, according to the Bounce-Average theory.

	ω (sec^{-1})
Hot center	17445
Equilibrium	17490

Chapter 4

Philosophy

4.1 Why Plasma Theory is Challenging

Plasma physics is veritably a wide and complex field of study, and consequently any modest discussion of the general challenges of plasma physics will be incomplete. In this introduction, I will provide an overview of the two main problems I have solved during my study here at UCSD, both of which share the theme of kinetic effects in plasmas, and also explain why these problems are challenging, both theoretically and computationally. Today, an active field of study related to plasma physics is fluid dynamics. This field of physics concerns itself with understanding the motion of a fluid by treating it as a continuum rather than a collection of a large number of particle constituents of the fluid. As a result, fluids are characterized by a collection of fields which describe the variation of various quantities throughout the medium–density, velocity, temperature, pressure, et cetera. From a course-grained point of view, a physicist could argue that fluid theory is actually quite simple in principle; one simply imagines the fluid as subdivided into infinitesimal fluid elements throughout space, then the net forces on each of these elements (typically either from local fluid interactions such as pressure gradients, viscosity, or external forces like gravity) are obtained, and finally Newton's laws are used to calculate the evolution

of the fluid. Since these forces can be calculated from the configuration of the fluid at a given time, it is not difficult to integrate the equations of motion forward in time from some initial condition and determine the state of the fluid at some later time. To understand kinetic effects of plasma physics, on the other hand, the fluid equations are upgraded to the Vlasov Equation or the Boltzmann Equation, which can be thought of as a fluid theory existing not in space, but rather in phase-space. The density is upgraded to the *distribution function*, which provides the probability of finding a particle near that position and momentum. While kinetic plasma theory is in this way analogous to fluid theory in the sense that it is a fluid theory in $2n$ dimensions, where n is the spatial dimension of the problem, there exists a few new complications in the transition from fluid theory to kinetic plasma theory. First, the dimensionality of the partial differential equations being solved doubles, making the solution more difficult to obtain. Second, the equations are no longer local in the sense that the plasma density (which is coupled to the electric and magnetic fields, which in turn influence the plasma evolution) is an integral of the distribution function over all momenta, so these new momentum dimensions are unlike extra spatial dimensions in that they are non-local. Third, in charged plasmas the density of the plasma at some point affects the evolution of the plasma at every other point through the electromagnetic field, which for our purposes are immediately established with no retardation. In this sense, the plasma equations are not even local in *space* because of the (near) instantaneous action of the electromagnetic field. While this final observation is equally valid in the fluid theory of a charged plasma, it is absent in the theory of uncharged and non-conducting fluids, where the only forces acting are either from some external field (e.g. gravity), or a local interaction (e.g. gradients in the pressure or velocity fields).

The second obstacle present across this body of work that is the subject of great attention is in the analysis of inhomogeneity and *boundary effects*, that are frequently discarded or approximately handled via handwaving arguments in much existing work. Often, plasma boundaries are argued away by imposing mathematically convenient boundary conditions (Dirichlet, Neumann,

Periodic...), but unfortunately, unlike a physical boundary such as a conducting wall or some similar condition, a plasma end can be "fuzzy"; the plasma density can drop off gradually, leading to the failure of the "boundary condition" analysis. To make matters worse, for the thermal effects ubiquitous in this paper, the particle orbits make any effective fluid theory non-local in space, giving rise to a "kernel" of finite spatial extent, which couples regions of the plasma separated by an appreciable distance. Consequently, any boundary condition to be imposed is far more subtle than matching a function value and derivative on the boundary, but requires identification of the functions to the left and right of the "boundary" within some finite interval! As a result, Bernstein modes are better understood in an infinite, uniform plasma, but not well understood in a realistic plasma with boundary, where there are not simply two boundary conditions to match, but an infinite set of them (for example the set of derivatives of all order at the boundary). For example, in chapter 2, we can get away with this by using asymptotic analysis to match finite intervals of the perturbed potential from one region to its neighbors. While an existing work[9] analyzed Bernstein Modes in a non-uniform plasma, the work did not capture the correct coupling of Bernstein modes to the Cold-Fluid Theory in the plasma edge, which is the subject of chapter 2. Similar themes of non-uniformity will appear in chapter 3, where here we consider both radial and axial plasma dependence, where the appropriate kernel is now far more non-local, coupling regions on opposite axial ends of the plasma due to warm particles quickly bouncing from end to end across the entire length of the plasma.

The third recurring difficulty throughout this dissertation concerns itself with computational techniques and numerics. There are several features of the research problems discussed here that simply for computational reasons alone, increase the difficulty even more:

1. *The curse of dimensionality*: We discussed that distinct from fluid dynamics, kinetic plasma physics dictates that each spatial dimension comes with its own momentum dimension. A problem necessitating N computational grid points along each dimension in n dimensions thus requires N^{2n} total grid points. Needless to say, this is exponential growth, so taking

even a meager $N = 10$ in $n = 3$ brings the problem to one million total grid-points and one million unknowns to be determined. A full linear system of equations for such a problem has a number of elements equal to the square of the number of unknowns and equations, which in the example case equates to one trillion matrix elements, which is not feasible. This is referred to as the *curse of dimensionality*, since increasing the dimensionality of the problem by a small amount can turn a soluble problem into an insoluble one. Consequently, compromises and simplifications must be made in order to make progress. Some examples of these tricks are assuming symmetry in certain dimensions (such as dropping z-dependence or assuming an $e^{i\ell\theta}$-dependence), using sparse matrices, and re-writing the problem as a superposition of harmonics in a basis where the solution is expected to have few large components, so fewer need be kept.

2. Convergence: The issue of convergence, particularly in chapter 2, was a significant source of difficulty. Each dimension has associated with it a different adjustable convergence parameter–typically the number of grid points along that dimension–and sometimes the results showed slow convergence, or a degree of convergence that was non-monotonic in the number of variables kept in a certain dimension. It appears that there is some non-trivial interplay between the various convergence parameters of the problem, making the results unexpectedly sensitive to the choice of these parameters, and to each other. The reason for this behavior is still not understood, and generally the attitude taken in this work is to focus to a lesser degree on the details of understanding the peculiarities of the numerics, to instead focus on the physics. In other words, when convergence was not met, we simply increase *all* of the convergence parameters together until we run out of computational power.

3. Memory: When describing the computational details to my coworkers, I would often receive the suggestion to simply run the code for a longer duration in order to reach convergence. Unfortunately, this is not always a feasible solution, since in my experience, memory, not

CPU time, was the main bottleneck. While the amount of computational effort used to solve a problem can be increased either by increasing the processor speed *or* by increasing the time spent on the problem, computer RAM is a limited resource. Once a computer program uses all available memory, aside from (very slowly) writing data to the hard disk, the program cannot recover, and a great deal of resources is wasted. Many linear algebra solver routines that operate on large matrices eat up significant memory, as they must generate new temporary matrices (for example methods that use the LU decomposition), which may not be as sparse as the original matrix. In hindsight, direct methods of solution for linear algebra problems should be avoided for 3D problems where the sheer size of the matrices has high memory impact.

4. Philosophy of Physics: Finally, there is a philosophical problem unrelated to computation per se, but of great importance in my study of physics and which is responsible in part for driving my research. This problem is with regards to the realization that "Numerical computation, alone, is not physics". It is easy to become so dependent on a problem that one will go to great lengths just to find the answer. Numerical computation affords a powerful way to gain answers to such complicated questions. However, after the insight into the physics theory appears, the pen stops writing, and finally the ideas are implemented into a computer code, all that remains is to use the code to generate results. These results are important in comparing the theory to experiments and to other theories, but the intrinsic value of the computation is rather shallow; the computer code simply tells you *how* the physics behaves, but seldom provides an understanding of *why* it behaves that way. In this way, computers often act as black boxes, and on their own are not sufficient to study physics. For this reason, this dissertation uses numerical results only as needed to draw comparison to analytic expressions and experiments, rather than using them to exhaustively study the problem in all conceivable regimes.

4.2 Kinetic Theory and the Scope of this Dissertation

In light of the difficulties described in the previous section, it is no surprise that understanding the kinetic effects of plasmas is currently an active area of research. Kinetic theory, when analytically tractable, is often restricted to ideal situations–uniform plasmas that extend to infinity, or plasmas of only one species–cases that are not obtainable experimentally, or at least much more challenging experimentally to produce. The work in this dissertation addresses solutions to problems that depart from these theoretically ideal scenarios.

In chapter 2, the theory of Bernstein modes is extended, examining both analytical and computational solutions to non-uniform plasma columns, with either a single species, or multiple species, which allow comparison to experiments that are neither uniform, infinite, nor comprised of a single species. Since Bernstein modes are thermal effects, arising from the finite Larmor Radius of particles in the magnetized plasma, the cold fluid theory is only valid in the $T \to 0$ limit, where a single cyclotron resonance is observed in the plasma response to a driver, and no additional structure is seen. As the temperature is increased, a family of new modes, called *Bernstein modes* are predicted to emerge from the single cyclotron resonance. At low temperatures, these modes are very closely spaced in frequency, and are not resolvable due to some physical damping mechanism such as particle collisions. However, when the temperature is increased, the mode spacing increases, and a number of Bernstein modes appear, no longer hidden by the finite collisionality. The origin of these modes is that the non-zero Larmor radius of the plasma particles allows them to explore a finite neighborhood around their guiding center positions as they undergo their small circular orbits. As a result, at any time, the force felt by these particles differs from the force that would be predicted from cold fluid theory, where every point in space has a single unambiguous fluid velocity rather than the actual Boltzmann distribution of particle velocities.

In chapter 3, a completely different problem is solved by extending diocotron theory to

study non-ideal theoretical aspects regarding the theory of finite-length and thermal effects on the diocotron mode frequency. Similar to the situation in chapter 2, while a cold diocotron mode is well-described with cold fluid theory, a temperature increase produces a frequency shift to the diocotron mode. We will see that there are two physical reasons for this. First, the plasma density changes as temperature increases and the particles travel farther axially before returning. Since even the infinite-length diocotron frequency depends on the density, this effect tends to make the mode frequency decrease as temperature increases. Second, these warm particles also feel a stronger radial force from the confinement cylinders which acts to increase the mode frequency. Third, the fact that the plasma itself has a finite length means that the self-consistent plasma fields differ from that of an infinite column, either from the image field (as in $\ell = 1$), and in the non-image field (as in $\ell > 1$). The net frequency shift is some combination of these effects.

Appendix A

Structure of Cold Fluid Response

The fluid theory for a plasma with annular Bernstein wave region is also rather interesting; there are two surface cyclotron peaks in the plasma response $\mathrm{Im}(Y)$, rather than the expected, single peak. By comparing figure 2.15 and figure A.1, It turns out that the left and right peaks appearing in figure A.1 occur at the same frequencies as the blue (solid) and red (dotted) curves in figure 2.15, corresponding to the frequencies at which the dielectric function satisfies $\varepsilon'_{11}(r) = \varepsilon_{11}(r) = 0$ at some value of r. These values of r are labeled with the numbers 1 and 2, and the corresponding frequencies are also labeled in Fig. A.1. We will take a small detour to understand why the admittance has peaks at such locations.

To simplify the analysis, we employ the admittance function from the old cold fluid theory valid in the large magnetic field limit[6]:

$$Y = \ell + \frac{{r_\mathrm{w}}^{2\ell}}{\int_0^{r_\mathrm{w}} r'^{2\ell-1}/\varepsilon_{11}(r')\,dr'}, \tag{A.1}$$

Defining I as the integral $I \equiv \int_0^{r_\mathrm{w}} r'^{2\ell-1}/\varepsilon_{11}(r')\,dr'$, we have

$$\mathrm{Im}(I^{-1}) = \frac{-I_\mathrm{i}}{{I_\mathrm{r}}^2 + {I_\mathrm{i}}^2},$$

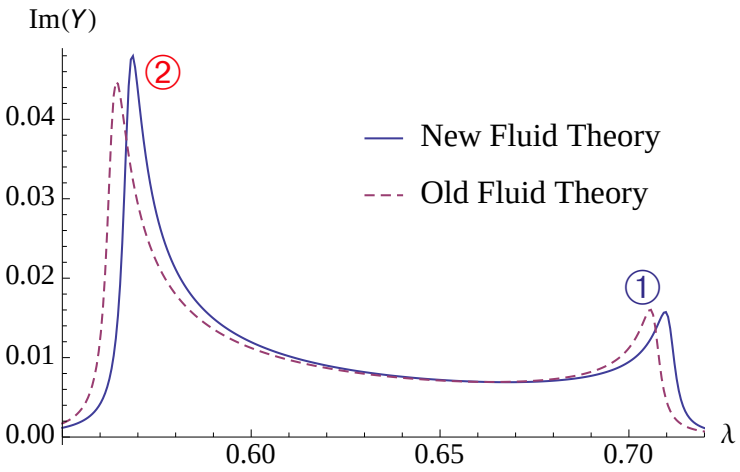

Figure A.1: In some cases, the cold fluid theory predicts two peaks in $\mathrm{Im}(Y)$, rather than one. Here we look at a plasma with $\ell = 2$, $\Omega = 10.45$, $R_\mathrm{p} = 10.5$, $\delta_\mathrm{res} = 56.3\%$, $r_\mathrm{w} = 83.54$, comparing the exact fluid theory developed in this paper, and the approximate fluid theory (using a large Ω expansion) by Dubin[6].

where the subscripts indicate a shorthand for the real and imaginary parts of I. Now suppose, as is true for the plasma under consideration, that $r_\mathrm{w} \gg R_\mathrm{p}$ so that there is a large vacuum region outside the plasma. In this case, I_r is dominated by the vacuum region (for $\ell > 1$) because $\varepsilon_{11}(r \gg R_\mathrm{p}) = 1$, whereas I_i has no contribution in this region. So we assume $I_\mathrm{r} \gg I_\mathrm{i}$, so that

$$\mathrm{Im}(I^{-1}) = \frac{I_\mathrm{i}}{I_\mathrm{r}^2},$$

and further, we can approximate $I_\mathrm{r} \approx \int_0^{r_\mathrm{w}} r'^{2\ell-1}\, dr' = \frac{{r_\mathrm{w}}^{2\ell}}{2\ell}$. This gives the expression

$$\mathrm{Im}(I^{-1}) = \frac{-4\ell^2 I_\mathrm{i}}{r_\mathrm{w}^{2\ell}}. \tag{A.2}$$

In the limit of small ν, the I_i integral can be conveniently evaluated using contour integration. The zeroes of ε_{11}, which are the poles of appearing in the I integral, occur just above or just below the real axis, depending on the sign of $\varepsilon'_{11}(r_\mathrm{UH})$. Because ν tends toward zero, the argument of I_i is effectively zero away from upper-hybrid radii, and sharply peaked near the upper-hybrid radii. We can therefore extend the range of integration to the entire real line without modifying

the value of the integral, and use the Plemelj formula to integrate around the poles. Notating the upper-hybrid radii where $\varepsilon_{11}(r) = 0$ as s_k, the result is

$$\mathrm{Im}Y = \frac{4\ell^2}{r_w^{2\ell}} \sum_k \frac{{s_k}^{2\ell-1}}{\left|\varepsilon'_{11}(s_k)\right|}. \tag{A.3}$$

This expression provides a useful way to estimate the cold fluid response of a plasma existing well within the wall without having to evaluate an integral over the entire plasma. It also immediately allows one to see that the peaks of ImY occur where $\varepsilon'_{11}(s_k) = \varepsilon_{11}(s_k) = 0$, which justifies the observation we made in figure A.1.

Appendix B

An alternate derivation of Bessel Functions

As an alternate, more physical derivation of the result derived in Sec. 2.5.1, we reconsider the problem of solving for eigenmodes of an arbitrary linear wave equation. In this section, we will consider solutions to equations with the following constraints:

1. Solution to a linear wave equation possessing plane waves as solutions,
2. Solutions with eigenfrequency ω are superpositions of plane waves with wavelength compatible with the dispersion relation: $k = |\vec{k}| = k(\omega)$,
3. Problem is uniform and isotropic, so $|k(\vec{\omega})|$ is not a function of the direction of wave propagation,
4. Posesses our desired $e^{i\ell\theta - i\omega t}$ dependence.

With these constraints, we can write down an expression for the potential as a superposition of plane waves:

$$\phi(\vec{r}) = \int A(\vec{k})\delta\left(|\vec{k}| - k(\omega)\right) e^{i\vec{k}\cdot\vec{r}}\, d\vec{k}. \tag{B.1}$$

All this equation is saying is that we can write down a general linear wave equation solution as a (continuous) superposition of plane waves with the appropriate wavenumber. Since the isotropic

dispersion constrains $|\vec{k}| = k(\omega)$, a delta function is introduced to ensure that any non-compatible wave vectors are destroyed. Consequently, the value of $A(\vec{k})$ on the circle of radius $|\vec{k}(\omega)|$ is all that is required. We can express this in polar coordinates by parametrizing the circle by a single parameter α (the angle measured conventionally from the x-axis), and $|\vec{k}|$ (a fixed "wavevectorial radius"), we can write Eq. (B.1) as follows:

$$\phi(\vec{r}) = \int_0^{2\pi} \int_0^{\infty} A(|\vec{k}|, \alpha) \delta\left(k_r - k(\omega)\right) e^{i|k| r \cos(\alpha - \theta)} |\vec{k}| \, d|\vec{k}| \, d\alpha. \tag{B.2}$$

The cosine in the exponent comes from taking the dot product of the position vector $\vec{r}$ with the wavevector $\vec{k}$. Converting to the relative angle variable $\beta = \alpha - \theta$, we can write this as

$$\phi(\vec{r}) = k(\omega) \int_0^{2\pi} A(\beta + \theta) e^{ikr\cos\beta} \, d\beta, \tag{B.3}$$

Since we seek solutions with $e^{i\ell\theta - i\omega t}$ dependence, and since the only remaining θ-dependence appears in the coefficient A, we had better have that A factors as $A(\beta+\theta) = f(\beta)g(\theta) = f(\beta)f(\theta)$, where the last equality follows by the symmetry of the argument of A upon interchange of β and α. Further, we seek solutions with $e^{i\ell\theta}$ dependence, so we learn that $f(\theta) \sim e^{i\ell\theta}$. Simplifying gives

$$\phi(\vec{r}) = A e^{i\ell\theta} k(\omega) \underbrace{\int_0^{2\pi} e^{i(k(\omega r \cos\beta + \ell\beta))} \, d\beta}_{!!}. \tag{B.4}$$

Since $k(\omega)$ and $2\pi i^{\ell}$ have no radial dependence, they can simply be absorbed into the multiplicative constant A. The result is that the solution with the θ-dependence we seek must be of the form

$$\phi(r, \theta) = A \mathrm{J}_{\ell}(k(\omega) r) e^{i\ell\theta}. \tag{B.5}$$

Appendix C

Separating plasma integrals into two parts

In Chapter 3 we need to evaluate the integral $\int_{-\infty}^{0} \cos k(z-z')dz'$, which does not, strictly speaking, converge. In order to do the integral anyways, we will keep the infinite limit, and later will do a limiting process as the lower limit tends toward $-\infty$. So we instead compute

$$\int_{-\infty}^{0} \cos k(z-z')dz' = \frac{-\sin(k(z-z'))}{k}\bigg|_{-\infty}^{0} \to \frac{-\sin(kz)}{k} - \lim_{Z\to\infty}\left[\frac{\sin(kZ)}{k}\right]. \tag{C.1}$$

We can understand the second term in the limit as $Z \to \infty$ by considering its integral over all values of k:

$$\int_{-\infty}^{\infty} \frac{\sin(kZ)}{k}\, dk = \mathrm{Im}\left(\int_{-\infty}^{\infty} \frac{e^{ikZ}}{k}\, dk\right), \tag{C.2}$$

which can be computed by considering a D-shaped contour that avoids the pole at $k = 0$:

$$\int_{-\infty}^{\infty} \frac{\sin(kZ)}{k}\, dk = \pi \mathrm{sgn}(Z). \tag{C.3}$$

We have $Z \to \infty$, so $\mathrm{sgn}(Z) \to +1$. Interestingly, regardless of the (positive) choice of Z, the integral remains constant. On the other hand, the graph of the integrand becomes horizontally scaled down as Z increases, which implies that $\frac{\sin(kZ)}{k}$ can be made to oscillate arbitrarily fast by

further increasing Z, therefore making any integral not including the origin to integrate to zero. This demonstrates that the function $\lim_{Z\to\infty}\frac{\sin(kZ)}{k}$ integrates to π when the integration range includes the origin, and zero otherwise, and therefore it has the requisite properties of the function $\pi\delta(k)$. Using this identification, we obtain the desired result:

$$\int_{-\infty}^{0}\cos k(z-z')dz' = \pi\delta(k) - \frac{\sin(kz)}{k}. \tag{C.4}$$

Bibliography

[1] M. Affolter, F. Anderegg, D. H. E. Dubin, and C. F. Driscoll. Cyclotron mode frequencies and resonant absorption in multi-species ion plasmas. *Physics of Plasmas*, 22(5), 2015.

[2] D. Baldwin and A. Kaufman. Determination of the density profile in a plasma slab. *Phys. Fluids*, 12:1526, 1969.

[3] R. C. Davidson. *Physics of nonneutral plasmas*. Imperial College Press London, 2001.

[4] D. Dubin. Displacement eigenmodes for cold-fluid and warm-fluid magnetized plasma oscillations. *Phys. Plasmas*, 12:1–13, 2005.

[5] D. H. E. Dubin. *Numerical and Analytical Methods for Scientists and Engineers*. John Wiley and Sons, New York, 2003.

[6] D. H. E. Dubin. Cyclotron waves in a non-neutral plasma column. *Physics of Plasmas*, 20(4), 2013.

[7] K. S. Fine and C. F. Driscoll. The finite length diocotron mode. *Physics of Plasmas*, 5(3):601–607, 1997.

[8] R. W. Gould. Theory of cyclotron resonance in a cylindrical non-neutral plasma. *Physics of Plasmas (1994-present)*, 2(5):1404–1411, 1995.

[9] R. W. Gould and M. A. LaPointe. Cyclotron resonance phenomena in a pure electron plasma. *Physics of Fluids B*, 4(7):2038–2043, 1992.

[10] G. W. Hart and R. L. Spencer. Properties of axisymmetric bernstein modes in an infinite-length non-neutral plasma. *Physics of Plasmas*, 20(10), 2013.

[11] T. J. HIlsabeck and T. O'Neil. Finite length diocotron modes. *Physics of Plasmas*, 8(2), 2000.

[12] H. Jeffreys. On isotropic tensors. In *Mathematical Proceedings of the Cambridge Philosophical Society*, volume 73, pages 173–176. Cambridge Univ Press, 1973.

[13] N. G. V. Kampen. On the theory of stationary waves in plasmas. *Physica*, 21:949, 1955.

[14] R. H. Levy. Two new results in cylindrical diocotron theory. *Phys. Fluids*, 11(920), 1968.

[15] T. M. ONeil. Centrifugal separation of a multispecies pure ion plasma. *The Physics of Fluids*, 24(8):1447–1451, 1981.

[16] T. M. ONeil and C. F. Driscoll. Transport to thermal equilibrium of a pure electron plasma. *Physics of Fluids*, 22(2):266–277, 1979.

[17] E. Sarid, F. Anderegg, and C. F. Driscoll. Cyclotron resonance phenomena in a nonneutral multispecies ion plasma. *Physics of Plasmas*, 2(8):2895–2907, 1995.

[18] D. Schecter, D. Dubin, A. Cass, C. Driscoll, I. Lansky, and T. O'Neil. Determination of the density profile in a plasma slab. *Phys. Fluids*, 12(2397), 2000.

[19] T. Stix. *The Theory of Plasma Waves*. McGraw-Hill, New York, 1962.

[20] A. W. Trivelpiece and R. W. Gould. Space charge waves in cylindrical plasma columns. *Journal of Applied Physics*, 30(11):1784–1793, 1959.

[21] H. Weyl. *The classical groups: their invariants and representations*. Princeton university press, 2016.